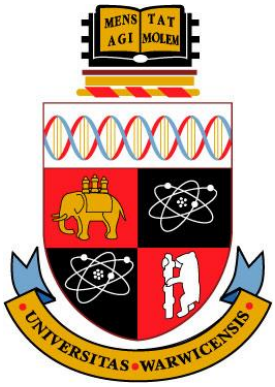

Developments and Applications of

Electrochemical Microscopy

by

Robert Alexander Lazenby

A thesis submitted for the degree of

Doctor of Philosophy in Chemistry

THE UNIVERSITY OF WARWICK

Department of Chemistry

September 2014

I would like to dedicate this thesis to my family.

“Practice without thought is blind; thought without practice is empty.”

Kwame Nkrumah, 1909 – 1972

Table of Contents

List of Figures

List of Tables

Acknowledgements

I would like to thank my supervisors, Patrick Unwin and Julie Macpherson. Their guidance and mentoring throughout has been invaluable, and their support has made this work possible.

I also thank Lee Butcher and Marcus Grant in Mechanical workshops, for making some of the designs for electrochemical cells and workstation components used for experiments in this thesis. I thank Dr. Alexander W. Colburn for designing and building electronic instrumentation used in this work.

I thank all members of the Warwick Electrochemistry and Interfaces Group (WEIG), not only for the collaborations and the people with whom I have worked, but equally importantly to everyone for providing a friendly and fun place to work.

I also thank the Engineering and Physical Sciences Research Council (EPSRC), for funding this work.

Finally, of course, I would like to thank my family for their support and patience, to whom I dedicate this work.

Declaration

This thesis is my own work except where it contains work based on collaborative research, in which case the nature and extent of the author's individual contribution shall be indicated.

This thesis is submitted to the University of Warwick in support of my application for the degree of Doctor of Philosophy. It has been composed by myself and has not been submitted in any previous application for any degree at another university.

The work presented (including data generated and data analysis) was carried out by the author except in the cases outlined below:

List of data provided and/or analysis carried out by collaborators.

i) Chapter 3: The image of Calcite in Figure 3-2 was made with Michael M. Mbogoro and the white light interferometry (WLI) image in Figure 3-3 was made by Michael M. Mbogoro.

ii) Chapter 4: Kim McKelvey developed the steady-state finite element method simulations of mass transport to a recessed disk-shaped ultramicroelectrode.

iii) Chapters 3 and 4: Kim McKelvey wrote the LabVIEW code for intermittent contact-scanning electrochemical microscopy (IC-SECM) and hopping (H)IC-SECM.

iv) Chapter 5: The microscale scanning electrochemical cell microscopy (SECCM) measurements and analysis were done with Stanley C. S. Lai.

v) Chapter 5: Paul M. Kirkman performed the atomic force microscopy image in Figure 5-8.

vi) Chapter 6: Voltammetric experiments were performed with Süheda Isikli.

Parts of this thesis have been published by the author:

List of publications (including submitted papers).

Quantitative localized proton-promoted dissolution kinetics of calcite using scanning electrochemical microscopy (SECM)

C-A. McGeouch, M. Peruffo, M. A. Edwards, L. Dexter, R. A. Lazenby, M. M. Mbogoro, K. McKelvey and P. R. Unwin, *J. Phys. Chem. C*, **2012**, *116*, 14892-14899.

As featured in Chapter 3.

Hopping intermittent contact-scanning electrochemical microscopy (HIC-SECM): visualizing interfacial reactions and fluxes from surfaces to bulk solution

R. A. Lazenby, K. McKelvey and P. R. Unwin, *Anal. Chem.*, **2013**, *85*, 2937-2944.

As featured in Chapter 3.

Nanoscale intermittent contact-scanning electrochemical microscopy

R. A. Lazenby, K. McKelvey, M. Peruffo, M. Baghdadi and P. R. Unwin, *J. Solid State Electrochem.*, **2013**, *17*, 2979-2987.

As featured in Chapter 4.

Nucleation, aggregative growth and detachment of metal nanoparticles during electrodeposition at electrode surfaces

S. C. S. Lai, R. A. Lazenby, P. M. Kirkman and P. R. Unwin, *Chem. Sci.*, **2015**, *6*, 1126-1138.

As featured in Chapter 5.

Quad-barrel multifunctional electrochemical and ion conductance probe for voltammetric analysis and imaging

B. P. Nadappuram, K. McKelvey, J. C. Byers, A. G. Güell, A. W. Colburn, R. A. Lazenby, P. R. Unwin, *Anal. Chem.*, **2015** – submitted.

As featured in Chapter 4.

Impact of surface parasitic processes on quinone electron transfer kinetics

S. Isikli,† R. A. Lazenby,† R. B. Channon, M. Lecea, M. Ribagorda, M. C. Carreño, A. G. Güell, R. Díaz, P. R. Unwin, – in preparation.

† These authors contributed equally to this work.

As featured in Chapter 6.

Hopping intermittent contact-scanning electrochemical microscopy (HIC-SECM) as a dissolution kinetic probe: application to salicylic acid dissolution in aqueous solution

A. R. Perry,† R. A. Lazenby,† M. Adobes-Vidal, M. Peruffo, K. McKelvey, M. E. Snowden and P. R. Unwin, *Cryst. Eng. Comm.*, **2015** – submitted.

† These authors contributed equally to this work.

An example of the use of HIC-SECM, not featured in this thesis.

Abstract

This thesis is concerned with the use of electrochemical microscopy, in particular the development and application of the scanning electrochemical microscope (SECM). The concept of intermittent contact (IC), *i.e*. detecting the oscillation amplitude damping of an SECM imaging probe as it makes physical contact with a surface, is presented as a non-electrochemical means to provide tip-substrate distance feedback, in IC-SECM. This is briefly demonstrated for localised etch pit formation on a calcite crystal. A new imaging mode that incorporates a hopping imaging mode with the principles of intermittent contact is demonstrated for a range of samples, in hopping (H)IC-SECM. HIC-SECM uses an oscillating probe, so alternating current data are also obtained, and this type of scanning mode allows three-dimensional visualisation of the flux around an interface, which greatly enhances the information content compared to other types of electrochemical imaging. The resolution achievable by constant-distance imaging using IC-SECM is greater than constant-height imaging, although the dimensions of the electrode used in imaging will limit the resolution. Pt disk nanoelectrodes were also prepared, that were milled using focussed ion beam-scanning electron microscopy (FIB-SEM). These probes were used to image a model substrate, a gold band on glass, using IC-SECM in a low-force soft-tapping setup. The extension of this work to electrochemical systems focuses on studies of electrodeposition of silver nanoparticles on basal plane highly oriented pyrolytic graphite (HOPG). A nucleation-aggregative growth-detachment mechanism is proposed as an important feature of the process, through both macroscopic and microscopic scanning electrochemical cell microscopy (SECCM). The active sites for electron transfer on HOPG, a topic of recent debate, were also probed in macroscopic and microscopic experiments for silver electrodeposition. The difficulties of working on the electrochemistry of quinones in non-aqueous media are highlighted, with particular focus on methods to overcome the issue of electrode fouling. Different degrees of surface fouling were observed depending both on the electrode material, the compound studied and its concentration. IC-SECM was introduced as a means of establishing a close tip-substrate gap without needing to do electrochemistry for positioning and thus minimising fouling effects, from which high rate constants could be measured and the effect of electrode material on electron transfer kinetics investigated.

Abbreviations

Abbreviation	Definition
$[C_2mim][NTF_2]$	1-ethyl-3-methyl-imidazolium bis(trifluoromethylsulfonyl)imide
2D	Two-dimensional
3D	Three-dimensional
4D	Four-dimensional
AC	Alternating current
AFM	Atomic force microscopy
AM	Refers to HOPG of the highest quality, originating from Arthur Moore and kindly provided by Prof. R. L. McCreery (University of Alberta, Canada)
AQ	Anthraquinone
BPPG	Basal plane pyrolytic graphite
CE	Counter electrode
CF	Carbon fibre
CM	Contact mode
CNT	Carbon nanotube
CV	Cyclic voltammetry
DAQ	Data acquisition
DC	Direct current
DFT	Density functional theory
DIC	Differential interference contrast
DLC	Diamond-like carbon
DMF	Dimethylformamide
DOS	Density of electronic states
EPPG	Edge plane pyrolytic graphite
ET	Electron transfer
$FcTMA^+$	Ferrocenylmethyltrimethylammonium ion

FEM	Finite element method
FE-SEM	Field emission-scanning electron microscopy
FIB-SEM	Focused ion beam-scanning electron microscopy
GC	Glassy carbon
HIC-SECM	Hopping intermittent contact-scanning electrochemical microscopy
HOPG	Highly oriented pyrolytic graphite
IC-SECM	Intermittent contact-scanning electrochemical microscopy
ID	Inner diameter
LSV	Linear sweep voltammetry
MeCN	Acetonitrile
MWNT	Multi-walled carbon nanotube
NMR	Nuclear magnetic resonance
NP	Nanoparticle
NQ	Naphthaquinone
O	Oxidised form of a redox species
OD	Outer diameter
OM	Optical microscopy
pBDD	Polycrystalline boron doped diamond
p-BQ	*Para*-benzoquinone
PC	Personal computer
PSA	Pressure sensitive adhesive
Q	Quinone species
$Q^{\bullet -}$	Semiquinone (radical anion) species
QRCE	Quasi-reference counter electrode
QRE	Quasi-reference electrode
R	Reduced form of a redox species
R, E^+, E^-	Racemic(+/-) mixture, enantiomer(+) and enantiomer(-) of 2-(*p*-tolysulfinyl)cyclohexane-2,5-diene-1,4-dione), respectively
RE	Reference electrode

SECCM	Scanning electrochemical cell microscopy
SECM	Scanning electrochemical microscopy
SEM	Scanning electron microscopy
SG/TC	Substrate generation/tip collection
SGS	Strain gauge sensor
S-H	Scharifker and Hills
SICM	Scanning ion conductance microscopy
SPI-3	Commercial HOPG sample, of low quality (high step edge density) from SPI Supplies
SPM	Scanning probe microscopy
SWNT	Single-walled carbon nanotube
TBAP	Tetrabutylammonium phosphate
$TBAPF_6$	Tetrabuthylammonium hexafluorophosphate
TEAB	Tetraethylammonium bromide
TG/SC	Tip generation/substrate collection
TM	Tapping mode
TPM	Tip-position modulation
UHV	Ultra-high vacuum
UME	Ultramicroelectrode
UV	Ultraviolet
VP	Variable-pressure
WE	Working electrode
WLI	White light interferometry

Glossary of Terms

Symbol	Definition
$[X]_{bulk}$	Concentration of species X in bulk solution
$[X]_O$	Concentration of species X at the electrode surface
a	Tip electrode radius
A	Area of the electrode
A	Pre-exponential factor
alpha	Probe angle with respect to substrate
c^*	Bulk concentration
d	Tip electrode to substrate separation
D_X	Diffusion coefficient for species X
E	Electrode potential
E^0	Standard electrode potential
$E^{0'}$	Formal potential
$E_{1/2}$	Half wave potential
$E_{1/4}$	Quarter wave potential
$E_{3/4}$	Three-quarter wave potential
E_e	Equilibrium potential
E_F	Fermi level
F	Faraday's constant
i	Current
I	Current density
i_0	Exchange current
i_∞	Current at the tip electrode, in bulk solution (*i.e.* $d = \infty$)
$i_{lim(disk)}$	Steady-state limiting current at a disk electrode
I_m	Maximum current density
i_{ss}	Steady-state limiting current
i_T	Current at the tip electrode

$I_T(L)$	Current at the tip electrode, normalised by tip radius
$i_{T,\infty}$	Current at the tip electrode, in bulk solution (*i.e.* $d = \infty$)
j	Diffusional flux
J	Current density
k and k’	Constants in Scharifker and Hills analysis for instantaneous and progressive nucleation, respectively
k^0	Standard rate constant
k_B	Boltzmann constant
k_{ox}	First order heterogeneous rate constant for an oxidation process
K_p	Equilibrium constant
k_{red}	First order heterogeneous rate constant for a reduction process
k_T	Steady-state mass transfer coefficient
L	Tip electrode to substrate separation, normalised by tip radius
L_a	Intraplanar microcrystalline size
L_c	Interplanar microcrystalline size
M	Molecular weight
m_O	Effective mass transfer coefficient
n	Number of electrons
N	Total number of nuclei
n	Unit normal vector
N_∞	Number density of active sites
R	Molar gas constant
r	Recession depth of tip electrode
RG	Ratio of glass sheath radius to electrode radius
r_g	Glass sheath radius
T	Temperature
t	Time
t_m	Time at maximum current
V	Coupling strength

V_1	Floated potential bias applied to both QRCEs in SECCM, with respect to ground
V_2	Potential bias applied between QRCEs in SECCM
x	Piezo position along the surface
y	Piezo position along the surface
z	Charge
z	Piezo position normal to the surface
α	Transfer coefficient
γ	Ratio of diffusion coefficients for oxidised and reduced species
δ	Oscillation amplitude
ΔG^*	Gibbs energy of activation
$\Delta G^{\ddagger}$	Gibbs free energy of activation
η	Overpotential
θ_{AC}	Phase difference of the alternating current
κ	Electronic transmission coefficient
κ'	A dimensionless rate constant that reflects electron transfer kinetics and the mass transport coefficient
λ	Wavelength
v	Potential scan rate
v_n	Nuclear barrier crossing frequency
ρ	Density
$\Psi(\Delta E)$	Parameter evaluated (see Equation (6.6))

1 Introduction

This thesis covers multiple areas of study in electrochemistry. In particular, the electrochemical imaging technique, scanning electrochemical microscopy (SECM), is developed further in terms of improving the resolution by imaging with nanoelectrodes and a hopping scanning mode, which both use the principles of intermittent contact (IC)-SECM as a means of tip-substrate distance feedback. To put this work into context with the state of the art, the fundamental principles of a dynamic electrochemical process are described, and types of electrodes for SECM and related techniques are discussed.

Carbon is an important electrode material in electrochemistry, and this is also studied here in terms of fundamental electron transfer kinetics of carbon materials and the electrodeposition of nanoparticles that have been grown on carbon surfaces. The studies carried out include not only SECM, but also scanning electrochemical cell microscopy (SECCM), a new addition to the electrochemical imaging family. A background of such processes is given in this Chapter. Additionally, a brief overview of the other experimental techniques used for the work in this thesis is presented.

1.1 Basic electrochemistry

Electrochemistry is typically concerned with the charge transfer chemical reactions that occur at the interface of an electrode and a solution. This can be under the regime of equilibrium or thermodynamic control, in which no external potential source is applied, or dynamic electrochemistry, in which an electrochemical process can be driven by applying an external voltage, with the current typically measured.[1]

1.1.1 Dynamic electrochemistry

A redox couple, that is to say a species that can undergo reduction or oxidation, in solution will have a standard electrode potential, E^0.[2] Promotion of a reduction of that species can be achieved by applying a more negative potential to the electrode than E^0 (see Figure 1-1).[1] If the applied potential, E, is equal to the equilibrium potential, E_e, then no current will flow. This is a simple approximation by Bard and Faulkner,[3] although more detailed approximations are available that account for changes to both the solution energy level and metal Fermi level.[2]

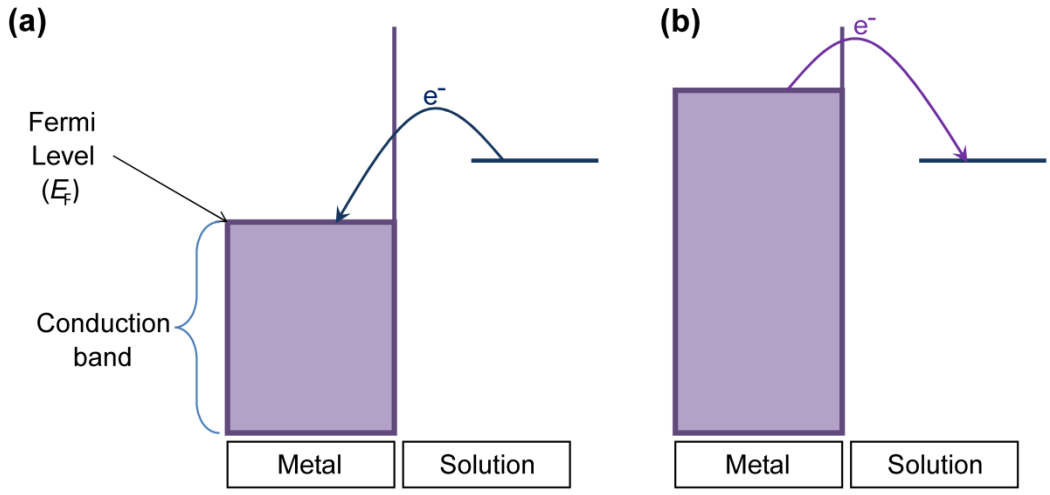

Figure 1-1. Electrode (metal) in contact with a redox species (in solution), undergoing an oxidation reaction (a) and a reduction (b).

This leads to the concept of overpotential, η, which is defined by the additional potential applied to the electrode to drive the reaction beyond the equilibrium potential as follows,

$$\eta = E - E_e \tag{1.1}$$

The equilibrium potential can be determined from the Nernst equation,[3]

$$E_e = E^0 + \frac{RT}{nF}\ln\frac{[O]}{[R]} \tag{1.2}$$

where R is the molar gas constant and T is temperature.

A general charge transfer reaction follows the form[3]

$$O + ne^- \underset{k_{ox}}{\overset{k_{red}}{\rightleftharpoons}} R \tag{1.3}$$

where O is the oxidised form of species R, and n is the number of electrons transferred. k_{red} and k_{ox} are the first order heterogeneous rate constants for the forward (reduction) and backward (oxidation) reactions, respectively.

The Fermi level (E_F) is at the top of the conduction band, which is a continuum of occupied electron states.[1] It can be formally defined as the midpoint between the top of the conduction band and the bottom of the valence band. Applying a potential to the electrode will move the Fermi level up or down in energy, and drive the equilibrium in Equation (1.3) to the right or left, corresponding to a reduction or oxidation process, respectively.

For the equilibrium in Equation (1.3), rate constants for the reduction and oxidation processes can be expressed[3]

$$k_{red} = k^0_{red} \exp\left(\frac{-\alpha F \eta}{RT}\right) \quad (1.4)$$

$$k_{ox} = k^0_{ox} \exp\left(\frac{(1-\alpha) F \eta}{RT}\right) \quad (1.5)$$

where k^0_{red} and k^0_{ox} are the standard rate constants for the reduction and oxidation processes, respectively, and α is the dimensionless transfer coefficient that reflects the nature of the transition state of the reaction. α lies between 0 and 1, where a value close to zero means that the transition state closely resembles the reactants, whereas a value close to 1 means the transition state closely resembles the products. It is usual to assume α to be ~0.5, especially for outer sphere electron transfer processes (Section 1.1.3).

The net current flowing at the electrode, i, as a function of overpotential and α is given by the Butler-Volmer equation:[3]

$$i = i_0 \left(\frac{[\mathrm{R}]_\mathrm{O}}{[\mathrm{R}]_\mathrm{bulk}} \exp\left(\frac{(1-\alpha)F\eta}{RT} \right) - \frac{[\mathrm{O}]_\mathrm{O}}{[\mathrm{O}]_\mathrm{bulk}} \exp\left(\frac{-\alpha F\eta}{RT} \right) \right) \quad (1.6)$$

where i_0 is the exchange current, which is large for reversible processes (defined in Section 1.1.2), which require little overpotential, and small for irreversible processes. $[\mathrm{X}]_\mathrm{O}$ and $[\mathrm{X}]_\mathrm{bulk}$ are the concentration of species X (O or R) at the electrode surface and in bulk solution, *i.e.* far away from the electrode surface, respectively.

1.1.2 Mass transport

The overall rate of an electrochemical reaction can be controlled by either the rate of electron transfer at the electrode surface, *i.e.* it is kinetically limited, or by the rate at which species move towards and away from the electrode surface in solution, *i.e.* it is mass transport limited.[3] These two processes are shown in Figure 1-2.

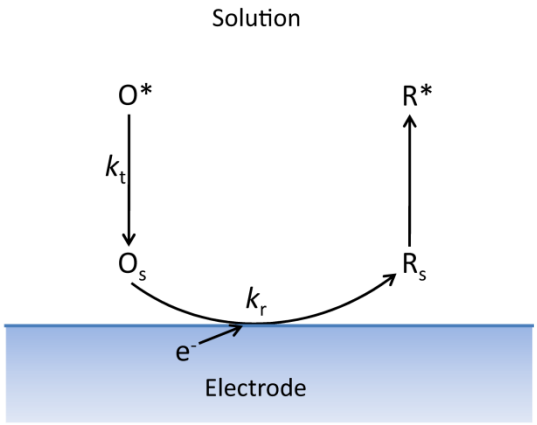

Figure 1-2. Dynamic electrochemistry with mass transport (k_t) and electron transfer (k_r) processes shown.

If an electrode process is mass transport limited, the surface electron transfer rate constant, k_r, is much bigger than the mass transfer rate constant, k_t, and the process is referred to as reversible.[1] For an electrode process that is kinetically limited by the surface, $k_t >> k_r$, this is referred to as being quasi-reversible or, ultimately, irreversible.

Mass transport is made up of three components; diffusion, migration and convection.[2] For typical electrochemical experiments, migration and convection can be successfully removed by control of experimental conditions.

Migration is the movement of charged species due to a potential gradient. This is made negligible for the analyte of interest by the addition of an electrochemically inert supporting electrolyte in large excess (*e.g.* > 100 times the analyte concentration). The effect of the supporting electrolyte is also to reduce the range of the potential gradient to a region very close (*i.e.* < 1 nm) to the electrode interface, so that the electron transfer process feels the full driving force at the electrode/solution interface. Provided the concentration of supporting electrolyte is high enough,[4] migration can be ignored.

Convection is the movement of species due to a mechanical force, either by natural or forced means. Natural convection could arise from thermal gradients or density changes across a solution, which can be avoided by performing the electrochemistry in a well-mixed (prior to experiments) solution at a stable temperature and at reasonably short times where such gradients do not have the time to be established. Forced convection is easily circumvented (or added), since this can be considered from external sources such as stirring or gas bubbling.

Diffusion is a fundamental process that is the main consideration in mass transport for electrochemists, and is defined as the movement of species down a concentration gradient. Fick's first law of diffusion describes the associated flux:[1]

$$j_{\mathrm{O}} = -D_{\mathrm{O}} \frac{\partial[\mathrm{O}]}{\partial x} \tag{1.7}$$

where j is the diffusional flux, D_{O} is the diffusion coefficient for species O and [O] is the concentration of species O.

Fick's second law describes the change in concentration of species O with time:[1]

$$\frac{\partial c_{\mathrm{O}}}{\partial t} = D_{\mathrm{O}} \left(\frac{\partial^2 c_{\mathrm{O}}}{\partial x^2} \right) \tag{1.8}$$

and this can be solved to predict concentration profiles *etc*.

Nernst approximated the diffusion layer thickness, δ_{d}, by extrapolating the linear region of change in concentration close to an electrode against distance, to the point at which bulk concentration is met. This enables the current to be estimated, by considering the change in surface concentration of species O,[5]

$$i = AFD \frac{[\mathrm{O}]_{\mathrm{bulk}} - [\mathrm{O}]_{\mathrm{O}}}{\delta_{\mathrm{d}}} \tag{1.9}$$

1.1.3 Brief overview of electron transfer

The rate of electron transfer (ET), shown as k_{r} in Figure 1-2, also includes pre-equilibrium steps before the ET. These are the rearrangement of the ion atmosphere, reorientation of solvent dipoles and changes in bond lengths of the central ion and

ligands of the redox species. ET is discussed in further detail in Chapter 6. ET reactions can be classified as outer sphere or inner sphere.[5] At an electrode, outer sphere reactions involve minimal structural changes, since there is no strong interaction between the reactant and product with the electrode. In outer sphere processes, solvent reorganisation is important. Inner sphere reactions involve larger changes in bond length, or geometry in the solvation shell, since the reactants and products have a strong interaction with the electrode surface.[6] Cleary, inner sphere reactions will depend much more on the electronic nature of the electrode material.[7]

The Butler-Volmer model underpins most interpretations of electrode kinetics.[2] Marcus theory can be used to further explain the rates of ET reactions, by taking into account the solvent. One important contribution of the Marcus-Hush theory is that it proposed that the Gibbs free energy of activation (formation of the transition state) during the ET process ($\Delta G^{\ddagger}$), is dependent on a parameter (λ) which accounts for the effects of the structural reorganisation processes occurring during the ET. $\Delta G^{\ddagger}$ is given in Equation (1.10),

$$\Delta G^{\ddagger} = \frac{\lambda}{4}\left(1+\frac{F\left(E-E^{0}\right)}{\lambda}\right)^{2} \qquad (1.10)$$

where E is the electrode potential and E^0 is the standard electrode potential.

The reorganisation energy, λ, is the energy needed for all necessary structural adjustments of the reactants and the solvent to be converted to the state of the products. The reorganisation term is composed of solvational and vibrational components.

The expression for the apparent rate constant (k_{et}) is given in the standard Arrhenius relationship,[1]

$$k_{et} = A\exp\left[-\Delta G^{\ddagger} / k_B T\right] \tag{1.11}$$

where, A is the pre-exponential factor that contains the probability of a reactant passing through the transition state, and k_B is the Boltzmann constant.

1.2 Experimental methods

In a two-electrode electrochemical cell, a (varying) potential is applied to the working electrode, with respect to a second electrode; the quasi-reference counter electrode (QRCE). The solution is located between the electrodes, and current is measured at the QRCE (Figure 1-3(a)). This setup is adequate for small currents (< 1 μA in aqueous electrolyte solution, *e.g.* resistance < 100 Ω), since the ohmic drop is low (< 0.1 mΩ). For currents larger than about 1 μA in aqueous solution, a three-electrode setup is used (Figure 1-3(b)), in which the current is measured by a third electrode, known as the counter electrode (or auxiliary electrode).

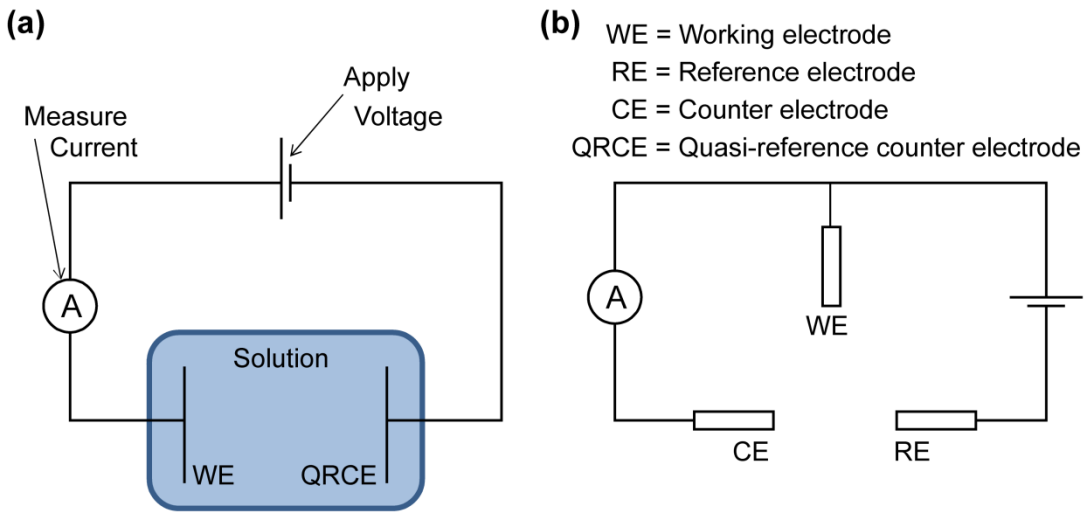

Figure 1-3. Typical electrode setup, using two electrodes (a) or three electrodes (b).

A quasi-reference counter electrode (QRCE) is an electrode that takes the role of both the reference electrode and the counter electrode.

1.2.1 Chronoamperometry

Chronoamperometry is a technique in which the potential of the working electrode is changed suddenly in a 'step' fashion from one potential to another (Figure 1-4). The current response is recorded against time, to produce a current-time plot.[5] An example of a diffusion-limited current-time curve is given in Figure 1-4(b), although this will be considered for other processes such as the electrodeposition of metals in Section 1.6.2 and Chapter 5.

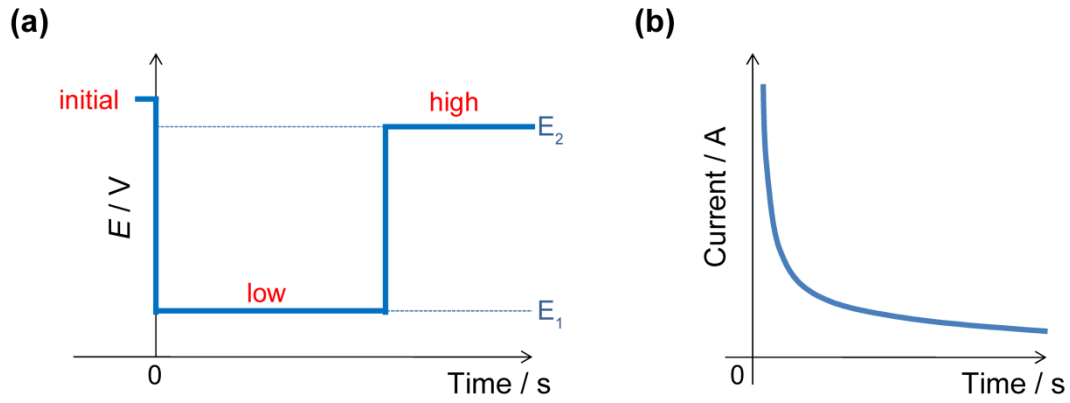

Figure 1-4. Potential step experiment (a) and a resultant current-time curve for the 'low' region (b).

1.2.2 Voltammetry at macroelectrodes

Voltammetry is important as it allows the study of electrolysis mechanisms.[8] A potentiostat can be used to control the applied potential, and a current can be measured. Linear-sweep voltammetry (LSV) involves changing the potential of the working electrode linearly between two limits, over a set period of time, corresponding to the scan rate. Cyclic voltammetry (CV) is similar to LSV, except after the potential reaches the first limit, the potential sweep direction is reversed. These two sweeps are known as the forward scan and the reverse scan. The current in the forward scan is in the opposite direction to the reverse scan. In Figure 1-5, the forward scan shows current due to an oxidation process, whereas the current in the reverse scan is due to a reduction of the same species.

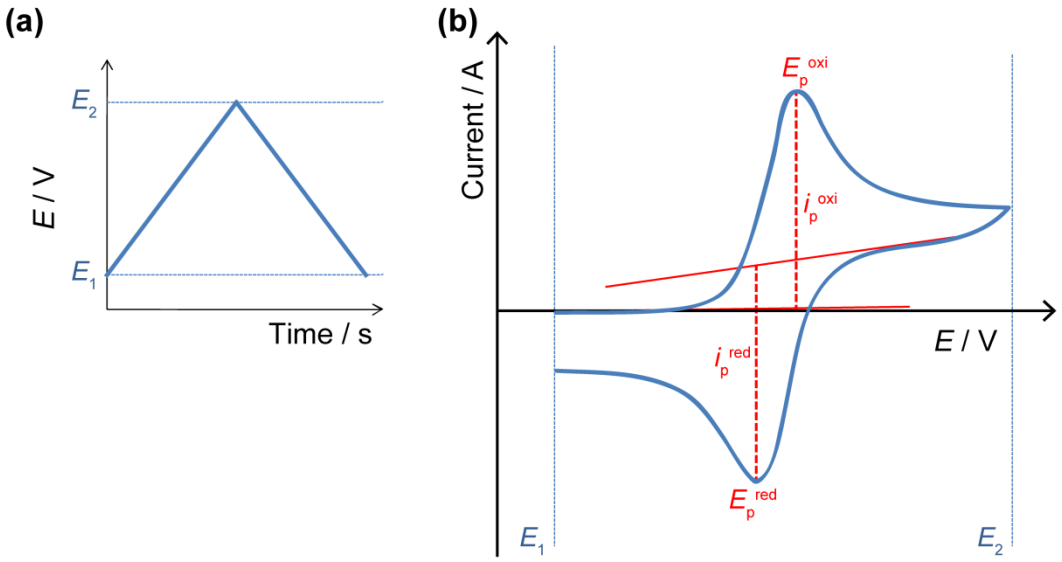

Figure 1-5. The applied potential sweep (a) and resultant current-voltage curve (b) for cyclic voltammetry.

The peak current, i_p, in the CV for a diffusion-limited process, *i.e.* reversible, is given by the Randles-Sevcik equation

$$i_p = 0.4463nFAc^*(nF\nu D/RT)^{1/2} \quad (1.12)$$

where A is the area of the electrode and ν is the potential scan rate. This can be simplified by combining the constants (at T = 25 °C) to give

$$i_p = 2.69\times10^5 n^{3/2} AD^{1/2}\nu^{1/2}c^* \quad (1.13)$$

The peak in current arises due to the diffusion of species to the electrode controlling the rate of reaction. In a reduction, species O diffuses to the surface and is reduced to R, thus reducing the surface concentration of O, $[O]_O$. New O arrives to the surface from the bulk solution, and the rate at which this diffusional process occurs will determine the rate of reaction, and thus the current observed at the electrode.

Also, it is clear that i_p is proportional to $\sqrt{\nu}$. A faster scan rate means that there is less time for the depletion of species O near the surface, and the diffusion layer will be thinner. This gives a steeper concentration gradient, resulting in a larger flux that enhances the peak current.

1.3 Diffusion at electrodes

The size of an electrode determines the diffusion profile that is set up when a voltage is applied. The differences in electrochemical behaviour between large electrodes (*i.e.* > 1 mm) and ultramicroelectrodes (UMEs) (< 100 μm) arise from their modes of diffusion. For a UME, the voltammetric behaviour will depend on the timescale of the experiment.[3] At very short timescales, the behaviour resembles that of a planar (macro) electrode. This is evident in Chapter 6, in which CVs are carried out at scan rates that do not produce a steady-state response that is typical for UMEs.

1.3.1 Macroelectrodes and ultramicroelectrodes

When a concentration gradient is set up at a large electrode, species diffuse to the electrode according to a planar diffusion field. At an UME, there is a significant contribution from radial diffusion, ultimately leading to a hemispherical diffusion field, and a greater flux. These two diffusion regimes are shown in Figure 1-6.

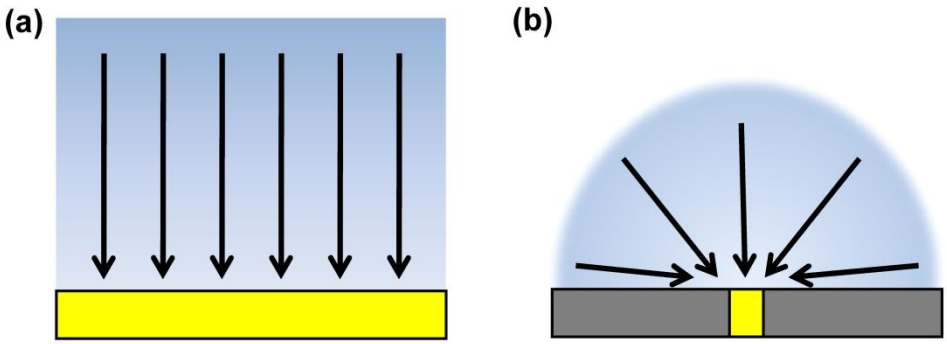

Figure 1-6. Diffusion profiles at a macroelectrode (linear) (a), and at a UME (hemispherical) (b).

The diffusion process described at a UME is often associated with a steady-state response, as shown in Figure 1-7(b), in which a limiting current (i_{lim}) is attained.[9]

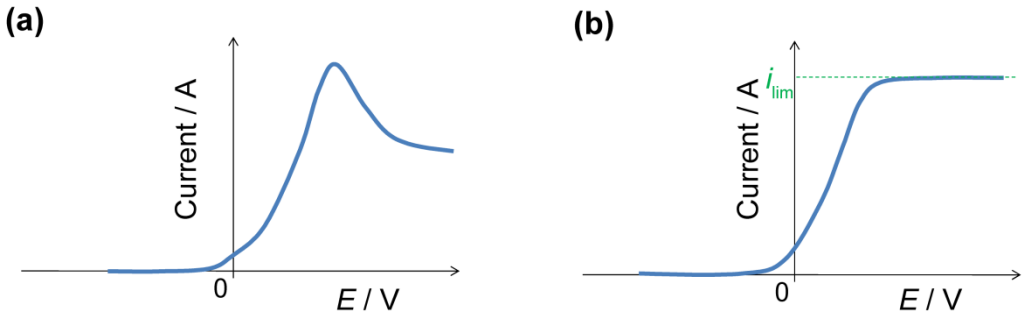

Figure 1-7. LSV showing a peak response associated with a macroelectrode (a) and a steady-state response associated with an ultramicroelectrode (b).

Since the diffusion profile at a UME is hemispherical (see Figure 1-6(b)), the replenishment of O at the electrode surface is sufficient that a steady-state current is achieved. In bulk solution, the steady-state limiting current, $i_{lim(disk)}$, is given by:

$$i_{lim(disk)} = 4naFDc^* \qquad (1.14)$$

where n is the number of electrons, a is the electrode radius in cm, F is Faraday's constant (96 485 C mol^{-1}), D is the diffusion coefficient of the redox species in solution and c^* is the bulk concentration of the redox species. This equation applies to a UME in an infinite plane. UMEs can also be used as imaging probes, for example when brought close to a surface, the current can give information about the topography and electrochemical activity of the underlying substrate, as in scanning electrochemical microscopy, *vide infra*. An example of a UME used in this way is shown in Figure 1-8.

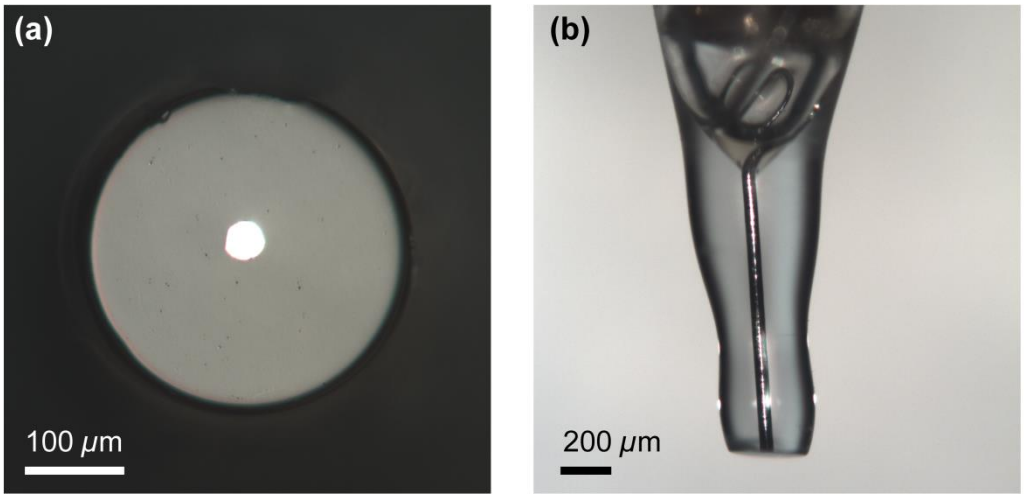

Figure 1-8. Bright field optical microscope image of a 25 μm diameter Pt UME, viewed end-on (a) and from the side (b).

The ratio of glass sheath radius, r_g, to electrode radius, a, is the RG value,[10]

$$RG = \frac{r_g}{a} \tag{1.15}$$

the dimensions of which are labelled in the schematic in Figure 1-9.

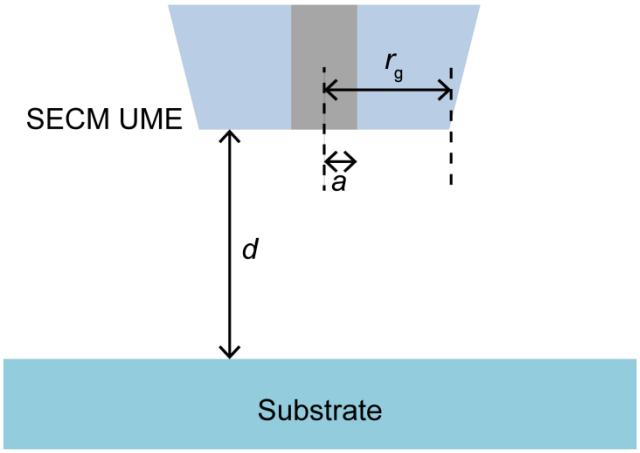

Figure 1-9. Notable dimensions used in scanning electrochemical microscopy.

When a UME has a low *RG*, *i.e.* of the order of the diffusion layer thickness, Equation (1.14) is no longer valid, since there is an additional flux due to the availability of additional material from the back of the electrode. There are a few attempts to incorporate the effect of *RG* into an estimation of current magnitude, i.e. to take into account the additional diffusion of species from around the corner of the electrode, notably by Denuault,[11] Xiong,[12] Lefrou,[13] Lee,[14] and Mirkin.[15] This is of particular importance for SECM, as discussed in Section 1.4.2.

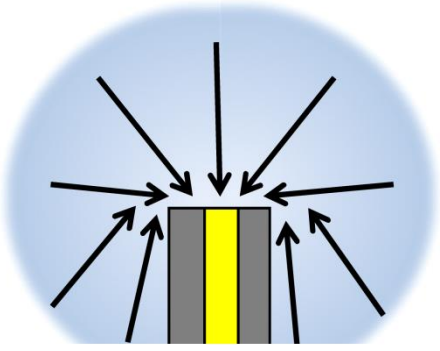

Figure 1-10. Back diffusion to a UME with low *RG*.

Ultramicroelectrodes have non-planar diffusion, which gives rise to higher current density over macroelectrodes. Current density is given by

$$J = \frac{i}{A} \tag{1.16}$$

which relates the current, *i*, to the total area of the electrode, *A*. UMEs also have reduced capacitance and reduced ohmic drop over macroelectrodes. These are differences that favour UMEs in the measurement of fast electrochemical processes.

1.3.2 Nanoelectrodes

Nanometre-sized Pt probes have been used as electrochemical sensors,[16] and kinetics of these tips have been studied,[17] with a number of papers describing their fabrication.[18-22] Nanoelectrodes have been discussed,[23] with the principle advantage being the enhanced mass transport rates due to radial diffusion. This allows the measurement of kinetics of faster electrode reactions.[17,24] In terms of scanning electrochemical microscopy, smaller electrodes allow for improved imaging resolution. Sub-micron platinum[25] and gold[26] electrodes have been fabricated for use in SECM-AFM (Section 1.4.8). The fabrication of needle-type Pt disk nanoelectrodes[18,19] is described in Section 2.2.3, and their use as an imaging probe is demonstrated in Chapter 4.

1.4 Scanning electrochemical microscopy (SECM)

Scanning electrochemical microscopy (SECM), a scanned probe microscope (SPM) introduced in 1989 by Bard *et al.*,[27] involves scanning a surface with an

ultramicroelectrode (UME) as the probe tip. The tip is immersed in solution containing electrolyte. In feedback mode, a potential is applied to the tip, as it is scanned across the substrate, and a current is measured. SECM is still a growing field, with over 1600 publications (based on a SciFinder search for the term "scanning electrochemical microscopy" as entered), which has been accelerated by the introduction of the first commercial instrument by CH Instruments in 1999.[28]

1.4.1 Modes of operation

There are many different modes of SECM, which include feedback,[29] tip generation/substrate collection (TG/SC), substrate generation/tip collection (SG/TC), redox competition[30] and surface interrogation[31] modes. In feedback mode, the current will increase or decrease depending on whether the substrate is a conductor or an insulator, respectively.[29] At an insulating substrate, the diffusion field around the tip is compressed, meaning fewer oxidised species can migrate to the tip to get reduced, resulting in negative feedback, *i.e.* a lower current close to the surface. A conducting substrate is able to regenerate the oxidised species from the reduced species, thus increasing the availability of the oxidised species to the tip. This increases the current, known as positive feedback. These processes are shown in Figure 1-11.

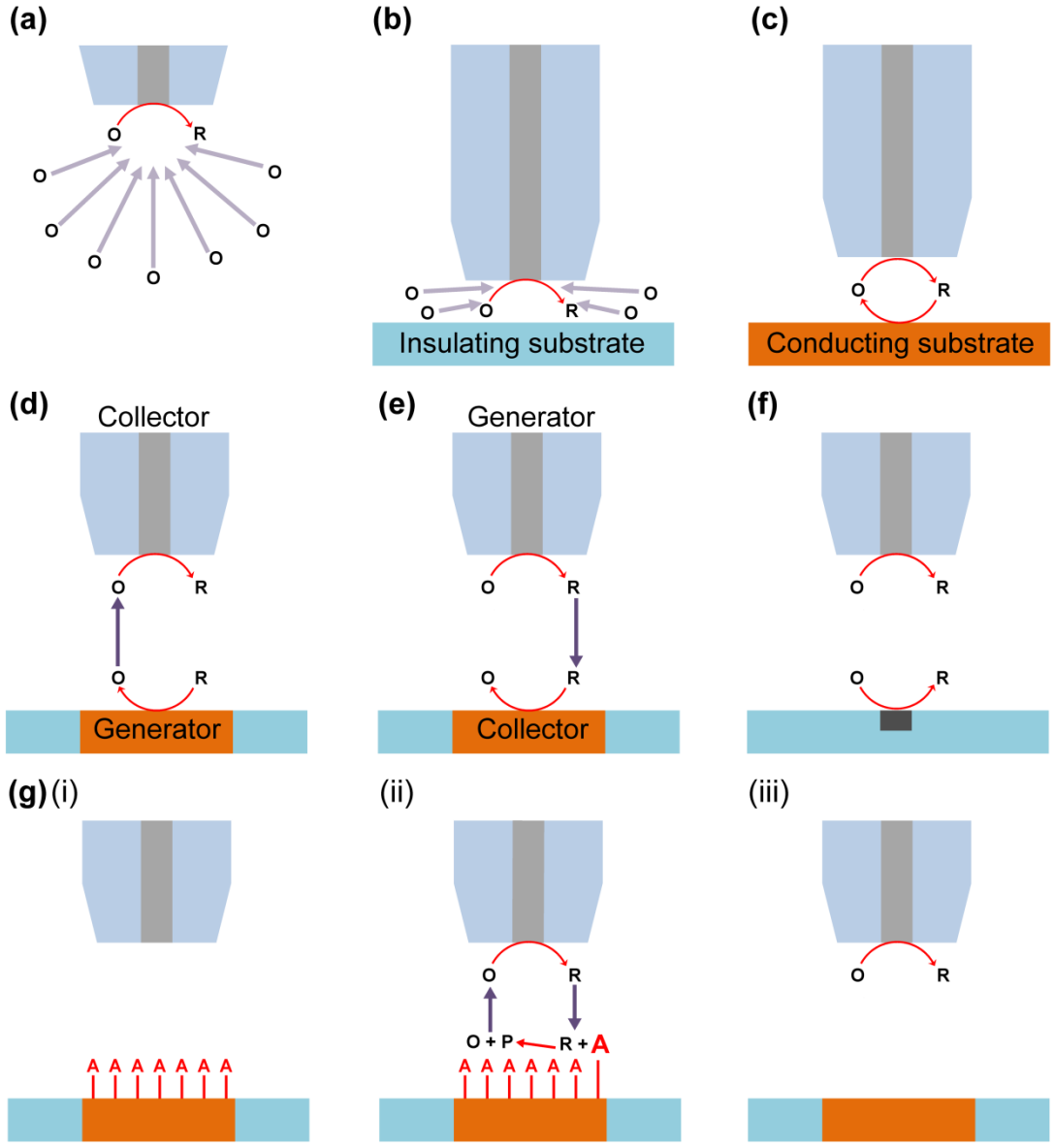

Figure 1-11. (a) Unhindered diffusion of oxidised species (O) to electrode in bulk solution, (b) negative feedback - hindered diffusion of O at an insulating substrate, (c) positive feedback - regeneration of species O at a conducting substrate, (d) SG/TC mode and (e) TG/SC mode, (f) redox competition mode and (g) surface interrogation mode.

In SG/TC mode, a potential is applied to the substrate, and the current is measured at the tip. This is considered easier than feedback mode for nanometre probes, because

the tip-substrate separation need not be as small.[32] In TG/SC mode, the potential is applied to the tip, and the current is measured at the substrate.

In redox competition mode, the tip competes with the substrate for the same analyte, which leads to a reduction in tip current when it is positioned over a catalytically active site on the substrate.[30] Surface interrogation is shown schematically in Figure 1-11(g).[31] Firstly, a reactive species is adsorbed onto the substrate electrochemically, whilst the tip is held at open circuit, as shown in (g)(i). Then, the substrate is held at open circuit, whilst the tip generates the titrant that reacts with the adsorbed species at the substrate ((g)(ii)). This results in positive feedback at the tip, until the adsorbed species is consumed off the surface, resulting in negative feedback at the tip, as shown in (g)(iii).

1.4.2 Approach curves

The curve resulting from a plot of tip current against tip-substrate separation, *d*, is an approach curve, and attempts have been made to model these in the literature for purely negative[11,33-36] and positive feedback.[11,13,33,37,38] In the case of negative feedback, Bard describes the tip current normalised for all tip radii, $I_T(L)$, by the equation:[39]

$$I_T(L) = \left[0.292 + \frac{1.5151}{L} + 0.6553 \exp\left(\frac{-2.4035}{L} \right) \right] \quad (1.17)$$

$$L = \frac{d}{a} \quad (1.18)$$

$$I_T(L) = \frac{i_T}{i_{T,\infty}} \quad (1.19)$$

Bard also describes the case for positive feedback (for RG = 10):[33]

$$I_T(L) = \left[0.68 + \frac{0.78377}{L} + 0.3315\exp\left(\frac{-1.0672}{L}\right)\right] \quad (1.20)$$

Examples of approach curves, *i.e.* positive feedback (by Lefrou)[13] and negative feedback (by Cornut and Lefrou),[36] are shown in Figure 1-12.

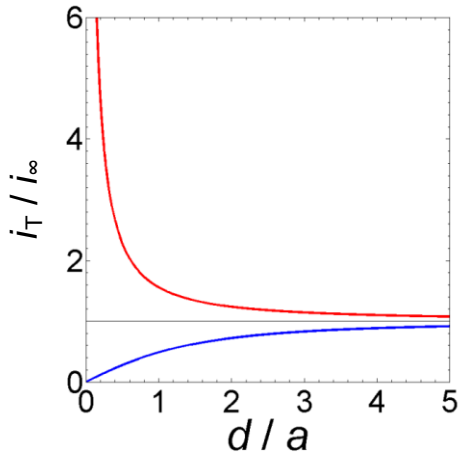

Figure 1-12. Theoretical approach curves for a UME approaching a surface in feedback mode, for an electrical insulator in negative feedback (blue)[36] and an electrical conductor in positive feedback (red).[13]

Clearly, the RG value will have an effect on the shape of the approach curve, and this effect is much greater for an approach to an insulating surface, and for RG > 10.[14,15] A low RG value is also important in SECM in order to achieve the smallest tip-substrate gap.[40]

1.4.3 Feedback mechanism

SECM measures electrochemical response, with spatial resolution determined by tip size and shape, and the tip-substrate separation.[32] A fundamental drawback is that any response depends on both topography and activity of the surface. If you desire higher resolution imaging using SECM, smaller electrodes are required, but smaller tips are more likely to crash into the surface when there is no feedback to adjust the tip-substrate separation; this is known as tip-crash.

SECM is typically operated in constant-height mode, following a raster scan pattern, as shown in Figure 1-13(a). That is the tip is scanned over a surface at a fixed height but due to changes in surface topography and sample slope, the tip-to-substrate distance is undefined. Without positional feedback, this can lead to the tip losing the surface, as depicted in Figure 1-13(b), or tip-crash, Figure 1-13(c). Losing the surface will mean that the imaging resolution becomes much worse, since changes in tip current due to substrate nature are much more apparent at small tip-substrate separation, as is evident in an approach curve for low d/a in Figure 1-12.

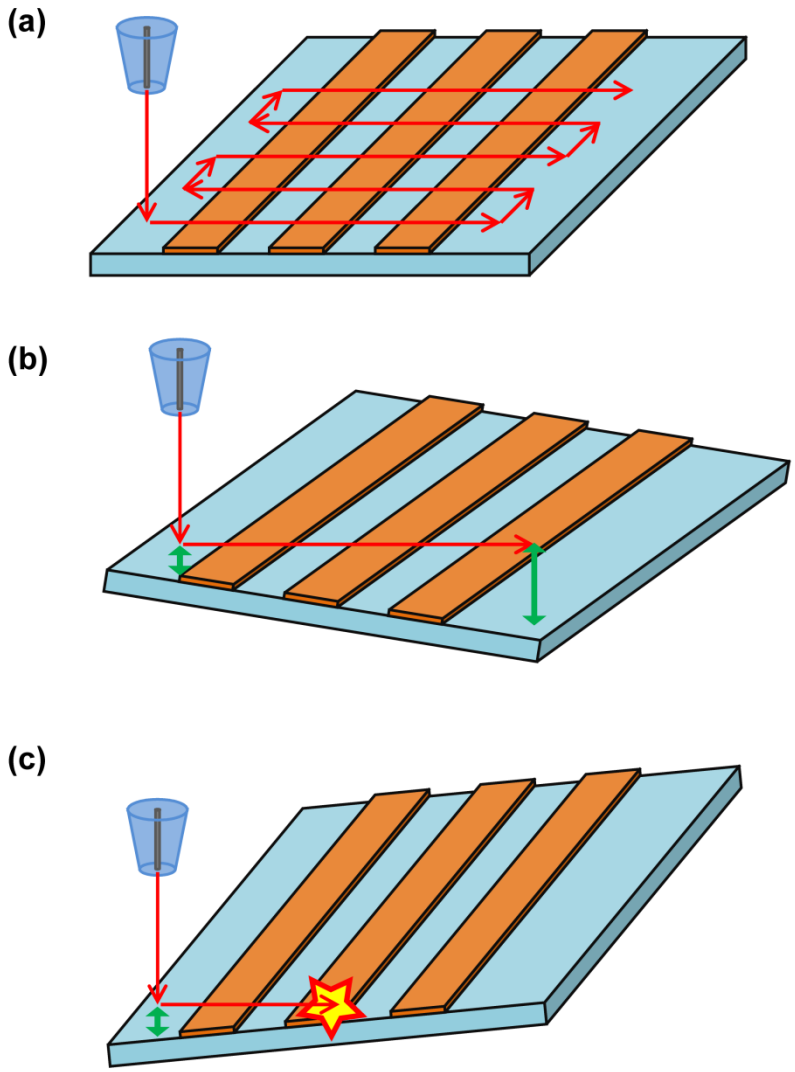

Figure 1-13. A raster scan pattern in constant-height mode SECM (a), and two scenarios that could arise from this due to a sloped sample; the tip losing the surface (b) and the tip crashing into the surface (c).

These are extreme cases, which can be minimised by having a large tip-substrate distance and good alignment between a flat substrate and the tip, but these conditions are not ideal, and are especially problematic when the dimensions of the probe are reduced. The two factors that are important to increase the spatial imaging resolution of SECM are UME size and tip-substrate separation. Following Bard's approximation for negative feedback in Equation (1.17), for the current at the tip to

drop to half the value in the bulk, the electrode needs to be a distance of about a tip radius away from the surface. In the mode discussed above, constant-height mode, there is no means of telling exactly how far for the surface the electrode is, since the current at the tip is influenced both by tip-substrate separation (d/a) and the conducting nature of the underlying substrate, that is to say the topography and the electrochemical activity are convoluted. These two modes of SECM are depicted in Figure 1-14.

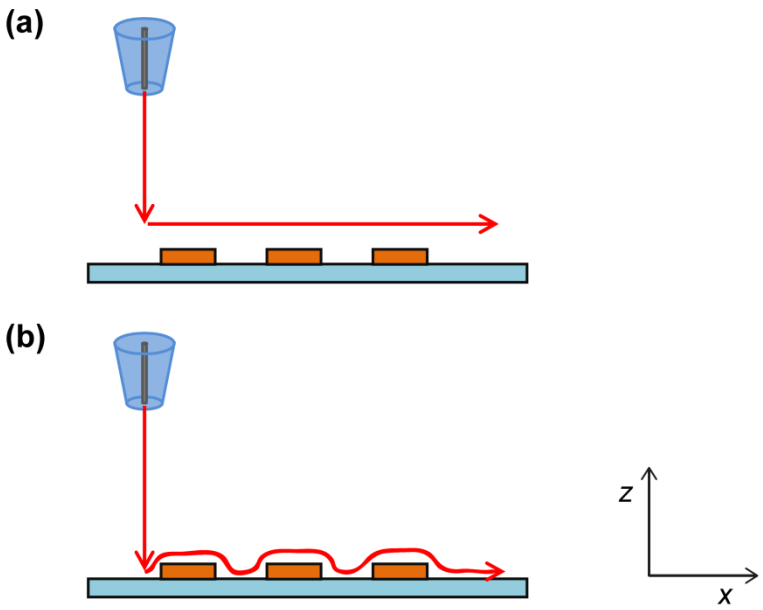

Figure 1-14. Constant-height mode (a) and constant-distance mode (b) scanning profiles.

Constant-distance mode, in which the tip follows the surface topography maintaining a fixed tip-substrate distance throughout the scan, is clearly preferable, although this would require a means of deconvoluting the topography and activity. A constant current mode would provide constant-distance imaging for a uniformly active substrate, *i.e.* all conductive or all insulating substrate. In this mode, a feedback loop

will adjust the tip position to provide constant current, thus tracking the topography of the substrate. Generally, substrates are not uniformly active, and a topography feedback mechanism that is not affected by the substrate activity is needed. Note that a feedback mechanism is not to be confused with the feedback mode of SECM discussed in Section 1.4.1.

1.4.4 Examples of feedback mechanisms for SECM

A feedback mechanism is not a trivial task, and there are a number of examples in the literature of attempts to use feedback with SECM for imaging at a constant-distance.

Shearforce SECM uses an oscillating probe, although the oscillation is lateral.[41,42] Shearforces have been used to provide feedback,[41] with constant-distance nanoimaging achieved, although this needs special tips.[43] The tip oscillates at a frequency between a few hundred Hz and a few hundred kHz, and the amplitude of this oscillation decreases when the tip is moved within a few hundred nanometres of the surface, due to the shear forces acting between tip and substrate.[44-46]

AC methods,[47,48] including the use of impedance,[49,50] have been used for positional feedback, although specialised probes are required. Tip-position modulation (TPM),[51] shown in Figure 1-15, involves the tip oscillating normal to the surface. The resulting AC and DC approach current can, in principle, be used to determine activity and topography of a surface.[52,53]

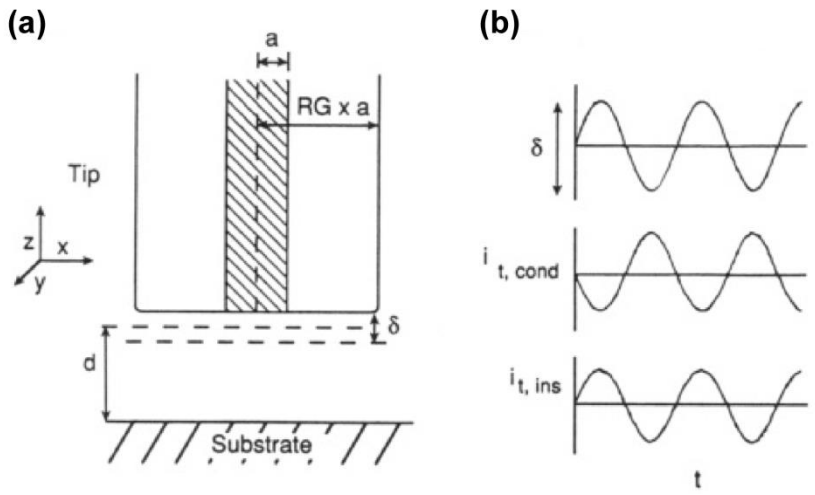

Figure 1-15. Schematic of tip-position modulation (a). Idealised graphs of tip position (δ) and tip current over a conductor ($i_{t,cond}$) and an insulator ($i_{t,ins}$) with time (b), taken from Ref.[51]

1.4.5 Intermittent contact (IC)-SECM

In intermittent contact (IC)-SECM the tip is oscillated in the *z*-axis, *i.e.* normal to the substrate, and this oscillation is dampened as the tip comes into contact with the surface.[54] This can be considered as analogous to the oscillation of the cantilever in tapping mode AFM, although the tip oscillates at much lower frequencies (*i.e.* ~100 Hz as opposed to 100s kHz). The damping of the tip oscillation provides information on tip-substrate separation, thus can be used to maintain a constant separation between the tip and substrate, allowing for high resolution imaging by maintaining the tip very close to the surface. The principles of SECM are the same, but the tip is oscillated to give feedback. User control of the IC-SECM setup is performed using custom LabVIEW code (LabVIEW 9.0, National Instruments). The technique is similar to SECM, with the additional requirements of a signal adder and an AC generator, used to apply the oscillation to the tip, plus a sensor to measure the

oscillation amplitude of the tip, and the additional control code to operate the feedback loop. IC-SECM has been used for tip-positioning[55] and to image heterogeneous electrodes,[56] but the collection of AC data during a scan, due to the oscillation of the probe, has also been a powerful tool to visualise molecular transport across dentin.[57] IC-SECM is used in Chapters 3, 4 and 6.

1.4.6 Pipette based techniques

A glass capillary can be pulled to a pipette with a fine point, using a laser puller or heated coil micropipette puller. The opening at the end of the pipette can be tuned to the size and taper length desired for specific applications. Scanning ion conductance microscopy (SICM)[58] is one application which uses the small pipette as a probe for imaging in electrolyte solution.[59]

In SICM, an Ag/AgCl reference electrode is placed in the pipette filled with electrolyte solution, and a second Ag/AgCl reference electrode is placed in solution. An ion current flows between these two QRCEs, upon application of a potential bias, which is incredibly sensitive to the tip-substrate separation close to the substrate of interest, typically an electrode radius. This technique has been especially useful for imaging living cells,[60-64] and for samples with large topographical features through the use of hopping mode scanning.[65]

Practically, the probe is oscillated, *i.e.* distance modulated, which makes feedback more sensitive since the AC is more sensitive to tip-substrate distance than the DC between the two reference electrodes.[66,67] Recently, bias modulation (BM)-SICM has

been introduced, which oscillates the potential bias between the QRCEs, which reduces convective effects and changes in supporting electrolyte composition.[68]

Another pipette technique is the scanning micropipette contact method (SMCM),[69] which uses a moveable micropipette probe, typically with a sub-micron opening, that contains an electroactive species in electrolyte solution that is brought into contact with an electrode surface. The substrate serves as the working electrode, whilst a QRCE is placed within the micropipette, in a two-electrode setup. By confining the solution in a droplet, the amount of surface exposed to the solution is controlled (defined by the droplet size) and limited (so only one part of the surface is in contact at any time. This work improved significantly from techniques employing pipettes larger than 1 μm.[70-72]

1.4.7 Scanning electrochemical cell microscopy (SECCM)

Scanning electrochemical cell microscopy (SECCM) uses a mobile double-barrelled theta pipette electrochemical cell as a probe tip.[73-75] A potential is applied between the two barrels, connected by a meniscus at the base of the tip, in contact with the surface of interest. The tip is oscillated, and the change in conductance current between barrels is measured. This enables functional imaging of interfaces with very high resolution, determined by the size of the meniscus. SECCM gives simultaneous measurement of conductance and topography and allows characterisation of local electrode activity.[76,77] SECCM has also been used for the fabrication of nanostructures,[78,79] molecular functionalisation and modification of surfaces,[80-82] and performing electrochemistry at individual nanoparticles.[83] Here, SECCM was used

in Chapter 5 to electrodeposit silver nanoparticles in a small area, *i.e.* the size of the meniscus, on the basal plane of highly oriented pyrolytic graphite.

1.4.8 Combined techniques

Combined techniques often require the fabrication of specially-designed tips, but positional feedback can also be achieved with conventional SECM probes. The first simultaneous topographical and electrochemical measurement was achieved by combining the techniques of SECM and atomic force microscopy (AFM) (see Section 1.7.4), referred to as SECM-AFM.[25] This can measure tip position independently of electrochemical response, due to a feedback signal maintaining constant tip-sample separation.[25,84-87] Custom SECM-AFM tips have been developed for this purpose.[88] Integrating an SECM tip into an AFM probe is achieved by hand by etching a metal wire,[24,89] thus forming the AFM imaging tip, that is bent and flattened before being insulated by a film that exposes the end of the tip during curing.[25] This part is important, since only the tip apex is revealed, and since the insulating coating must have no pinholes in order to act as an effective SECM electrode.

Combined SECM-SICM,[90,91] uses a pipette with two components; one open channel filled with electrolyte solution and used for topographic measurements to provide the feedback by SICM, and another solid electrode for electrochemical imaging, by SECM. This could be in the form of a double-barrelled theta pipette, with one barrel filled with pyrolysed carbon,[92] or a single barrel pipette with a surrounding ring-disk[91] or half ring electrode.[90]

1.4.9 Resolution of SECM

Heterogeneous electroactivity of electrodes can be examined using such techniques as IC-SECM and SECCM. Certain materials will have heterogeneities that require higher resolution in order to observe this. The development of smaller tips will push the resolution of such techniques to new limits. Kim *et al.*[93] reported the first image of an individual single-walled carbon nanotube (SWNT) using SECM. Kim imaged a SWNT with a diameter of 1.6 nm, using a 1.5 μm tip, with position determined to 100 nm (which was significantly higher using a 10 μm tip). This was carried out in feedback mode, which requires efficient mass transport at the nanotube that is not directly under the tip. There was sufficient area of nanotube at either side of the tip to regenerate the redox mediator.

With smaller tips, and techniques that bring tips closer to the substrate, piezos require stricter temperature control to enable high resolution imaging of small regions of a sample.[94] The use of IC-SECM with nanoelectrodes is described in Chapter 4, to push the resolution of the technique to the nanoscale. IC-SECM was also used in Chapter 3 for hopping mode imaging, and Chapters 3 and 6 for tip-positioning.

1.5 Carbon-based electrodes

Carbon is a common electrode material as it is largely chemically inert, so may be used under a wide range of conditions. Carbon materials also exhibit wide electrochemical potential windows, meaning a greater variety of reactions can be studied.[95] Carbon electrodes are widely used, for example in sensors for glucose,[96]

fuel cells[97] and for bioanalysis.[98] Despite their widespread use, there is ongoing debate as to which surface features are responsible for electroactivity of carbon electrodes. Typical carbon electrodes include sp^2 allotropes such as highly oriented pyrolytic graphite (HOPG), depicted in Figure 1-16, graphene and carbon nanotubes, and sp^3 allotropes such as doped diamond.

1.5.1 Highly oriented pyrolytic graphite (HOPG)

Graphitic carbon has an sp^2 hybridised structure. Highly oriented pyrolytic graphite (HOPG) is a highly ordered and highly pure graphite material used in electrochemistry (see Figure 1-16). It is made by the decomposition of a gaseous hydrocarbon under high temperature, such as acetylene, followed by pressing the material under high pressure and temperature.

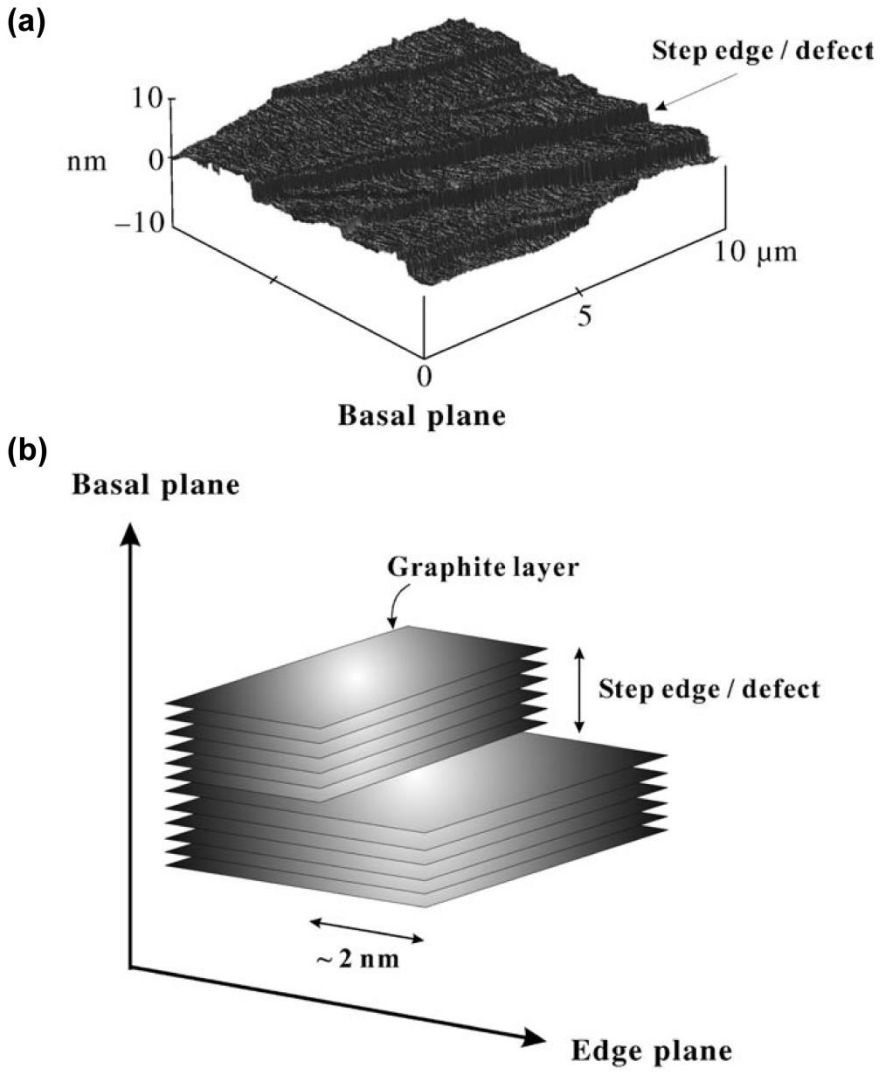

Figure 1-16. AFM image of HOPG (a) and representation of graphite layers at a step edge (b), taken from Ref.[99]

HOPG is described as having a lamellar structure, in which the lateral planes have much stronger forces than the forces between each plane. The highly ordered hexagonal plane of graphite is known as the basal plane. Perpendicular to this is the edge plane, a highly irregular surface of stacked layers of graphite which differs greatly in its electrochemical reactivity due to the different chemical bonding. HOPG can provide edge plane pyrolytic graphite (EPPG) and basal plane pyrolytic graphite

(BPPG) electrode surfaces, depending upon how the graphitic crystal is cut. The basal plane can be readily cleaved, usually by the scotch tape method, to reveal a basal surface that is not perfect. This surface will have defects in the form of surface defects and step edge defects, as shown in Figure 1-16.

HOPG displays fast heterogeneous electron transfer kinetics,[100-104] although electrode kinetics have been widely considered to be much faster on edge plane graphite than basal plane,[105] although this is a topic of debate in the literature.[69,79,80,104,106-112] HOPG is commercially available in various grades, depending on the surface quality. High grades of HOPG have fewer surface defects and step edges, and are more highly ordered than lower grades.[107,113] Since the highest grades are much more expensive than the lowest grades, the preference of grade to use will depend on the desired application. The density and purity do not vary across grades, and purity is much higher than that of naturally occurring graphite.

The highest grades (available from SPI Supplies) are ZYA and SPI-1, which are similar in quality and possess excellent crystallinity with a typical grain size of about 3 mm. A higher-quality (but ungraded) sample originating from Dr. A. Moore (Union Carbide, now GE Advanced Ceramics), denoted in this thesis as AM grade HOPG, will also be studied. ZYB and SPI-2 are high grades of similar quality, for general use, with typical grain sizes up to 0.5 mm. The lowest grades are ZYH and SPI-3, with grain sizes no more than 30-40 nm. Two samples of HOPG were studied in Chapter 5, described in Section 2.4.1; AM grade and SPI-3 grade HOPG.

1.5.2 Carbon nanotubes

Graphene is essentially a single layer of graphite, one atom thick. It is a two-dimensional (2D) layer of carbon atoms in a honeycomb arrangement with high electronic transport, that was first isolated by Geim in 2004.[114] Most recently, single sheets of graphene have been isolated.[115] Carbon nanotubes (CNTs), which can be envisaged as rolled up sheets of graphene, are also interesting as an electrode material.[116] They can either be single-walled carbon nanotubes (SWNTs) or multi-walled carbon nanotubes (MWNTs). It is still unclear which features of CNTs are responsible for electrochemical activity, and if this is different for SWNTs and MWNTs.[117] The features of MWNTs can be considered as being similar to the surface features of HOPG; the open ends of MWNTs have been likened to the highly active edge plane steps on the surface of HOPG, whilst the tube walls have been likened to the basal plane of HOPG.[118]

CNTs have found applications in polymer composite materials, supercapacitors and are expected to be used in nanometre sized electronic devices.[119] SWNT networks of as low as 1 % surface coverage, considered high density networks, have been shown to behave as a thin metallic film, with experimental approach curves showing they behave as electrical conductors of uniform activity.[120] Simulations by Wilson *et al.*[120] showed that the heterogeneities in diffusion to the substrate were largely insignificant based on typical tip-substrate separations used in SECM. Higher resolution techniques may show that these heterogeneities become more significant.

1.5.3 Glassy carbon

Glassy carbon (GC) is a harder form of graphitic carbon that has been proposed to consist of ribbon-like sp^2 carbon that contains mostly edge-plane like graphite, as shown in Figure 1-17,[121] although the structure is not properly understood.[122,123] The proposed structure, intertwined ribbons of graphitic planes of limited size, shown in Figure 1-17, has an intraplanar microcrystalline size, L_a, and interplanar microcrystalline size, L_c, in the range of 30 – 70 Å. This interwoven ribbon structure means that GC is much harder than HOPG.

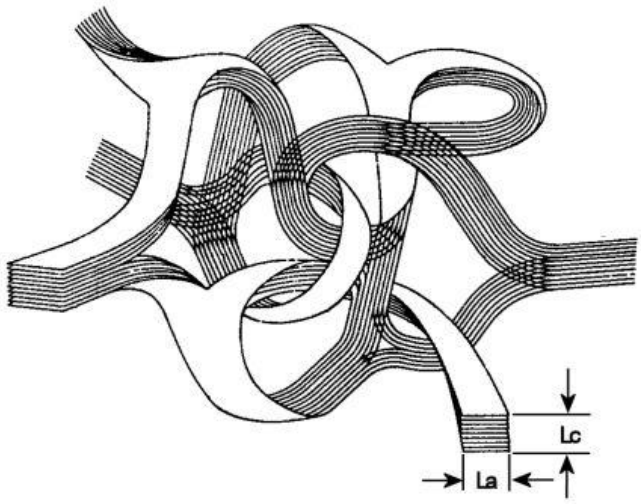

Figure 1-17. Proposed structure of glassy carbon, taken from Ref.[121]

To produce a pristine and clean surface, GC can be 'fractured' to give very high electrochemical activity and low surface oxide coverage.[124,125] 'Fracturing' the electrode is usual impractical, so polishing is a reasonable alternative, although the edges are usually terminated by oxides. Polishing may be responsible for deactivation of the surface of a GC electrode, depending on the cleanliness of the procedure and the removal of polishing debris.[124] There is also the possibility of

exposing a greater surface area polishing as compared to fracturing, but careful polishing can lead to a clean substrate.[95]

1.5.4 Carbon fibre

Carbon fibre (CF) is a graphitic filament, *ca.* 7 μm in diameter. Their strength, size, structure and biocompatibility have made CFs attractive for use as UMEs, electron transfer kinetic measurements and for *in vivo* voltammetry.

A CF can be made into a disk UME by insulating the walls and exposing the end of a single fibre. CF UMEs may be made by sealing in heat shrinkable polyethylene tubing,[126] or by electropolymerisation with polyoxyphenylene,[127] followed by cutting with a scalpel blade to expose the fibre, or by sealing in glass and micropolishing to reveal the CF.[128] Carbon fibres, of the type used in electrochemistry, are sufficiently disordered graphitic materials that they do not exhibit unusual electronic properties. The method of cutting a carbon fibre will reveal a pristine surface similar to that obtained by 'fracturing' GC.[129,130] Carbon fibre is used as a UME in Chapter 6.

1.5.5 Boron doped diamond

Although studies are primarily aimed at sp^2 carbon allotropes, doped diamond (sp^3 carbon) is also a widely used electrode. The electrical conductivity of pure diamond can be increased with the introduction of foreign dopant atoms such as boron, thus making it a much more attractive electrode material. The surface of polycrystalline boron doped diamond (pBDD) has been shown to have heterogeneous activity, as shown using SECM by Neufeld and O'Mullane,[131] and by field emission (FE)-

scanning electron microscopy (SEM) images of silver electrodeposited on diamond by Colley *et al*.[132]

1.6 Metal nanoparticles

The study of metal nanoparticles is important because when the critical dimensions of a material are reduced to the nanoscale, the properties of that material also change, which can lead to novel applications. Nanoparticles can be prepared via a host of different methods. Here, the fundamental processes that occur in the electrodeposition of nanoparticles, a process common for electrodecorating a substrate such as carbon, are considered.

1.6.1 Electrodeposition

There are several key stages in the growth of a layer of atoms over an electrode surface, as shown in Figure 1-18.[133] Firstly, separate nuclei are formed on the surface. It has been proposed that these nuclei form at defects and grain boundaries in materials such as diamond, although this is still a topic of lively debate.[134] This will be examined in Chapter 5, for the case of HOPG, also a topic of debate.[100,101,103,135,136] Secondly, these isolated nuclei will grow. Further nucleation at new sites may also occur. Next, as the isolated growth centres continue to grow, they will begin to overlap. In time, this will result in a continuous layer over the entire cathode surface. This layer will thicken over time as growth continues, with potential control.

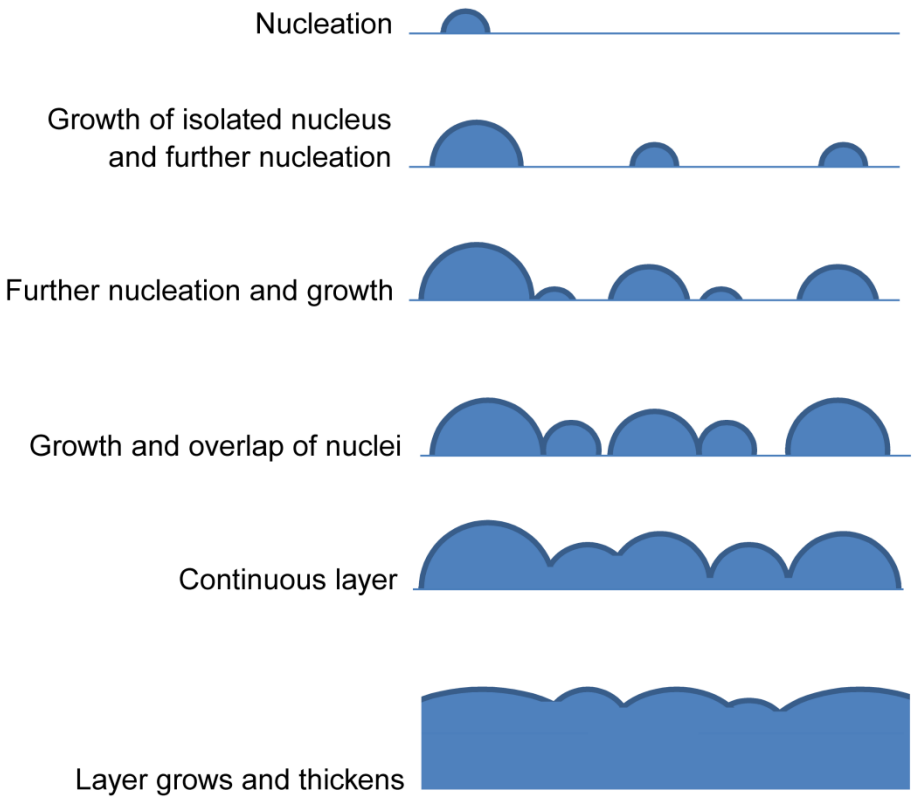

Figure 1-18. Growth process in the electrodeposition of a metal on an electrode surface, following a progressive nucleation mechanism.

Deposition of metals onto a cathode is relatively common and has important industrial applications, ranging from galvanics (batteries) to microelectronics (micrometre-scale electronic components).

1.6.2 Scharifker-Hills model for nucleation and growth

Scharifker and Hills (S-H) modelled the nucleation and growth current-time transients for multiple nuclei, according to instantaneous or progressive

nucleation.[137] These processes are conveniently analysed by simple analytical expressions. Instantaneous nucleation is described by

$$\frac{I^2}{I_m^2} = \frac{1.9542}{t/t_m}\left\{1-\exp\left[-1.2564(t/t_m)\right]\right\}^2 \quad (1.21)$$

where I is the current density, I_m is the maximum current density, t is time and t_m is the time at the maximum current. Progressive nucleation can be expressed as

$$\frac{I^2}{I_m^2} = \frac{1.2254}{t/t_m}\left\{1-\exp\left[-2.3367(t/t_m)^2\right]\right\}^2 \quad (1.22)$$

These current-time transients are shown in Figure 1-19.

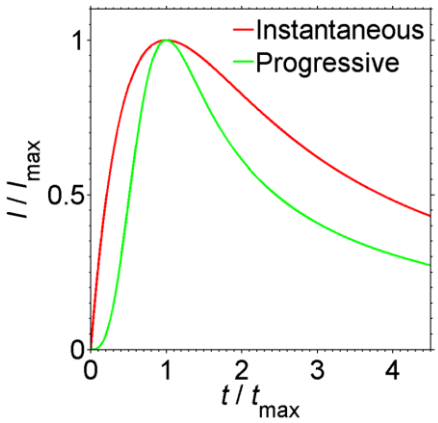

Figure 1-19. Current-time transients for the Scharifker and Hills models for instantaneous and progressive nucleation.[137]

The S-H model also predicts number of nucleation sites, with the following two equations for instantaneous nucleation

$$I_m = 0.6382zFDc^*(kN)^{1/2} \quad (1.23)$$

$$t_m = \frac{1.2564}{N\pi kD} \tag{1.24}$$

where A is the surface area of the electrode, zF is the molar charge, D is the diffusion coefficient, c^* is the bulk concentration, N is the nuclei density (number of nuclei per surface area), and k is a given by the following equation

$$k = \left(\frac{8\pi c^* M}{\rho} \right)^{1/2} \tag{1.25}$$

where M and ρ are the molecular weight and density of the deposited material, respectively.

For the case of progressive nucleation, the following equations will apply

$$I_m = 0.4615 zFD^{3/4} c^* (k' A N_\infty)^{1/4} \tag{1.26}$$

$$t_m = \left(\frac{4.6733}{A N_\infty \pi k' D} \right)^{1/2} \tag{1.27}$$

$$k' = \frac{4}{3} \left(\frac{8\pi c^* M}{\rho} \right)^{1/2} \tag{1.28}$$

where N_∞ is the number density of active sites.

The S-H analysis of current-time transients is performed on data obtained for the electrodeposition of silver nanoparticles on HOPG in Chapter 5.

1.7 Experimental imaging techniques

A range of non-electrochemical imaging techniques have been applied to systems in this thesis. These are discussed here.

1.7.1 Optical microscopy

An optical microscope (OM) employs optical lenses and visible light to magnify an object. The limit of resolution is determined by the wavelength of light. Violet light (λ ~400 nm) would give a resolution of 200 nm. Optical microscopes were required for characterisation of samples with features greater than 1 μm, *e.g.* UMEs and gold bands, and for tip-positioning over samples in SECM. Electrons have much smaller wavelengths, hence electron microscopes achieve much greater resolution than optical microscopes, but the resolution is no longer limited by the wavelength of radiation, rather by practical limitations of the electronic lens used.

1.7.2 Field emission-scanning electron microscopy (FE-SEM)

Scanning electron microscopy (SEM) is used to obtain information such as topography, electrical conductivity and composition of conducting samples. Field emission (FE) refers to the electron gun, and is this is the most expensive and complicated type of gun used, the others being a tungsten filament or lanthanum hexaboride (LaB_6) crystal. It requires an ultra-high vacuum (UHV), < 10^{-7} Pa, and uses the effect of having an enhanced electric field at a small sharp tip, which is very important for resolution in scanning systems.[138] This results in increased spatial resolution and decreased damage to the surface. The electrons are focused by a

condenser lens, controlled by the beam current, before passing through scan coils which deflect the beam to produce a raster scan, controlled by the magnification. The objective lens focuses the probe to its final size, which will change the working distance. As the incident electron beam (primary electrons) hits the surface, they cause secondary electrons to be emitted from the sample, which come from close to the surface. These are detected to produce an image. An in-lens detector can be used, which is situated in the pole of the primary beam, to avoid shadowing effects due to the position of the detector.

This technique was used to image samples such as silver nanoparticles in Chapter 5 and to verify tip and UME and nanoelectrode dimensions accurately,[139] in Chapters 3 and 4.

1.7.3 Focused ion beam-scanning electron microscopy (FIB-SEM)

Focused ion beam (FIB)-SEM differs from SEM due to the use of a focussed beam of ions which can be used for the ablation of materials, as well as site-specific analysis and deposition of materials. The ion beam can provide a resolution of less than 10 nm. A Ga^+ ion source is used, which also generates secondary electrons, although material is removed where the ion beam hits the sample. Modern instruments usually use two primary beam sources so that the sample can be imaged without destruction. This technique was used to mill Pt nanoelectrodes in Chapter 4.

1.7.4 Atomic force microscopy

The atomic force microscope (AFM) is a scanning probe microscope introduced by Binnig, Quate and Gerber in 1986,[140] and was an evolution of the scanning tunnelling microscope, introduced in 1982.[141] The technique measures the force of interaction between an atomically sharp tip, attached to a cantilever, and a substrate to deduce topography.[140] It is simple in design, with a very sharp atomic tip on the end of a cantilever. The tip moves across the surface, and the interaction it experiences with the surface causes the cantilever to deflect. This deflection is monitored by a laser beam focused on the cantilever, directly above the tip (Figure 1-20).

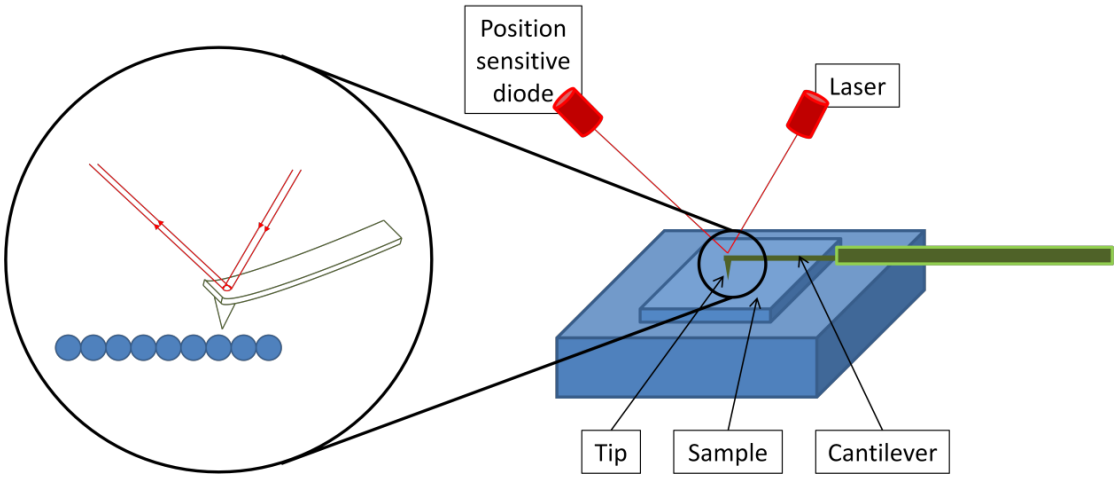

Figure 1-20. Basic principle of atomic force microscopy.

AFM has two main modes of imaging: contact mode (CM) and tapping mode (TM). The former involves moving the tip across the surface, with the tip in contact with the surface, whilst the latter involves oscillating the cantilever (and tip), close to its

resonant frequency. Both modes employ a feedback system. In contact mode, a constant force is maintained so that the tip traces the contours of the surface, whilst in tapping mode, the amplitude of the oscillations is kept constant. In contact mode, the deflection of the cantilever is used to measure this force, whereas in tapping mode it is the amplitude of vibration of the cantilever that is used. AFM was used to characterise gold band samples used in Chapters 3 and 4, and to examine HOPG after electrodeposition experiments in Chapter 5.

1.8 Aims of study

A major theme in this thesis is to improve the resolution and information attainable using SECM. This is achieved by using IC-SECM as a means of feedback, which can be used in conjunction with smaller electrodes, approaching nanoscale imaging.

After a detailed discussion of experimental methods and instrumentation in **Chapter 2**, **Chapter 3** is about implementing a hopping imaging mode that uses IC-SECM to obtain more information (hence more images) during a scan. Also in this chapter, the use of IC-SECM as non-electrochemical means of tip-substrate feedback on a calcite crystal, to permit a new acid-induced dissolution experiment, is described.

Chapter 4 describes the characterisation of nanoelectrodes and their use with IC-SECM in order to push the resolution of SECM. Nanoelectrodes are fabricated and exposed using FIB milling, and characterised using FEM modelling, SEM imaging and voltammetry.

Chapter 5 covers an investigation into the nucleation and growth of metal nanoparticles, as well as a re-examination of the role of surface sites on HOPG towards the electrodeposition process. This study uses SECCM to examine the basal plane of HOPG, in isolation of step edges. Also, macroscopic measurements in a large droplet compares HOPG of different step edge densities, in order to probe the role of step edge sites in silver electrodeposition.

Chapter 6 looks at quinone electron transfer kinetics on carbon fibre and gold UMEs, with particular focus on fouling processes that inhibit the effective rate of the electrochemical reaction. This study aimed to measure kinetic differences of quinone

compounds on these different materials, although progressed to consider the electrode fouling effects on accurate measurements. Again, this work utilised IC-SECM as non-electrochemical means of tip-substrate feedback, in order to reduce the effects of tip-fouling during tip-positioning.

Chapter 7 provides brief conclusions on the research.

1.9 References

(1) Brett, C. M. A.; Brett, A. M. O. *Electrochemistry: Principles, Methods, and Applications*; Oxford University Press, 1993.

(2) Compton, R. G.; Sanders, G. H. W. *Electrode Potentials*; OUP Oxford, 1996.

(3) Bard, A. J.; Faulkner, L. R. *Electrochemical Methods: Fundamentals and Applications*; 2nd ed.; John Wiley & Sons, Inc.: New York, 2001.

(4) Dickinson, E. J. F.; Limon-Petersen, J. G.; Rees, N. V.; Compton, R. G. *J. Phys. Chem. C* **2009**, *113*, 11157.

(5) Compton, R. G.; Banks, C. E. *Understanding Voltammetry*; Imperial College Press, 2011.

(6) Bard, A. J. *J. Am. Chem. Soc.* **2010**, *132*, 7559.

(7) Thirsk, H. R.; Harrison, J. A. *A guide to the study of electrode kinetics*; Academic Press, 1972.

(8) Fisher, A. C. *Electrode Dynamics*; Oxford University Press: Oxford, 2003.

(9) Wightman, R. M.; Wipf, D. O. In *Electroanal. Chem.*; Bard, A. J., Ed.; Marcel Dekker: New York, 1989; Vol. 15, p 267.

(10) Kwak, J.; Bard, A. J. *Anal. Chem.* **1989**, *61*, 1794.

(11) Amphlett, J. L.; Denuault, G. *J. Phys. Chem. B* **1998**, *102*, 9946.

(12) Xiong, H.; Guo, J.; Amemiya, S. *Anal. Chem.* **2007**, *79*, 2735.

(13) Lefrou, C. *J. Electroanal. Chem.* **2006**, *592*, 103.

(14) Lee, Y.; Amemiya, S.; Bard, A. J. *Anal. Chem.* **2001**, *73*, 2261.

(15) Mirkin, M. V.; Bard, A. J. *J. Electroanal. Chem.* **1992**, *323*, 1.

(16) Shao, Y.; Mirkin, M. V.; Fish, G.; Kokotov, S.; Palanker, D.; Lewis, A. *Anal. Chem.* **1997**, *69*, 1627.

(17) Sun, P.; Mirkin, M. V. *Anal. Chem.* **2006**, *78*, 6526.

(18) Ballesteros Katemann, B.; Schuhmann, W. *Electroanalysis* **2002**, *14*, 22.

(19) Zuliani, C.; Walsh, D. A.; Keyes, T. E.; Forster, R. J. *Anal. Chem.* **2010**, *82*, 7135.

(20) Mezour, M. A.; Morin, M.; Mauzeroll, J. *Anal. Chem.* **2011**, *83*, 2378.

(21) Zhang, B.; Galusha, J.; Shiozawa, P. G.; Wang, G.; Bergren, A. J.; Jones, R. M.; White, R. J.; Ervin, E. N.; Cauley, C. C.; White, H. S. *Anal. Chem.* **2007**, *79*, 4778.

(22) Li, Y.; Bergman, D.; Zhang, B. *Anal. Chem.* **2009**, *81*, 5496.

(23) Arrigan, D. W. M. *Analyst* **2004**, *129*, 1157.

(24) Penner, R. M.; Heben, M. J.; Longin, T. L.; Lewis, N. S. *Science* **1990**, *250*, 1118.

(25) Macpherson, J. V.; Unwin, P. R. *Anal. Chem.* **2000**, *72*, 276.

(26) Abbou, J.; Demaille, C.; Druet, M.; Moiroux, J. *Anal. Chem.* **2002**, *74*, 6355.

(27) Bard, A. J.; Fan, F. R. F.; Kwak, J.; Lev, O. *Anal. Chem.* **1989**, *61*, 132.

(28) Sun, P.; Laforge, F. O.; Mirkin, M. V. *Phys. Chem. Chem. Phys.* **2007**, *9*, 802.

(29) Kwak, J.; Bard, A. J. *Anal. Chem.* **1989**, *61*, 1221.

(30) Eckhard, K.; Chen, X.; Turcu, F.; Schuhmann, W. *Phys. Chem. Chem. Phys.* **2006**, *8*, 5359.

(31) Rodríguez-López, J.; Alpuche-Avilés, M. A.; Bard, A. J. *J. Am. Chem. Soc.* **2008**, *130*, 16985.

(32) Amemiya, S.; Bard, A. J.; Fan, F.-R. F.; Mirkin, M. V.; Unwin, P. R. *Annu. Rev. Anal. Chem.* **2008**, *1*, 95.

(33) Mirkin, M. V.; Fan, F.-R. F.; Bard, A. J. *J. Electroanal. Chem.* **1992**, *328*, 47.

(34) Shao, Y.; Mirkin, M. V. *J. Phys. Chem. B* **1998**, *102*, 9915.

(35) Cornut, R.; Lefrou, C. *J. Electroanal. Chem.* **2007**, *604*, 91.

(36) Cornut, R.; Lefrou, C. *J. Electroanal. Chem.* **2007**, *608*, 59.

(37) Galceran, J.; Cecília, J.; Companys, E.; Salvador, J.; Puy, J. *J. Phys. Chem. B* **2000**, *104*, 7993.

(38) Rajendran, L.; Ananthi, S. P. *J. Electroanal. Chem.* **2004**, *561*, 113.

(39) Haram, S. K.; Bard, A. J. *J. Phys. Chem. B* **2001**, *105*, 8192.

(40) Shen, M.; Arroyo-Currás, N.; Bard, A. J. *Anal. Chem.* **2011**, *83*, 9082.

(41) Ludwig, M.; Kranz, C.; Schuhmann, W.; Gaub, H. E. *Rev. Sci. Instrum.* **1995**, *66*, 2857.

(42) Cougnon, C.; Bauer-Espindola, K.; Fabre, D. S.; Mauzeroll, J. *Anal. Chem.* **2009**, *81*, 3654.

(43) Ballesteros Katemann, B.; Schulte, A.; Schuhmann, W. *Electroanalysis* **2004**, *16*, 60.

(44) Etienne, M.; Anderson, E. C.; Evans, S. R.; Schuhmann, W.; Fritsch, I. *Anal. Chem.* **2006**, *78*, 7317.

(45) Lee, Y.; Ding, Z.; Bard, A. J. *Anal. Chem.* **2002**, *74*, 3634.

(46) Buchler, M.; Kelley, S. C.; Smyrl, W. H. *Electrochem. Solid-State Lett.* **2000**, *3*, 35.

(47) Eckhard, K.; Schuhmann, W. *Analyst* **2008**, *133*, 1486.

(48) Zhao, X.; Diakowski, P. M.; Ding, Z. *Anal. Chem.* **2010**, *82*, 8371.

(49) Alpuche-Aviles, M. A.; Wipf, D. O. *Anal. Chem.* **2001**, *73*, 4873.

(50) Kurulugama, R. T.; Wipf, D. O.; Takacs, S. A.; Pongmayteegul, S.; Garris, P. A.; Baur, J. E. *Anal. Chem.* **2005**, *77*, 1111.

(51) Wipf, D. O.; Bard, A. J. *Anal. Chem.* **1992**, *64*, 1362.

(52) Edwards, M. A.; Whitworth, A. L.; Unwin, P. R. *Anal. Chem.* **2011**, *83*, 1977.

(53) Wipf, D. O.; Bard, A. J.; Tallman, D. E. *Anal. Chem.* **1993**, *65*, 1373.

(54) McKelvey, K.; Edwards, M. A.; Unwin, P. R. *Anal. Chem.* **2010**, *82*, 6334.

(55) McGeouch, C.-A.; Peruffo, M.; Edwards, M. A.; Bindley, L. A.; Lazenby, R. A.; Mbogoro, M. M.; McKelvey, K.; Unwin, P. R. *J. Phys. Chem. C* **2012**, *116*, 14892.

(56) Patten, H. V.; Meadows, K. E.; Hutton, L. A.; Iacobini, J. G.; Battistel, D.; McKelvey, K.; Colburn, A. W.; Newton, M. E.; Macpherson, J. V.; Unwin, P. R. *Angew. Chem., Int. Ed.* **2012**, *51*, 7002.

(57) McKelvey, K.; Snowden, M. E.; Peruffo, M.; Unwin, P. R. *Anal. Chem.* **2011**, *83*, 6447.

(58) Hansma, P. K.; Drake, B.; Marti, O.; Gould, S. A.; Prater, C. B. *Science* **1989**, *243*, 641.

(59) Chen, C.-C.; Zhou, Y.; Baker, L. A. *Annu. Rev. Anal. Chem.* **2012**, *5*, 207.

(60) Korchev, Y. E.; Bashford, C. L.; Milovanovic, M.; Vodyanoy, I.; Lab, M. J. *Biophys. J.* **1997**, *73*, 653.

(61) Shevchuk, A. I.; Gorelik, J.; Harding, S. E.; Lab, M. J.; Klenerman, D.; Korchev, Y. E. *Biophys. J.* **2001**, *81*, 1759.

(62) Mann, S. A.; Hoffmann, G.; Hengstenberg, A.; Schuhmann, W.; Dietzel, I. D. *J. Neurosci. Methods* **2002**, *116*, 113.

(63) Gorelik, J.; Ali, N. N.; Sheikh Abdul Kadir, S. H.; Lab, M.; Stojkovic, P.; Armstrong, L.; Sviderskaya, E. V.; Negulyaev, Y. A.; Klenerman, D.; Bennett, D. C.; Lako, M.; Harding, S. E.; Stojkovic, M.; Korchev, Y. E. *Tissue Eng Part C Methods* **2008**, *14*, 311.

(64) Shevchuk, A. I.; Frolenkov, G. I.; Sanchez, D.; James, P. S.; Freedman, N.; Lab, M. J.; Jones, R.; Klenerman, D.; Korchev, Y. E. *Angew. Chem. Int. Ed. Engl.* **2006**, *45*, 2212.

(65) Novak, P.; Li, C.; Shevchuk, A. I.; Stepanyan, R.; Caldwell, M.; Hughes, S.; Smart, T. G.; Gorelik, J.; Ostanin, V. P.; Lab, M. J.; Moss, G. W. J.; Frolenkov, G. I.; Klenerman, D.; Korchev, Y. E. *Nat. Methods* **2009**, *6*, 279.

(66) Li, C.; Johnson, N.; Ostanin, V.; Shevchuk, A.; Ying, L.; Korchev, Y.; Klenerman, D. *Progress in Natural Science* **2008**, *18*, 671.

(67) Pastré, D.; Iwamoto, H.; Liu, J.; Szabo, G.; Shao, Z. *Ultramicroscopy* **2001**, *90*, 13.

(68) McKelvey, K.; Perry, D.; Byers, J. C.; Colburn, A. W.; Unwin, P. R. *Anal. Chem.* **2014**, *86*, 3639.

(69) Williams, C. G.; Edwards, M. A.; Colley, A. L.; Macpherson, J. V.; Unwin, P. R. *Anal. Chem.* **2009**, *81*, 2486.

(70) Böhni, H.; Suter, T.; Schreyer, A. *Electrochim. Acta* **1995**, *40*, 1361.

(71) Suter, T.; Böhni, H. *Electrochim. Acta* **1997**, *42*, 3275.

(72) Suter, T.; Böhni, H. *Electrochim. Acta* **1998**, *43*, 2843.

(73) Ebejer, N.; Schnippering, M.; Colburn, A. W.; Edwards, M. A.; Unwin, P. R. *Anal. Chem.* **2010**, *82*, 9141.

(74) Ebejer, N.; Güell, A. G.; Lai, S. C. S.; McKelvey, K.; Snowden, M. E.; Unwin, P. R. *Annu. Rev. Anal. Chem.* **2013**, *6*, 329.

(75) Snowden, M. E.; Güell, A. G.; Lai, S. C. S.; McKelvey, K.; Ebejer, N.; O'Connell, M. A.; Colburn, A. W.; Unwin, P. R. *Anal. Chem.* **2012**, *84*, 2483.

(76) Patten, H. V.; Lai, S. C. S.; Macpherson, J. V.; Unwin, P. R. *Anal. Chem.* **2012**, *84*, 5427.

(77) Aaronson, B. D. B.; Chen, C.-H.; Li, H.; Koper, M. T. M.; Lai, S. C. S.; Unwin, P. R. *J. Am. Chem. Soc.* **2013**, *135*, 3873.

(78) McKelvey, K.; O'Connell, M. A.; Unwin, P. R. *Chem. Commun.* **2013**, *49*, 2986.

(79) Patel, A. N.; McKelvey, K.; Unwin, P. R. *J. Am. Chem. Soc.* **2012**, *134*, 20246.

(80) Kirkman, P. M.; Güell, A. G.; Cuharuc, A. S.; Unwin, P. R. *J. Am. Chem. Soc.* **2014**, *136*, 36.

(81) Zhang, G.; Kirkman, P. M.; Patel, A. N.; Cuharuc, A. S.; McKelvey, K.; Unwin, P. R. *J. Am. Chem. Soc.* **2014**, *136*, 11444.

(82) Byers, J. C.; Güell, A. G.; Unwin, P. R. *J. Am. Chem. Soc.* **2014**, *136*, 11252.

(83) Lai, S. C. S.; Dudin, P. V.; Macpherson, J. V.; Unwin, P. R. *J. Am. Chem. Soc.* **2011**, *133*, 10744.

(84) Kranz, C.; Friedbacher, G.; Mizaikoff, B.; Lugstein, A.; Smoliner, J.; Bertagnolli, E. *Anal. Chem.* **2001**, *73*, 2491.

(85) Salomo, M.; Pust, S. E.; Wittstock, G.; Oesterschulze, E. *Microelectron. Eng.* **2010**, *87*, 1537.

(86) Kueng, A.; Kranz, C.; Mizaikoff, B.; Lugstein, A.; Bertagnolli, E. *Appl. Phys. Lett.* **2003**, *82*, 1592.

(87) Dobson, P. S.; Weaver, J. M. R.; Holder, M. N.; Unwin, P. R.; Macpherson, J. V. *Anal. Chem.* **2005**, *77*, 424.

(88) Burt, D. P.; Wilson, N. R.; Weaver, J. M. R.; Dobson, P. S.; Macpherson, J. V. *Nano Lett.* **2005**, *5*, 639.

(89) Nagahara, L. A.; Thundat, T.; Lindsay, S. M. *Rev. Sci. Instrum.* **1989**, *60*, 3128.

(90) Comstock, D. J.; Elam, J. W.; Pellin, M. J.; Hersam, M. C. *Anal. Chem.* **2010**, *82*, 1270.

(91) Takahashi, Y.; Shevchuk, A. I.; Novak, P.; Murakami, Y.; Shiku, H.; Korchev, Y. E.; Matsue, T. *J. Am. Chem. Soc.* **2010**, *132*, 10118.

(92) Takahashi, Y.; Shevchuk, A. I.; Novak, P.; Zhang, Y.; Ebejer, N.; Macpherson, J. V.; Unwin, P. R.; Pollard, A. J.; Roy, D.; Clifford, C. A.; Shiku, H.; Matsue, T.; Klenerman, D.; Korchev, Y. E. *Angew. Chem., Int. Ed.* **2011**, *50*, 9638.

(93) Kim, J.; Xiong, H.; Hofmann, M.; Kong, J.; Amemiya, S. *Anal. Chem.* **2010**, *82*, 1605.

(94) Kim, J.; Shen, M.; Nioradze, N.; Amemiya, S. *Anal. Chem.* **2012**, *84*, 3489.

(95) McCreery, R. L. *Chem. Rev.* **2008**, *108*, 2646.

(96) Kang, X.; Mai, Z.; Zou, X.; Cai, P.; Mo, J. *Anal. Biochem.* **2007**, *363*, 143.

(97) Lebert, M.; Kaempgen, M.; Soehn, M.; Wirth, T.; Roth, S.; Nicoloso, N. *Catal. Today* **2009**, *143*, 64.

(98) Honeychurch, K. C.; Hart, J. P.; Pritchard, P. R. J.; Hawkins, S. J.; Ratcliffe, N. M. *Biosens. Bioelectron.* **2003**, *19*, 305.

(99) Ji, X.; Banks, C. E.; Crossley, A.; Compton, R. G. *ChemPhysChem* **2006**, *7*, 1337.

(100) Zoval, J. V.; Stiger, R. M.; Biernacki, P. R.; Penner, R. M. *J. Phys. Chem.* **1996**, *100*, 837.

(101) Miranda-Hernandez, M.; Gonzalez, I.; Batina, N. *J. Phys. Chem. B* **2001**, *105*, 4214.

(102) Porter, J. D.; Robinson, T. O. *J. Phys. Chem.* **1993**, *97*, 6696.

(103) Pötzschke, R. T.; Gervasi, C. A.; Vinzelberg, S.; Staikov, G.; Lorenz, W. J. *Electrochim. Acta* **1995**, *40*, 1469.

(104) McCreery, R. L.; McDermott, M. T. *Anal. Chem.* **2012**, *84*, 2602.

(105) Banks, C. E.; Compton, R. G. *Analyst* **2006**, *131*, 15.

(106) Lai, S. C. S.; Patel, A. N.; McKelvey, K.; Unwin, P. R. *Angew. Chem., Int. Ed.* **2012**, *51*, 5405.

(107) Patel, A. N.; Collignon, M. G.; O'Connell, M. A.; Hung, W. O. Y.; McKelvey, K.; Macpherson, J. V.; Unwin, P. R. *J. Am. Chem. Soc.* **2012**, *134*, 20117.

(108) Anne, A.; Cambril, E.; Chovin, A.; Demaille, C.; Goyer, C. *ACS Nano* **2009**, *3*, 2927.

(109) Lhenry, S.; Leroux, Y. R.; Hapiot, P. *Anal. Chem.* **2012**, *84*, 7518.

(110) Patel, A. N.; Tan, S.-y.; Miller, T. S.; Macpherson, J. V.; Unwin, P. R. *Anal. Chem.* **2013**, *85*, 11755.

(111) Edwards, M. A.; Bertoncello, P.; Unwin, P. R. *J. Phys. Chem. C* **2009**, *113*, 9218.

(112) Lee, C.-Y.; Guo, S.-X.; Bond, A. M.; Oldham, K. B. *J. Electroanal. Chem.* **2008**, *615*, 1.

(113) Patel, A. N.; Tan, S.-y.; Unwin, P. R. *Chem. Commun.* **2013**, *49*, 8776.

(114) Novoselov, K. S.; Geim, A. K.; Morozov, S. V.; Jiang, D.; Zhang, Y.; Dubonos, S. V.; Grigorieva, I. V.; Firsov, A. A. *Science* **2004**, *306*, 666.

(115) Stankovich, S.; Dikin, D. A.; Dommett, G. H. B.; Kohlhaas, K. M.; Zimney, E. J.; Stach, E. A.; Piner, R. D.; Nguyen, S. T.; Ruoff, R. S. *Nature* **2006**, *442*, 282.

(116) Wildgoose, G. G.; Banks, C. E.; Leventis, H. C.; Compton, R. G. *Microchim. Acta* **2006**, *152*, 187.

(117) Dumitrescu, I.; Unwin, P. R.; Macpherson, J. V. *Chem. Commun.* **2009**, 6886.

(118) Banks, C. E.; Moore, R. R.; Davies, T. J.; Compton, R. G. *Chem. Commun.* **2004**, 1804.

(119) Baughman, R. H.; Zakhidov, A. A.; de Heer, W. A. *Science* **2002**, *297*, 787.

(120) Wilson, N. R.; Guille, M.; Dumitrescu, I.; Fernandez, V. R.; Rudd, N. C.; Williams, C. G.; Unwin, P. R.; Macpherson, J. V. *Anal. Chem.* **2006**, *78*, 7006.

(121) Jenkins, G. M.; Kawamura, K. *Nature* **1971**, *231*, 175.

(122) McDermott, M. T.; McDermott, C. A.; McCreery, R. L. *Anal. Chem.* **1993**, *65*, 937.

(123) McDermott, M. T.; McCreery, R. L. *Langmuir* **1994**, *10*, 4307.

(124) Rice, R.; Allred, C.; McCreery, R. *J. Electroanal. Chem.* **1989**, *263*, 163.

(125) Allred, C. D.; McCreery, R. L. *Anal. Chem.* **1992**, *64*, 444.

(126) Hernández, L.; Hernández, P.; Patón, F. *Anal. Chim. Acta* **1996**, *327*, 117.

(127) Miller, T. S.; Macpherson, J. V.; Unwin, P. R. *J. Electroanal. Chem.* **2014**, *729*, 80.

(128) Kelly, R. S.; Wightman, R. M. *Anal. Chim. Acta* **1986**, *187*, 79.

(129) Kawagoe, K. T.; Zimmerman, J. B.; Wightman, R. M. *J. Neurosci. Methods* **1993**, *48*, 225.

(130) Hsueh, C. C.; Brajter-Toth, A. *Anal. Chem.* **1993**, *65*, 1570.

(131) Neufeld, A. K.; O'Mullane, A. P. *J. Solid State Electrochem.* **2006**, *10*, 808.

(132) Colley, A. L.; Williams, C. G.; D'Haenens Johansson, U.; Newton, M. E.; Unwin, P. R.; Wilson, N. R.; Macpherson, J. V. *Anal. Chem.* **2006**, *78*, 2539.

(133) Pletcher, D. *A First Course in Electrode Processes*; 2 ed.; The Royal Society of Chemistry: Cambridge, 2009.

(134) Edwards, M. A.; Bertoncello, P.; Unwin, P. R. *J. Phys. Chem. C.* **2009**, *113*, 9218.

(135) Penner, R. M. *J. Phys. Chem. B* **2002**, *106*, 3339.

(136) Boxley, C. J.; White, H. S.; Lister, T. E.; Pinhero, P. J. *J. Phys. Chem. B* **2002**, *107*, 451.

(137) Scharifker, B.; Hills, G. *Electrochim. Acta* **1983**, *28*, 879.

(138) Crewe, A. V.; Eggenberger, D. N.; Wall, J.; Welter, L. M. *Rev. Sci. Instrum.* **1968**, *39*, 576.

(139) Dumitrescu, I.; Unwin, P. R.; Wilson, N. R.; Macpherson, J. V. *Anal. Chem.* **2008**, *80*, 3598.

(140) Binnig, G.; Quate, C. F.; Gerber, C. *Phys. Rev. Lett.* **1986**, *56*, 930.

(141) Binnig, G.; Rohrer, H.; Gerber, C.; Weibel, E. *Appl. Phys. Lett.* **1982**, *40*, 178.

2 Experimental

This Chapter details the materials and chemicals used, the instrumentation and experimental setup, and the procedures undertaken. Since a large part of Chapter 3 and Chapter 4 involve the implementation of new techniques, these are also described in detail here.

2.1 Materials and chemicals

Table 2-1. Chemicals used within this thesis, including purity and supplier name.

Chemicals	Commercial source
2-(*p*-tolysulfinyl)cyclohexane-2,5-diene-1,4-dione)	Synthesised at Universidad Autónoma de Madrid, Spain, courtesy of Dr. Raúl Díaz
Acetone, ≥98%	Sigma-Aldrich
Anthraquinone, 98%	Acros Organics
Deionized water (resistivity 18.2 MΩ cm at 25 °C)	Millipore Milli-Q system and Select HP, Purite system
Ferrocenylmethyltrimethylammonium ($FcTMA^+$) iodide, 99 %	Strem Chemicals, Inc.
Iceland spar calcite (naturally occurring from Creel, Mexico)	Richard Tayler Minerals
Nitric acid, laboratory reagent grade, 70 %	Fischer Scientific
p-benzoquinone, reagent grade, ≥98%	Sigma-Aldrich
Perchloric acid, 70%	Acros Organics
Potassium chloride, ACS reagent grade, 99.0 – 100.5 %	Sigma-Aldrich
Potassium nitrate, ≥ 99.995 %	Sigma-Aldrich
Silver hexafluorophosphate ($AgPF_6$), 99 %	Strem Chemicals, Inc.
Silver nitrate ($AgNO_3$), ACS reagent grade, ≥99.0 %	Sigma-Aldrich
Sulfuric acid, 99.999%	Sigma-Aldrich
Tetrabutylammonium hexafluorophosphate for electrochemical analysis, ≥99.0%	Sigma-Aldrich

Table 2-2. Materials used within this thesis, including supplier name.

Materials	**Commercial source**
0.025 mm diameter annealed platinum wire, 99.99 %	Goodfellow
0.025 mm diameter hard gold wire, 99.99+ %	Goodfellow
Borosilicate glass capillaries (1.16 mm inner diameter; 2.00 mm outer diameter, 10 cm length)	Harvard Apparatus Ltd.
Copper wire, 0.25 mm diameter, annealed 99.9 %	Goodfellow
HOPG (AM) kindly provided by Prof. R. L. McCreery (University of Alberta, Canada).	GE Advanced Ceramics
HOPG (SPI-3 grade)	SPI Supplies (Aztech Trading)
Microcloth pad, pressure sensitive adhesive (PSA) backed	Buehler
MicroPolish II powder, 0.05 μm particle size	Buehler
Pd wire, 0.25 mm, 99.9 %	VWR International Ltd.
Quartz capillaries (0.50 mm inner diameter; 1.00 mm outer diameter; 10 cm length)	Intracell
Quartz theta capillaries (0.90 mm inner diameter; 1.20 mm outer diameter; 7.5 cm length)	Intracell
Silver conductive paint	RS Components
Solder (60:40 tin:lead alloy)	RS Components
Wollaston wire, 0.002 mm platinum wire, 99.9 %	Goodfellow

2.1.1 Solutions

These comprised 1 mM ferrocenylmethyltrimethylammonium ($FcTMA^+$) hexafluorophosphate, prepared from the metathesis reaction between the iodide salt (Strem Chemicals) and silver hexafluorophosphate (Strem Chemicals), in 0.1 M potassium chloride (KCl, Aldrich, ACS Reagent grade) solution, using water purified (deionised) through a Millipore Milli-Q system (resistivity 18.2 MΩ cm at 25 °C).

2.1.2 Substrates

A gold band array on glass (28 μm width, 22 μm pitch, height 125 nm) and a 25 μm diameter Pt-disk UME were used as substrates for imaging. The Pt UME was micropolished by mounting it on a micrometre, and bringing it into contact with a 0.1 μm diamond lapping disc (PSA, Buehler) fixed on a spinning hard drive (5 200 rpm). The Pt UME was further cleaned using an alumina polishing suspension (MasterPrep 0.05 μm alumina polishing suspension, Buehler).

A gold band, of height 125 nm determined by AFM, on a glass microscope slide was used as a model substrate. The AFM image was recorded in tapping mode using a Veeco Enviroscope with Nanoscope IV controller. The AFM image was processed using the SPIP software package (Image Metrology).

In order to have useful test structures for imaging (*i.e.* gold bands) and to create masks on substrates to expose only a selected area of a sample, the techniques of photolithography, sputtering and evaporation will be used. A photoresist is applied to the sample by spin coating, then the sample is selectively exposed to ultraviolet (UV)

light through a mask. The photoresist may be positive or negative, and this determines whether the resist will become soluble or insoluble in a developer solution. A thin layer (3 nm) of chromium is applied, followed by a layer of gold to the desired thickness, by evaporation onto the substrate, deposited using a Quorum Technologies SC7640 sputter coater. The remaining photoresist and gold is removed in acetone. The mask used produced gold bands on a glass substrate with 25 μm width separated by a 20 μm pitch.

2.2 Electrode fabrication

Macroelectrodes are available commercially, but ultramicroelectrodes and nanoelectrodes still frequently require in-house fabrication, as described here.

2.2.1 25 μm disk diameter ultramicroelectrodes

25 μm diameter Pt-disk and Au-disk UMEs were prepared by sealing the wire in a borosilicate glass capillary (1.16 mm inner diameter (ID); 2.00 mm outer diameter (OD)), following the widely adopted procedure for making ultramicroelectrodes by Wightman and Wipf.[1]

In brief, the capillary was pulled into two using a heated coil micropipette puller (PB-7, Narishige Co. Ltd.), and the pipette end was sealed in a Bunsen flame. A 0.5 cm length of the appropriate ultramicroelectrode wire was inserted into the capillary, and moved to the sealed end by gentle tapping. The glass was melted around the metal wire coil by reinsertion into the micropipette puller's heated coil, whilst under vacuum using rubber tubing of the open end of the capillary. The wire was back-

connected to a larger copper wire (0.25 mm diameter), using solder inserted into the open end and heating with a soldering iron from the outside of the glass capillary. The open end of the capillary was sealed using Araldite, to ensure the connection did not break. The wire core was sealed completely in glass, and was exposed by coarse polishing at the tip of the capillary using 600 grit polishing paper. The sides of the tip were also polished, by coning around the edges with the polishing paper, in order to make sure that the UME was located centrally within the glass sheath and that the *RG* was the desired value.

The tip surface was made flat by mounting it on a micrometre, and bringing it into contact with a 0.1 μm diamond lapping disc (PSA, Buehler) fixed on a spinning hard drive (5 200 rpm). Electrodes were polished until optically flat by hand using an alumina polishing suspension (MasterPrep 0.05 μm alumina polishing suspension, Buehler) on a microcloth polishing pad (Buehler). The alumina suspension was removed by further polishing onto a clean wet microcloth polishing pad.

2.2.2 2 μm disk diameter ultramicroelectrodes

A 2 μm diameter Pt-disk UME was used as the SECM probe, prepared as described elsewhere.[1] The procedure broadly mirrors that of the 25 μm electrodes described above. In brief, Wollaston wire was inserted into the capillary whilst the end of the pulled pipette is still open. This Wollaston wire is a 25 μm Ag wire, with a 2 μm diameter Pt core. Once the Wollaston wire sat at the end of the pipette, the silver coating was removed by dipping into a 30 % nitric acid (diluted from 70 %), and removing the acid and dissolved silver on tissue paper. This acid treatment was repeated until the lower half of the Wollaston wire had the silver completely

removed, whilst the upper half still had Ag on in order to make a secure connection to later. The remaining acid in the pipette was removed by dipping into water ten times, and removing the water on tissue paper. The water and any dirt was removed by dipping into acetone ten times, and removing the acetone on tissue paper. Once the acetone had evaporated, the pipette end was closed by careful heating in a Bunsen flame. From this point, the methodology is the same as for the 25 μm electrode, although greater care should be taken when polishing due to the reduced dimensions of the probe.

The ratio of glass radius to Pt radius (*RG* value) was 10. The electrodes were polished as above on a microcloth polishing pad, and this was done prior to every experiment.

2.2.3 Nanoelectrode fabrication

Nanoelectrode tips, comprising of Pt sealed in glass, were prepared following a closely similar procedure to that described by Zuliani *et al.* [2] which is based on an earlier report,[3] for quartz capillaries (0.50 mm ID; 1.00 mm OD; 10 cm length), using a Sutter P-2000 laser puller with modification of the settings, using two programs:

Program 1:

HEAT = 830 ± 20; FILAMENT = 5; VELOCITY = 255; DELAY = 255; PULL = 0.

Program 2:

HEAT = 690; FILAMENT = 1; VELOCITY = 43; DELAY = 124; PULL = 120.

The procedure, outlined schematically in Figure 2-1, involved placing a 1 cm length 25 μm diameter annealed platinum wire in the centre of a glass capillary (pushed to the middle using a larger copper wire). The capillary was placed in the laser puller, so that the laser beam would hit the Pt wire, and the capillary was clamped in place so that no pulling force was applied during the sealing step (Program 1). Rubber tubing was connected to both ends of the capillary, and a vacuum was applied. After waiting for 1 minute to ensure a good vacuum, Program 1 was run for 40 seconds, followed by 20 seconds when the laser was turned off, to allow the glass to cool and to maintain an optimal laser power. This was repeated so that in total the glass was heated four times. After the final heating of 40 seconds, the vacuum was turned off and the glass was allowed to cool for 1 minute to ensure reproducibility at the pulling stage. The clamps where removed, and the Pt seal in glass capillary was pulled using Program 2 to produce two tapered nanoelectrodes that were sealed in glass.

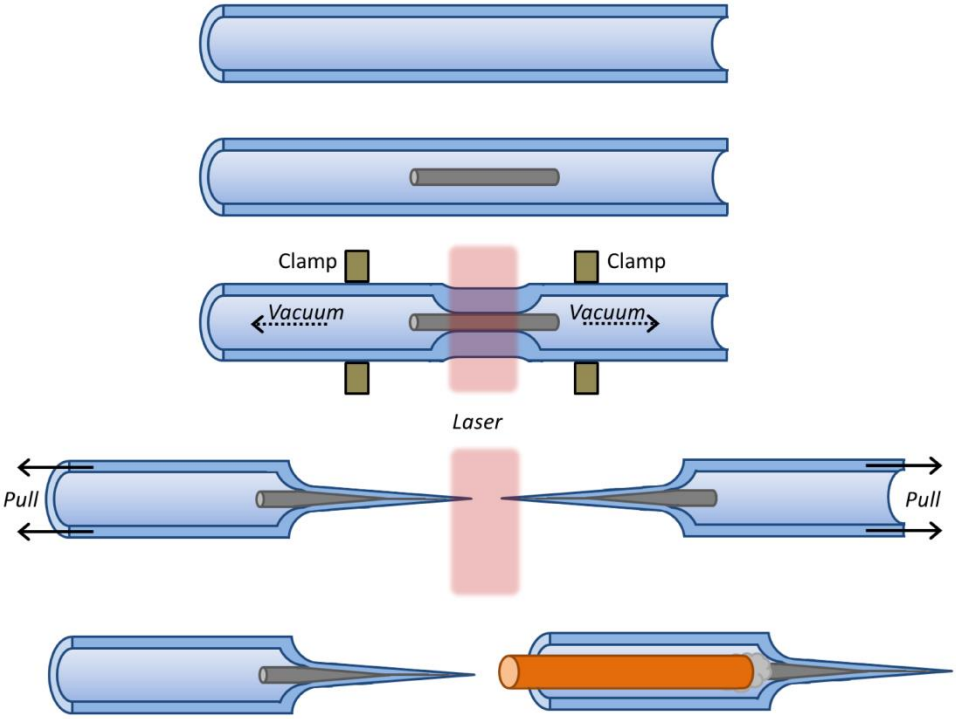

Figure 2-1. Fabrication procedure for nanoelectrodes.

2.2.4 Pt nanoelectrode FIB milling

The Pt was exposed by removing the ends of the nanotips by FIB milling, using a FIB scanning electron microscope (SEM) (JEOL 4500, JEOL), at an accelerating voltage of 5 kV, with positively charged Ga^+ ions at 5 nC μm^{-2}. Low resolution images were obtained using the JEOL system to follow the FIB milling procedure, but higher resolution field emission (FE) SEM micrographs of the tips, for the measurement of critical dimensions, were acquired at 15 kV, using a SUPRA 55 variable-pressure (VP) system (Zeiss). FIB-milled tips with exposed Pt were also shaped, to reduce the *RG* value to around 10, and to ensure that the Pt was located centrally in the glass sheath of the probe. This was done by defining a mask over the

end of the tip, and milling the region inside this, in the same manner as for cutting the tips.

As an extension to the FIB milling procedure, Figure 2-2(b) shows an electrode that has been 'shaped' in the milling process to produce a tip of preferred geometry, *i.e.* smaller *RG* and more central location of the Pt.

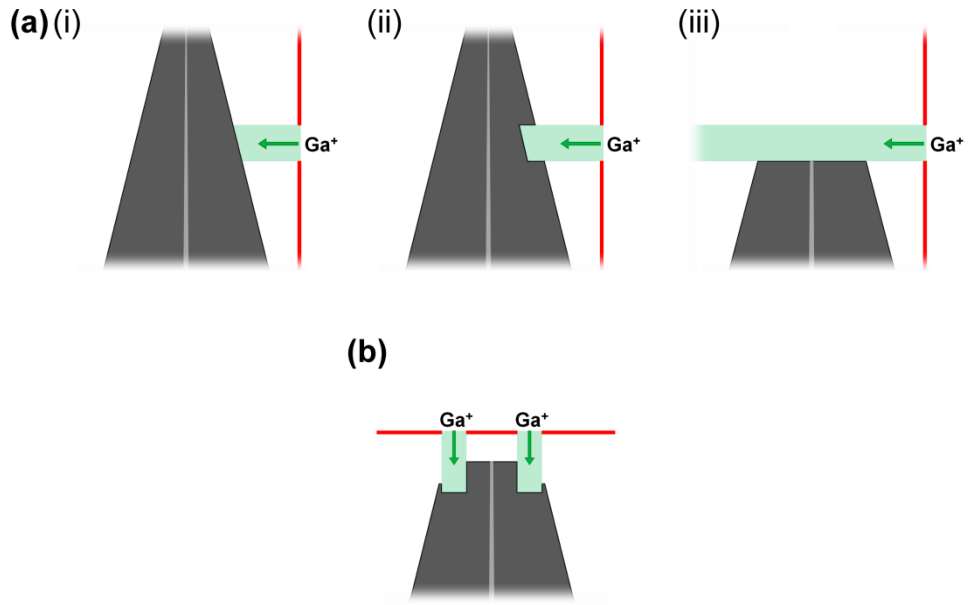

Figure 2-2. Side-view schematic of the FIB-milling procedure (a) showing ablation of a nanoelectrode before (i), during (ii) and after (iii) the milling process. The reducing of the *RG* value of a cut electrode is also shown (b).

2.2.5 SECCM probe fabrication

400 nm theta pipette tips were prepared from quartz theta capillaries (0.90 mm ID; 1.20 mm OD; 7.5 cm length). The capillaries were pulled on the laser puller, using a custom-made two-line program;

Program 3:

HEAT = 830 ± 20; FILAMENT = 5; VELOCITY = 255; DELAY = 255; PULL = 0.

Program 4:

HEAT = 690; FILAMENT = 1; VELOCITY = 43; DELAY = 124; PULL = 120.

2.3 IC-SECM and HIC-SECM

The SECM studies using IC-SECM and HIC-SECM used the same hardware, although the imaging modes used were different, in terms of the scan profile used and the modes of SECM used.

2.3.1 Instrumentation for IC-SECM

The instrument used for the studies herein, for both IC-SECM with nanoelectrodes and HIC-SECM, was modified from the recently reported setup for IC-SECM,[4] specifically in order to implement low-force soft-tapping imaging with nanoelectrodes. A schematic of the modified setup is given in Figure 2-3.

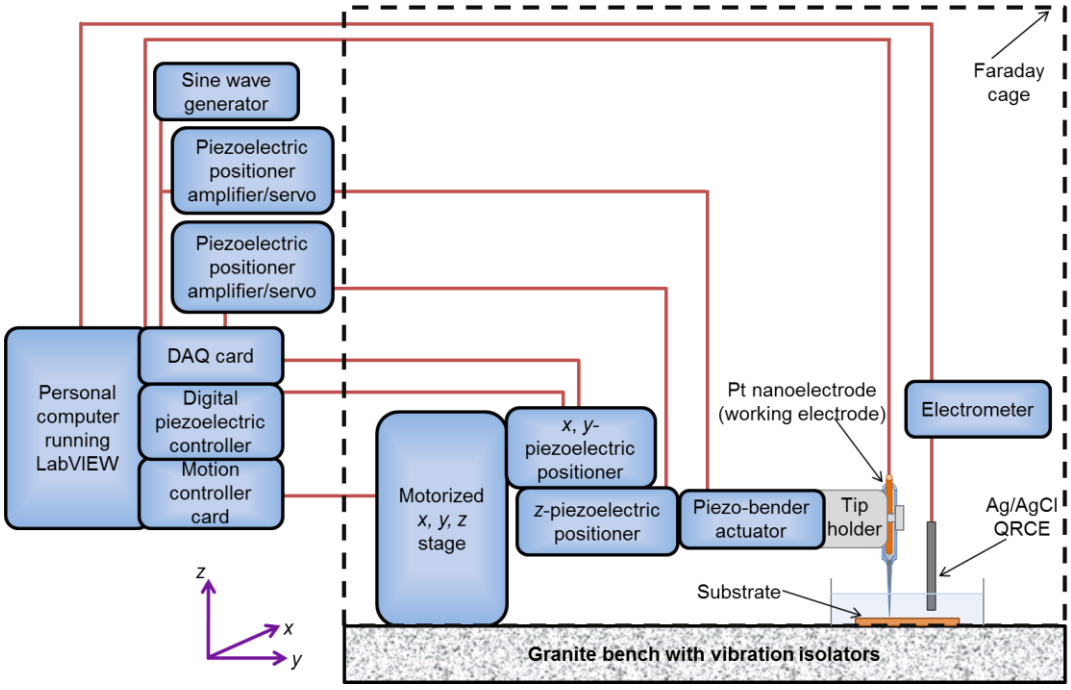

Figure 2-3. Schematic showing the setup of IC-SECM with a piezo-bender actuator.

The principal modification was the addition of a piezo-bender actuator (PICMA P-871.112, Physik Instrumente) with a strain gauge sensor (SGS), to which the SECM tip was mounted directly. This was controlled using an amplifier/servo (E-651.1S, Physik Instrumente). This is shown in Figure 2-4.

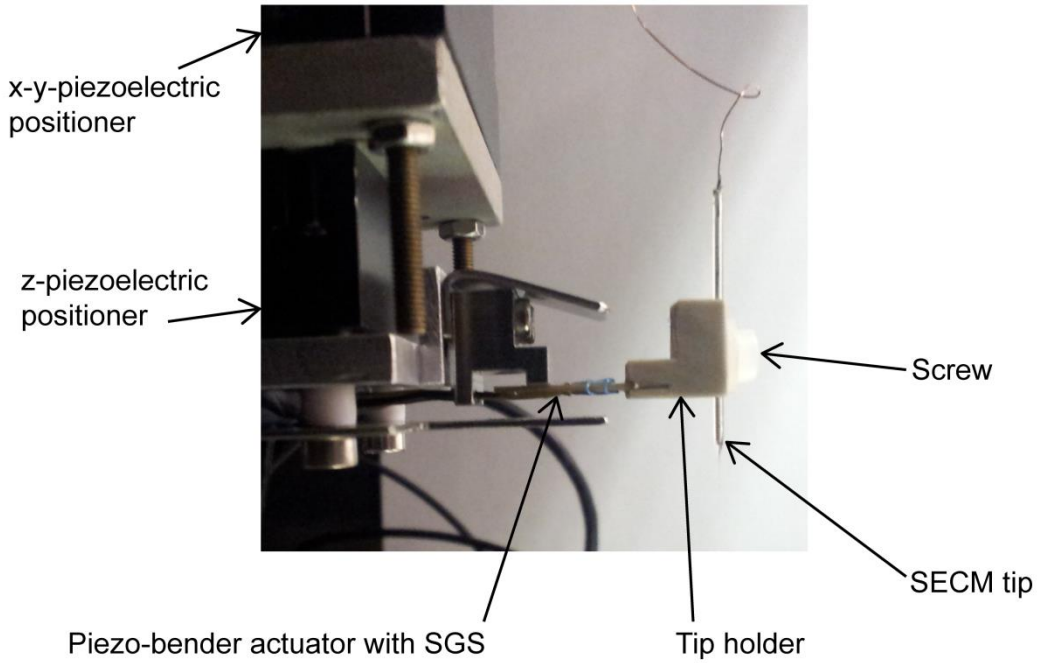

Figure 2-4. Photograph of SECM tip mounted on the piezo-bender actuator, mounted on the *z*-piezoelectric positioner.

Coarse control of the SECM tip, mounted perpendicular to the surface, was realized using a motorized *x*, *y*, *z* translation stage (M-112.1DG, Physik Instrumente) controlled by a motion controller card (C843.41, Physik Instrumente). In order to bring the electrode close to the surface, *i.e.* less than the z-piezo range of 100 μm, a video camera (PL-B776U, Pixelink) was used with a ×2 magnification lens (44 mm, InfiniStix, Edmund Optics).

Fine control was realized by three piezoelectric positioners for closed loop operation: two (*x* and *y*) each with 500 μm total travel (PIHera P-625.2CD, Physik Instrumente), controlled through a digital piezo controller (E761, Physik Instrumente), and one positioner (*z*) with 100 μm travel (PIHera P-621.ZCD, Physik Instrumente) for operation with an amplifier/servo (E.665 LVPZT, Physik Instrumente). The piezoelectric positioner amplifier/servo and digital piezo

controller were controlled through a data acquisition (DAQ) card (NI PCIe-6259, National Instruments) from a PC running custom LabVIEW code (LabVIEW 9.0, National Instruments).

A sinusoidal oscillation (of $\delta\sin(2\pi ft)$ in the position of the tip normal to the surface, about the average height of the tip) was generated using a sine wave generator (Digimess TG100, Digimess) and applied to the piezo-bender actuator and the amplitude of the vertical oscillation of the tip was measured by the SGS.

2.3.2 Electrochemical setup for IC-SECM

An AgCl-coated Ag wire (Ag/AgCl) served as a quasi-reference counter electrode (QRCE) in a two-electrode configuration. The SECM was operated in the feedback mode, by applying a potential of 0.45 V to the Pt nanoelectrode *vs*. the Ag/AgCl QRCE, whilst the substrate was unbiased. This potential corresponded to the diffusion-limited one-electron oxidation of $FcTMA^+$ to $FcTMA^{2+}$ at the tip.

2.3.3 Electrochemical setup for HIC-SECM

An AgCl-coated Ag wire in the 0.1 M KCl electrolyte served as an Ag/AgCl (0.1 M KCl) quasi-reference counter electrode (QRCE), for the feedback mode studies, in a simple two-electrode configuration, with the tip as the working electrode, whilst the substrate was unbiased. The current was measured by a home-built current follower. The DAQ card applied the voltage to the tip electrode *vs*. the Ag/AgCl QRCE, and was used to acquire data. For SG/TC imaging, the potential of both the tip and substrate were controlled using a home-built bipotentiostat. The current at the tip

was measured by a home-built current follower, and the current could also be measured at the substrate.

2.3.4 IC-SECM approach curves and imaging

While oscillated with a small amplitude in *z*, the tip was approached normal to the surface of interest (*z*-direction) using the *z*-piezoelectric positioner. Detection of IC for the tip approach and the imaging process have been described previously in full,[4] but was slightly different here because the piezo-bender actuator was oscillated and used to detect damping rather than the *z*-piezoelectric positioner. In brief, the tip was oscillated at 70 Hz with an amplitude of about 36 nm, and a damping of 5 % in the oscillation amplitude was used as the setpoint for imaging. The scan area was typically 3 μm × 3 μm, with a 0.1 μm step size in each direction. A forward line scan was made in intermittent contact, and a reverse line scan was made at a constant distance of 300 nm from the forward scan *z*-position, using the tip-contact data detected on the forward line scan to set the tip position in *z* on the reverse scan.

The tip height in IC-SECM is updated, for example, every 0.1 μm, by a proportional controller which takes the form:[4]

$$z_{new} = z_{old} + P\left(\delta_{SGS} - \left(1-0.1\right)\delta_{SGSBulk}\right) \qquad (2.1)$$

where z_{new} and z_{old} are the new and old SECM tip heights respectively, P is a scalar, δ_{SGS} and $\delta_{SGSBulk}$ are the oscillation amplitudes of the tip measured by the strain gauge sensor (integrated on the piezo) at the current position and in the bulk solution (away from the surface), respectively. The (1 – 0.1) term represents a damping threshold of 90 %, *i.e.* $\delta_{SGS} = 0.9\ \delta_{SGSBulk}$.

2.3.5 HIC-SECM imaging

3D current images were obtained using a HIC-SECM scan, consisting of a series of approach curves, arranged as a raster scan pattern over the surface (Figure 2-3(a)). The tip current was recorded as a function of *z* as the probe was translated towards the substrate at each point in the *x*-*y* plane. Note that the program used is versatile and could be modified so that the current was recorded on the retract, rather than the approach, or both. Each approach was stopped when IC was detected (*vide supra*), and the tip was retracted by a set amount and moved to the next position. A schematic showing the manner in which approach curves were recorded is given in Figure 2-5(b), while Figure 2-5(c) shows how this is extended in three dimensions across the surface. The *z* step size used in the approach curve was 50 nm, meaning data were recorded every 50 nm in steps normal to the surface. The initial approach at the start of the scan was made from within 100 μm of the surface, and subsequent approaches were performed after a constant retract distance of 5.0 μm.

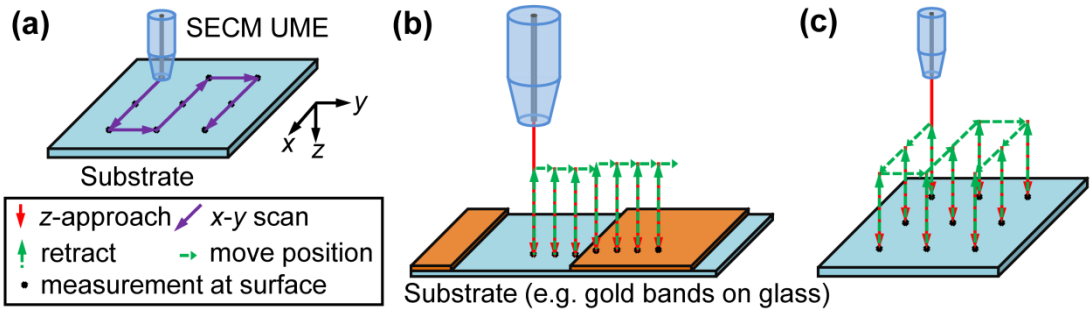

Figure 2-5. Schematics showing: (a) a 2D tip raster scanning pattern over a substrate at a fixed height; (b) a single line scan in HIC-SECM, constituted as a series of approach curves with the current measured on the approach; and (c) the tip movement over a substrate in a full HIC-SECM scan.

The tip was oscillated at a frequency of 70 Hz, with an amplitude in the bulk of 39 nm. An amplitude of 35 nm (*i.e.* 10 % lower) was used as the set point for IC. Three further 50 nm steps were made after the set point for IC was reached to ensure the tip was in contact with the surface and that the damping was well above the noise level. The scan area for all images was 50.0 μm × 50.0 μm, with approach curves performed every 2.0 μm. Hence each image consisted of 676 approach curves (26 in both the *x*- and *y*- directions), each of 100 *z* points (in a 5.0 μm approach for Figure 3-4) or 210 *z* points (in a 10.5 μm approach for Figure 3-8 and Figure 3-9).

Approaches used here were at velocities of about 0.3 μm s^{-1}, which incorporated a 5 ms wait time between each 50 nm step. This is sufficiently slow that the response is at steady-state and there are no convective effects. Cornut *et al*. found the limit before a 2 % deviation from steady-state conditions takes place is about 2.5 μm s^{-1} for a 1 μm radius electrode, although a slightly different diffusion coefficient was used.[5]

2.3.6 Localised proton-promoted etching of calcite via SECM

Naturally occurring single crystals of Iceland spar (Richard Tayler Minerals, UK) were cleaved along the $(10\bar{1}4)$ cleavage plane, using an open Stanley blade (Stanley Tools USA, no. 1992) to produce two freshly exposed faces. One face was used for proton-promoted etching via SECM, while the other 'mirror' face was free-etched in 0.1 M KNO_3 at pH 6 for 60 min, to reveal sub-surface dislocations emerging at the crystal surface.[6] Since all experiments were performed in 0.1 M KNO_3, comparison of the two mirror faces after both types of etching allowed correlation of the local SECM measurements with the corresponding surface properties.

The instrumentation used for SECM measurements was as described above (Section 2.3.1).[7] A 25 μm diameter platinum UME was used as the tip for SECM, with an *RG* value approximately 10.[8] The quasi-reference electrode was a Ag wire coated in AgCl, while the UME acted as the working electrode in a standard two-electrode voltammetric-galvanostatic setup.

Positioning of the tip at a precise distance from the surface was achieved using intermittent contact (IC)-SECM.[4,9] In an approach curve for IC-SECM, the tip was approached normal to the surface, having set the oscillation in the bulk *ca.* δ = 90 nm. IC was determined to be the point at which the oscillation amplitude dropped by 5 %, detected by the bender actuator. The tip was then withdrawn by the distance of 10 μm from the substrate, such that it was sufficiently close for the electrochemical process at the tip to promote dissolution, but also allowed dissolution products to escape; rather than accumulate significantly in the gap between the tip and the surface which might influence the etching process (*e.g.* by promoting back reactions).[7]

A current of 100 nA (204 A m^{-2}) was typically employed to induce the dissolution process, by oxidising water to produce protons, which is a quantitative reaction that allows the precise calculation of the proton flux at the electrode surface.[10] The duration of etching was varied accurately between 1 and 5 minutes. It is important to note that varying the time for dissolution serves to vary the distance between the tip and (dissolving) surface, and hence the mass transport rate, allowing its influence to be determined (*vide infra*). By moving the tip to a new location after each etch, by ≈ 200 μm, numerous etches could be made on one sample. There was naturally some free etching on the SECM-etched surface (at the bulk pH = 6), but this was negligible compared to the SECM-induced proton-promoted dissolution (*vide infra*).

After a series of etches was complete, the calcite sample was rinsed for ≈ 5 seconds in Milli-Q reagent grade water and mounted on a glass slide. This did not cause further significant dissolution, but produced a clear surface for visualisation.

The calcite 'matched faces' (SECM-etched and free-etched) were imaged by optical microscopy, typically at ×200 magnification in DIC (differential interference contrast) mode. SECM etch pits were analysed using white light interferometry (WLI) (WYKO NT-2000 Surface Profiler, WYKO Systems) which required sputter-coating the calcite surfaces with gold (Sputter Coater, Quorum Technologies) to give a layer of ≈ 10 nm. The gold coating thickness was negligible compared with the pit depths (typically over 1 μm). WLI yielded 3D images of localised dissolution pits, from which various parameters could be extracted for numerical modelling of dissolution kinetics (not discussed here).

2.4 Silver electrodeposition on HOPG

2.4.1 Materials

Two grades of HOPG were employed in this study: a high-quality (but ungraded) sample originating from Dr. A. Moore (Union Carbide, now GE Advanced Ceramics), hereafter denoted as AM grade HOPG, kindly provided by Prof. R.L. McCreery (University of Alberta), and an SPI-3 graded sample from SPI Supplies (Aztech Trading, UK). Both HOPG samples were freshly cleaved with adhesive tape before each experiment.

Previously, it has been shown that AM grade HOPG provides surfaces with extensive basal terraces (typically >> 1 μm) and a low coverage of step edges (0.09 % area on average, with respect to the basal surface, mostly of mono-atomic height),[11] whereas SPI-3 has an average step edge coverage of 31% (mostly multilayer steps),[12] a difference of more than two orders of magnitude in step coverage, as shown in Table 2-3.

Table 2-3. Table showing step density and step edge coverage of HOPG samples used.

HOPG grade	**AM**	**SPI-3**
Mean step density / μm^{-1}	0.02 ± 0.02 (range 0.003 – 0.12)	8.0 ± 5.8 (range 2.5 – 21.9)
Average step edge coverage on basal plane	0.09 % (range 0.006 – 0.48 %)	31 ± 24 % (range 10.1 – 78.0 %)

The two samples are shown in Figure 2-6. The AFM image shows SPI-3 HOPG has many more steps and much greater topographical variation compared to the AM grade HOPG. Optical microscopy at lower magnification (×100) shows many more features on the SPI-3 HOPG as compared to AM grade HOPG.

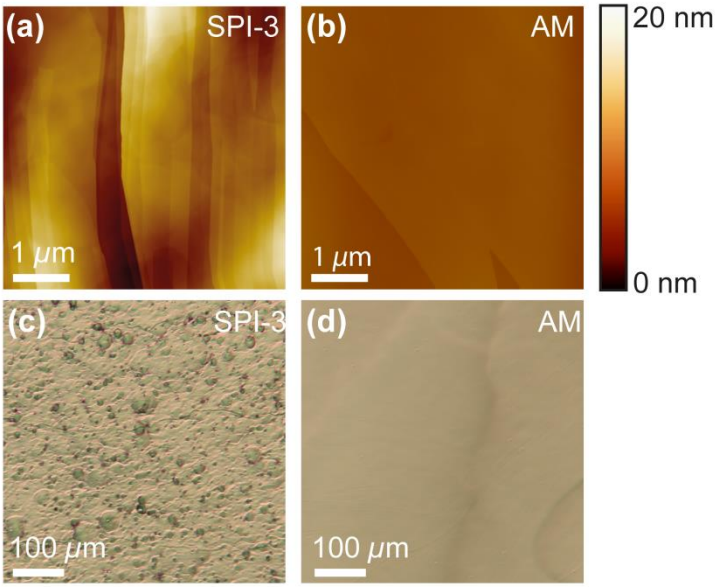

Figure 2-6. AFM images of freshly cleaved SPI-3 HOPG (a) and AM grade HOPG (b). Optical microscopy images of the same freshly cleaved SPI-3 HOPG (c) and AM grade HOPG samples (d).

Solutions were prepared from silver nitrate ($AgNO_3$, Sigma Aldrich, "ACS reagent") with potassium nitrate (KNO_3, Sigma Aldrich, "ReagentPlus") as supporting electrolyte (except in specific cases noted below) in ultra-pure water ("Select HP", Purite, >18 MΩ cm at 25 °C). All materials were used as received, and the concentrations used were always 1 mM $AgNO_3$ in 50 mM KNO_3 (supporting electrolyte), except for the *ex situ* analysis, which omitted the supporting electrolyte.

2.4.2 Macroscale electrochemical measurements

Macroscopic electrochemical measurements were carried out in a droplet, confined by a ¼ inch (6.4 mm) diameter fluorosilicone rubber O-ring gently placed on the HOPG surface, to produce a liquid-tight seal with little to no lateral friction on the

sample. A conventional three-electrode configuration was used, depicted in Figure 2-7, where the HOPG substrate was connected as the working electrode, while a platinum gauze and a silver wire were used as counter and quasi-reference electrodes, respectively. Both the AM and SPI-3 HOPG samples were studied.

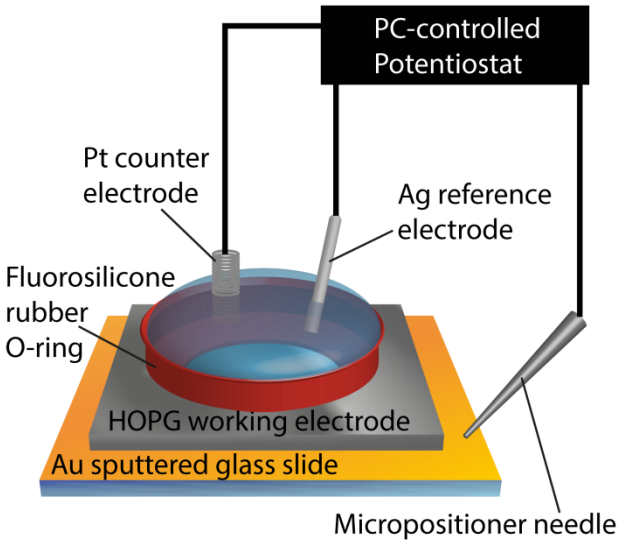

Figure 2-7. Schematic of the experimental setup for macroscale electrochemical measurements.

All potentials herein are reported relative to the Ag/Ag^+ redox couple and can thus be directly related to the overpotential for the silver electrodeposition process. Depositions were performed from a solution of 1 mM $AgNO_3$ in 50 mM KNO_3, with the HOPG electrode held at –100, –170 and –240 mV. Prior to any deposition, immediately after cleaving and during/after solution addition, the surface was held at +400 mV for 180 s to avoid any deposition of silver. Deposition was induced by stepping the HOPG substrate to the potential of interest for defined periods up to 50 s, and recording the current-time response.

For experiments that were followed by *ex situ* microscopy characterisation (see below), the deposition was carried out from a 1 mM $AgNO_3$ solution without supporting electrolyte to minimise salt residues on the sample. In this case, after deposition, the droplet was carefully removed using a Pasteur pipette, and any remaining solution whisked away using a fibre tissue placed at the edge of the sample. The macroscopic chronoamperometric measurements were performed at room temperature (21 ± 2°C) in an air conditioned room, using a computer controlled CHI760A potentiostat (CH Instruments Inc., USA).

2.4.3 Nanoscale measurements

The SECCM setup has been described in detail elsewhere[13] and is shown schematically in Figure 2-8. In short, a theta pipette was pulled to a sharp taper and filled with an electrolyte solution (1 mM $AgNO_3$ in 50 mM KNO_3, with one silver wire placed in each barrel as a quasi-reference counter electrode (QRCE). A small potential bias was applied between the QRCEs before and after each electrodeposition experiment to monitor the resistance of the electrolyte meniscus at the end of the pipette, which is a good indication for the size of the droplet.[14] This was used to verify that the size of the meniscus did not vary appreciably during the experiment, and also to minimise variances between experiments performed with different pipettes. During electrodeposition, the electrochemical current response can be wholly assigned to the contacted area of the substrate, which is comparable to the pipette size (*ca.* 400 nm diameter).[14-17] There was no potential bias between the QRCEs during electrodeposition experiments.

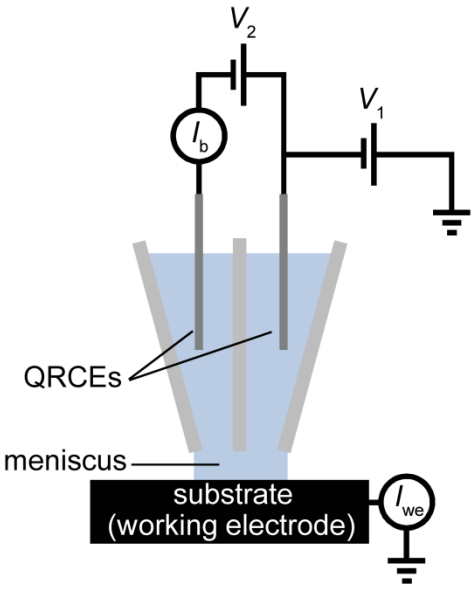

Figure 2-8. Schematic of the experimental setup for microscale experiments using SECCM. A potential bias (V_2) was applied between the quasi-reference counter electrodes (QRCEs) before and after each measurement in a spot on the surface, and the current between them (I_b) was measured to monitor the resistance of the electrolyte droplet. During electrodeposition experiments, no potential bias between the QRCEs was applied (V_2 = 0); rather, both QRCEs were floated by potential V_1 with respect to ground. The substrate (working electrode) was held at ground, and had an effective potential of $-V_1$ with respect to the QRCEs, and the current flowing through it (I_{we}) was measured continuously.

The pipette was mounted above the HOPG sample, which was connected as the working electrode and held at ground, so that its effective potential was set by floating the potential of the QRCEs. Only AM grade HOPG was studied for the nanoscopic experiments, as it has the lowest number of step edge defects and is of high quality.[11] The current flowing through the HOPG sample (working electrode current) was monitored continuously. The pipette was slowly lowered (200 nm s^{-1}) towards the substrate, until a significant current at the HOPG surface (due to double layer charging or silver electrodeposition upon closing the electrical circuit) was

detected, indicative of contact between the electrolyte droplet and the substrate, with no physical contact from the pipette itself. The meniscus was typically held on the surface for one second, while recording the current every 165 μs (the average of 32 separate measurements) on a home-built, high bandwidth current-to-voltage converter, before it was swiftly retracted (1 μm s^{-1}) from the surface (Figure 2-9). Subsequently, the substrate was moved laterally to provide a fresh HOPG area under the pipette, and the pipette was slowly lowered to bring the meniscus into contact again to perform another measurement. This entire procedure was typically repeated five times within *ca*. two minutes, and the measurements were found to be very reproducible (*vide infra*).

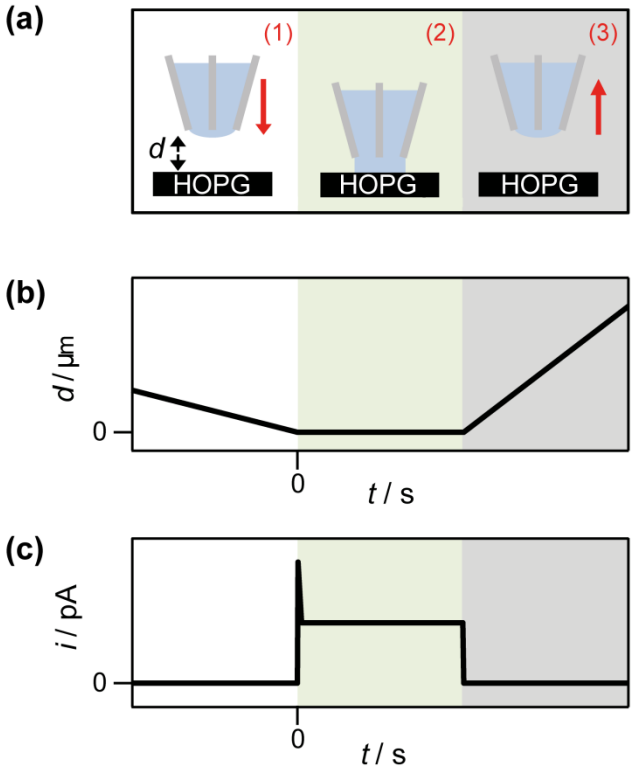

Figure 2-9. Schematic representation of pipette positioning during an electrodeposition experiment (a), together with the corresponding tip-to-substrate separation (b) and current through the HOPG surface (c) as a function of time. (1) The pipette was translated slowly towards the HOPG surface. (2) Once the electrolyte droplet contacted the surface (as witnessed by a current spike), and assigned as $d = 0$, the pipette motion ceased automatically and the pipette was held in place for a predetermined time (typically 1 s). (3) The pipette was then retracted swiftly and moved laterally to approach at the next area. Red arrows denote the direction of movement of the pipette.

After localised electrodeposition, the HOPG surface was examined by FE-SEM. Also, to examine the contents of the capillary, the pipette was translated further into the surface after an electrodeposition, forcing the pipette to break and leave a minute droplet of solution and broken glass on the surface. A control tip breaking experiment was also performed, using only 50 mM KNO_3 (*i.e.* in the absence of

$AgNO_3$) to ensure no electrodeposition. Both tip breaking experiments were inspected by FE-SEM, and electrodeposition features were also characterized by TM-AFM.

2.4.4 *Ex situ* characterisation

Field emission-scanning electron microscopy (FE-SEM) images were recorded on a Zeiss Supra 55-VP. Tapping mode-atomic force microscopy (TM-AFM) images were recorded on a Veeco MultiMode AFM with a Nanoscope IIIa controller or a Veeco Enviroscope AFM with a Nanoscope IV controller.

2.5 Quinone ET kinetics

2.5.1 Compounds

All reagents (except 2-(*p*-tolysulfinyl)cyclohexane-2,5-diene-1,4-dione)) were purchased from Sigma-Aldrich and used without further purification. 2-(*p*-tolysulfinyl)cyclohexane-2,5-diene-1,4-dione) was synthesised in Departamento de Química Orgánica, Universidad Autónoma de Madrid, courtesy of Dr. Raúl Díaz. Analyte concentration for all experiments was 0.2 mM, unless stated to be 2 mM, in dry (using 3 Å molecular sieves) acetonitrile (MeCN) with 0.1 M tetrabuthylammonium hexafluorophosphate ($TBAPF_6$) as the supporting electrolyte. The molecular structures of the quinones under investigation are shown in Figure 2-10.

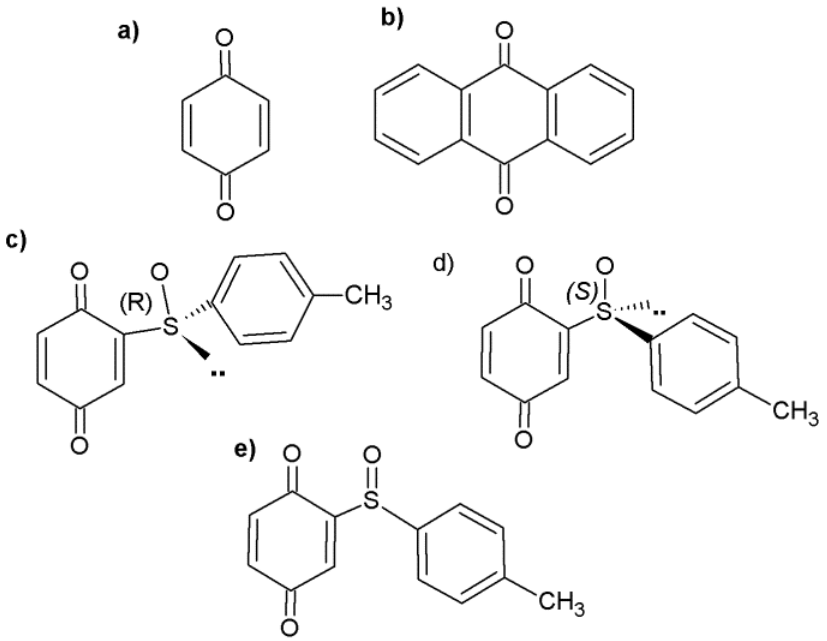

Figure 2-10. Molecular structures of *p*-benzoquinone (a), anthraquinone (b), enantiomer(-) (c), enantiomer(+) (d) and racemic mixture(+/-) (e).

Prior to experiments, solutions were purged with dry nitrogen gas for about 15 minutes, and during experiments gas was flowed over the surface of the solution in a home-built SECM cell (see Figure 2-11).

2.5.2 SECM of quinones

The scanning electrochemical microscopy (SECM) experiment was carried out under an atmosphere of dried nitrogen (N_2) gas, as shown in Figure 2-11. CVs were also carried out in this cell.

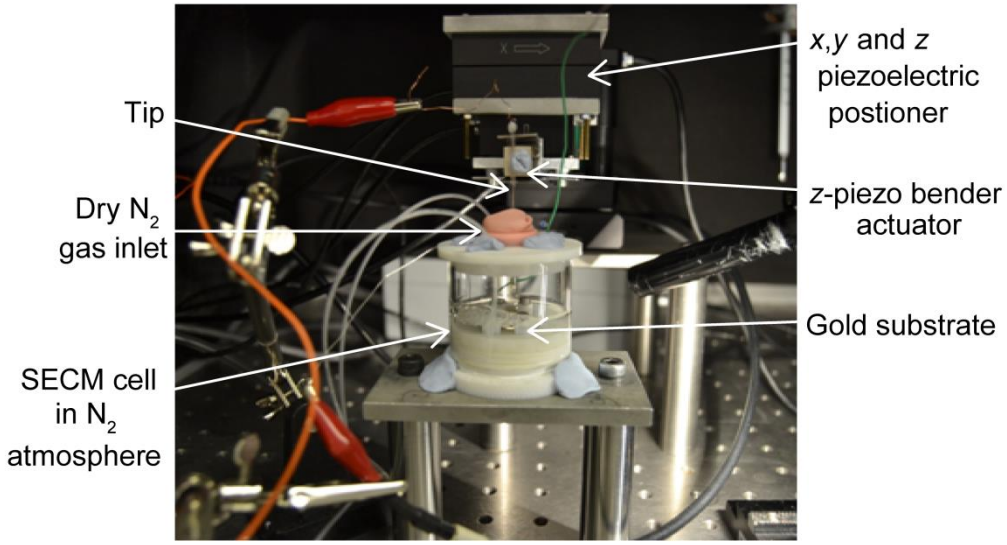

Figure 2-11. Basic components of a home-built SECM.

The home-built SECM instrument was mounted on a vibration-free optical table inside a Faraday cage. An UME tip was mounted in a tip holder on a piezo-bender actuator, which in turn was mounted to a 3D piezoelectric positioner controlled by a computer running custom LabVIEW code (LabVIEW 9.0, National instruments), which was also used for data acquisition. The potentials of the tip and/or the substrate *vs*. the silver-silver chloride (Ag/AgCl) reference electrode were applied through a home-built bipotentiostat and the tip current was measured. Experiments were performed by positive feedback mode.

Tip-substrate separation was controlled by monitoring changes in the oscillation amplitude which results from the IC of the tip with the substrate surface. As the tip encounters the surface, damping of oscillation amplitude occurs and tip approach toward the substrate is terminated.

2.5.3 CVs of quinones

CVs were performed at a potential scan rate of 25 mV s^{-1} in bulk solution (*i.e.* away from the underlying substrate) for each quinone on Au and CF UMEs, using 2 mM and 0.2 mM solutions. CVs were also performed in the feedback mode of SECM when the UME was very close (at intermittent contact) with the substrate, also at 25 mV s^{-1}, using 0.2 mM quinone concentration, whilst the underlying gold substrate was biased at 0.0 V.

Non-steady-state measurements were carried out in a two-electrode configuration using a potentiostat (CH Instruments model 760C, Austin, TX) at a scan rate of 1 V s^{-1}. This was for ferrocene (as a model reversible compound), *p*-BQ, AQ and the racemic compound, on Au and CF.

2.6 References

(1) Wightman, R. M.; Wipf, D. O. In *Electroanal. Chem.*; Bard, A. J., Ed.; Marcel Dekker: New York, 1989; Vol. 15, p 267.

(2) Zuliani, C.; Walsh, D. A.; Keyes, T. E.; Forster, R. J. *Anal. Chem.* **2010**, *82*, 7135.

(3) Ballesteros Katemann, B.; Schuhmann, W. *Electroanalysis* **2002**, *14*, 22.

(4) McKelvey, K.; Edwards, M. A.; Unwin, P. R. *Anal. Chem.* **2010**, *82*, 6334.

(5) Cornut, R.; Poirier, S.; Mauzeroll, J. *Anal. Chem.* **2012**, *84*, 3531.

(6) MacInnis, I. N.; Brantley, S. L. *Chem. Geol.* **1993**, *105*, 31.

(7) McGeouch, C.-A.; Edwards, M. A.; Mbogoro, M. M.; Parkinson, C.; Unwin, P. R. *Anal. Chem.* **2010**, *82*, 9322.

(8) Wipf, D. O.; Michael, A. C.; Wightman, R. M. *J. Electroanal. Chem.* **1989**, *269*, 15.

(9) McKelvey, K.; Snowden, M. E.; Peruffo, M.; Unwin, P. R. *Anal. Chem.* **2011**, *83*, 6447.

(10) Rudd, N. C.; Cannan, S.; Bitziou, E.; Ciani, I.; Whitworth, A. L.; Unwin, P. R. *Anal. Chem.* **2005**, *77*, 6205.

(11) Patel, A. N.; Collignon, M. G.; O'Connell, M. A.; Hung, W. O. Y.; McKelvey, K.; Macpherson, J. V.; Unwin, P. R. *J. Am. Chem. Soc.* **2012**, *134*, 20117.

(12) Patel, A. N.; Tan, S.-y.; Unwin, P. R. *Chem. Commun.* **2013**, *49*, 8776.

(13) Kleijn, S. E. F.; Lai, S. C. S.; Miller, T. S.; Yanson, A. I.; Koper, M. T. M.; Unwin, P. R. *J. Am. Chem. Soc.* **2012**, *134*, 18558.

(14) Snowden, M. E.; Güell, A. G.; Lai, S. C. S.; McKelvey, K.; Ebejer, N.; O'Connell, M. A.; Colburn, A. W.; Unwin, P. R. *Anal. Chem.* **2012**, *84*, 2483.

(15) Lai, S. C. S.; Patel, A. N.; McKelvey, K.; Unwin, P. R. *Angew. Chem., Int. Ed.* **2012**, *51*, 5405.

(16) Patel, A. N.; McKelvey, K.; Unwin, P. R. *J. Am. Chem. Soc.* **2012**, *134*, 20246.

(17) Güell, A. G.; Ebejer, N.; Snowden, M. E.; McKelvey, K.; Macpherson, J. V.; Unwin, P. R. *Proc. Natl. Acad. Sci. U. S. A.* **2012**, *109*, 11487.

3 Hopping Intermittent Contact-Scanning Electrochemical Microscopy (HIC-SECM): Visualising Interfacial Reactions and Fluxes from Surfaces to Bulk Solution

Hopping intermittent contact-scanning electrochemical microscopy (HIC-SECM) is introduced as a powerful new technique for the quantitative visualisation of redox activity and concentration at and above a surface of interest. HIC-SECM combines a hopping imaging mode, in which data are acquired at a tip as a function of distance (*z*) from the surface, at a series of *x*, *y* pixels across the surface, using the principles of intermittent contact (IC) to provide a non-electrochemical means of determining when the tip and the substrate come into contact. The implementation of HIC-SECM is described, and SECM feedback measurements in 3D space over a gold band array are presented. To demonstrate the generality of the methodology, flux imaging is also carried out over a Pt-disk ultramicroelectrode (UME) in the feedback mode and substrate generation/tip collection mode. The type of information that can be extracted from the data sets acquired include *x*-*y* current maps, at a well-defined tip-substrate separation (parallel to the surface), *x*-*z* current maps (normal to the surface), 3D *x*-*y*-*z* profiles, approach curves at particular spots on the surface of interest, and surface topography. Moreover, because HIC-SECM utilises an oscillating probe, alternating current data are also obtained, that greatly enhances the information content compared to other types of electrochemical imaging. Furthermore, interfacial fluxes are ubiquitous in chemistry, and allied areas, and

HIC-SECM opens up the possibility of detailed flux visualisation in three dimensions for many physicochemical processes.

3.1 Introduction

Scanning electrochemical microscopy (SECM) uses an ultramicroelectrode (UME) scanned laterally close to a surface or interface of interest, to build up a quantitative image of the electrochemical or chemical activity.[1,2] In its simplest form, and in most reported applications, the UME is scanned at a constant-height, in a fixed plane. However, this may complicate quantitative analysis, due to the convolution of topography (tip-substrate distance) and substrate activity in the tip electrode response.[3,4] Furthermore, with this approach, any significant topographical features in the surface may result in tip-crash, particularly with small tips that have to be positioned close to the surface. Moreover, probes operated in potentiometric mode have no reliable means of tip-substrate distance (*d*) control, making them especially challenging to use routinely.[5,6]

A wealth of alternative imaging modes and techniques, such as SECM-atomic force microscopy (AFM),[7,8] SECM-scanning ion conductance microscopy (SICM),[9,10] shearforce-SECM,[11,12] the use of impedance in alternating current (AC)-SECM,[13,14] and strict temperature control (through the use of an isothermal chamber),[15] have been developed as a means of achieving reliable tip-substrate distance control. In the best cases, these techniques allow a small separation to be maintained between the tip and sample, to achieve the greatest spatial resolution. Most importantly, most of these approaches allow topography and activity of the sample to be separated effectively. On the other hand, many of these methods have not yet been widely adopted which may be attributed, at least in part, to the need for specialized tips and/or additional equipment for implementation.

While there is an ample body of work on the use of conventional SECM techniques to provide two-dimensional (2D) maps, less attention has been given to mapping three-dimensional (3D) profiles and fluxes above surfaces and interfaces. As an aside, it is noted that an elementary approach to 3D mapping is to perform 2D scans, such as that that shown in Figure 2-5(a), at a series of heights from a sample surface, as originally proposed by Kwak and Bard.[16] However, without positional feedback this still leads to some of the problems highlighted above. Mapping of 3D profiles can be better achieved by a so-called hopping imaging mode,[17,18] involving a series of successive approaches of the tip electrode normal to the surface at a sequence of points. This hopping scanning mode, shown in Figure 2-5(b), requires tip-substrate distance determination in order to stop the advancement of the tip for each approach. By taking measurements during the approach curve, at various distances away from the surface, full concentration (and flux) profiles can be mapped.

Hopping modes have been used in both SICM[19] and SECM[20] for purely topographical imaging. In the SICM literature, this type of imaging has been called floating backstep,[21,22] hopping,[17] and standing approach.[23] These methods were developed specifically for samples with large topographical variation, so as to avoid tip-crash that might occur during lateral probe motion imaging. Various hopping modes have been implemented in SECM to obtain local flux information,[20,24-27] with the technique usually used to acquire data only at the distance of closest approach,[20,27] but sometimes during the whole approach curve.[25] In hopping modes that employ a tapping mode-like scanning method, such as SECM/optical microscopy (OM) in constant-distance mode with shearforce feedback,[27] the retract distance is too small to obtain useful data above the surface. The wealth of information that can be obtained by recording data during the approach is evident in

4D shearforce imaging,[25] where 3D current profiles are obtained. The terminology (4D) refers to a data set consisting of *x*, *y* and *z*-position, and tip current. However, shearforce SECM requires the use of specialized probes; namely highly flexible glass-coated microelectrodes that may place some restrictions on the type of measurements that can be made.

In intermittent contact (IC)-SECM, the tip is oscillated normal to the surface of interest and the oscillation amplitude can be used to control the tip-substrate separation, since upon physical intermittent contact between the tip and substrate, the oscillation amplitude is damped.[28-30] This damping is used as a set point for imaging in IC-SECM, and, as shown herein, can also be used as a set point to terminate each approach curve in hopping (H)IC-SECM.

A key attribute of IC-SECM is that because the tip is oscillated, an alternating current (AC) component develops that can provide additional information about the surface, as first described in tip-position modulation (TPM) SECM.[31,32] This is made use of in HIC-SECM, which acquires 3D spatial data sets (*x*, *y*, *z*) of the DC tip current, AC tip current magnitude and phase, probe oscillation amplitude and topographical data. All of these complementary data are collected simultaneously at a particular point in space. Given the large dataset acquired during a typical HIC-SECM scan, hundreds of possible plots can be constructed. In addition, the *z*-position of the tip at IC provides topographical information.

To illustrate the general features of HIC-SECM, a gold band array on glass was imaged as a model substrate, in the well-known SECM feedback mode.[33] Further imaging of a Pt-disk UME was performed in the feedback mode,[33,34] and also the

substrate generation/tip collection (SG/TC) mode[35] to highlight the versatility of the technique.

3.2 Localised proton-promoted etching of calcite via SECM

3.2.1 Introduction to calcite dissolution

The dissolution of calcite (calcium carbonate, $CaCO_3$) is of interest in areas such as scaling on metal pipes,[36] neutralisation of acidic lakes[37-39] and weathering of carbonate rocks.[40] The rate of reaction increases with decreasing pH (proton concentration),[41-43] and below pH 4 the mechanism is dominated by proton attack.[36] The proton-promoted dissolution reaction involves the following major processes:[37]

$$CaCO_{3(s)} + H^+_{(aq)} \rightleftharpoons Ca^{2+}_{(aq)} + HCO^-_{3(aq)} \quad (3.1)$$

$$HCO^-_{3(aq)} + H^+_{(aq)} \rightleftharpoons H_2CO_{3(aq)} \rightarrow CO_{2(aq)} + H_2O_{(l)} \quad (3.2)$$

In proton-promoted dissolution of calcite, etch pits form at dislocations,[37] although the rate of dissolution is difficult to measure since macroscopic measurements will average the rate of dissolution over the whole surface. This work builds on previous studies which have demonstrated SECM to be powerful for local etching studies of a wide variety of different materials.

The use of IC-SECM to define a tip-substrate distance by non-electrochemical means has been demonstrated at a calcite crystal surface, to probe the calcite $(10\bar{1}4)$ cleavage surface (from natural 'Iceland Spar') at the microscopic scale. In this work, the size of the probe is much less than the characteristic dislocation spacing (as

revealed by etching experiments). This allowed etch pits to be formed on regions of the calcite surface which are free from dislocations.

To clearly reveal the locations of measurements, studies focused on cleaved 'mirror' surfaces, where one of the two faces produced by cleavage was etched freely to reveal defects intersecting the surface, while the other (mirror) face was etched locally (and quantitatively) using SECM to generate high proton fluxes with a 25 μm diameter Pt disk ultramicroelectrode (UME) positioned at a defined (known) distance from a crystal surface. The etch pits formed at various etch times were measured using white light interferometry to ascertain pit dimensions.

3.2.2 Etch pit formation using IC-SECM

See Figure 3-1 for a typical IC-SECM approach curve. This is not an approach curve for diffusion-limited oxygen reduction (hindered diffusion response), as was used in a previous similar study,[44,45] because this current was unstable and could induce unwanted electrochemical reactions close to the calcite surface. Instead of the tip current on the *y*-axis, the oscillation amplitude of the tip is plotted, as a function of tip-substrate separation.

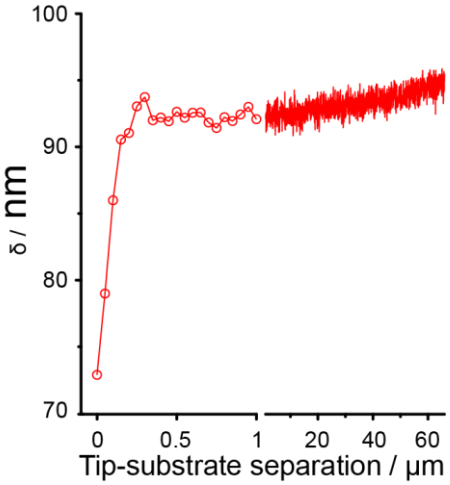

Figure 3-1. IC-SECM curve of piezo oscillation for 12.5 μm radius Pt disk electrode oscillated at 80 Hz, δ = 94 nm, in 0.1 M KNO_3, approaching a calcite surface. Note the different length scales on the *x*-axis.

Away from the surface, the oscillation of the tip is *ca*. 94 nm, and this does not change with tip-substrate distance, until the glass sheath of the tip makes physical IC with the substrate, at which point the oscillation amplitude is damped. This damping is used as a feedback mechanism for constant-distance imaging, or in this case, to accurately position the tip at a known distance from the crystal surface. After IC was confirmed, by a decrease of 5 % in the oscillation amplitude for three consecutive measurements, the tip was withdrawn 10 μm to perform the localised dissolution on the crystal surface. The point in Figure 3-1 at which the tip-substrate separation = 0 μm was the final point in the approach curve.

Figure 3-2 shows a typical example of two cleaved and etched matched surfaces of a calcite crystal: (a) is the SECM-etched surface showing two dominant SECM pits (100 nA for 300 s) along with background pits and (b) is the corresponding free-etched surface on which small pits (4 – 8 μm^2 and surface coverage $\approx 10^4$ cm^{-2}) are formed. These background pits coincide on the two images and mark screw and edge

dislocations,[37,46-48] emergent at the calcite surface. Also evident on both images are very small pits in the background which are formed at point defects.[37,46-49] This free etching is due to the bulk dissolution over the entire crystal surface. It is evident that the amount of free etching is negligible compared to the proton-promoted dissolution, *i.e.* dissolution occurring directly below the UME, in (a). Evidently, Figure 3-2 shows that most SECM measurements will, in fact, be made in regions free from the influence of screw and edge dislocations, presenting a clear opportunity to study dissolution in dislocation-free areas, *i.e.* to elucidate dissolution only in areas with point defects.

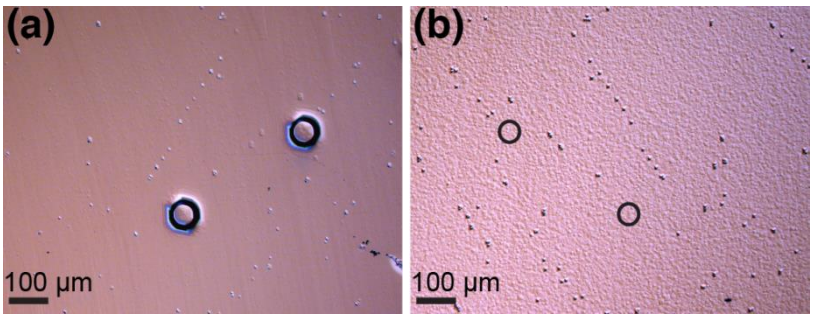

Figure 3-2. DIC micrographs showing: (a) two SECM-induced etch pits on calcite obtained using 100 nA current for 300 s; and (b) the corresponding free-etched mirror face. Circles on the free etched mirror half correspond to the surface locations of the SECM etch pits in (a).

Figure 3-3 illustrates the effect of etch time, showing a typical WLI micrograph (a) and the corresponding pit cross sections (b), after etching times of 120, 180, 240 and 300 seconds. It is evident that the pit depth is linear with time over this range and the proton-promoted SECM-induced pits are the only significant features on the surface. This provides evidence for considering SECM-induced dissolution as the main process on an otherwise relatively inert surface.

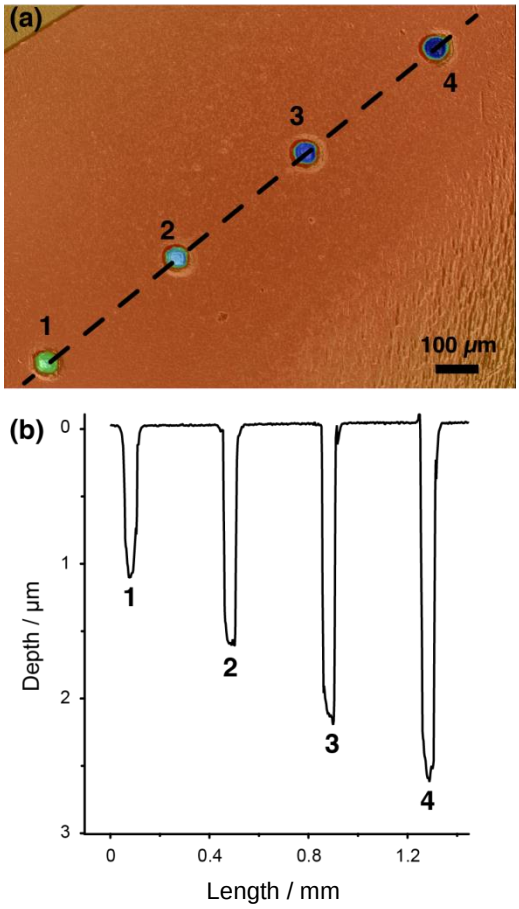

Figure 3-3. (a) WLI image of a set of SECM-induced etch pits at times of 120 s (1), 180 s (2), 240 s (3) and 300 s (4) etched at 100 nA. (b) Cross-section of etch pits taken from WLI image (black dashed line).

3.3 Gold band array on glass

Gold bands (unbiased) were imaged as a model substrate with the tip operated in feedback mode; typical HIC-SECM data are presented in Figure 3-4. All plots in this Figure were obtained from a single scan, and this highlights the amount of data that can be obtained concurrently. Three different ways of visualising the electrochemical activity maps for the oxidation of $FcTMA^{+}$ to $FcTMA^{2+}$ at the tip, as measured by the DC tip current (i_{mean}), are shown in Figure 3-4(a-c); *x*-*y*-*z*, *x*-*y* and *x*-*z* maps, respectively. The gold bands are well-defined, as visualised by the tip current at the

surface in Figure 3-4(b), with the lowest normalized limiting current at 0.11 times the bulk current over glass and up to 4 times the bulk over gold. Based on the negative feedback current, this corresponds to an effective electrode-substrate separation of *ca.* 190 nm.[50]

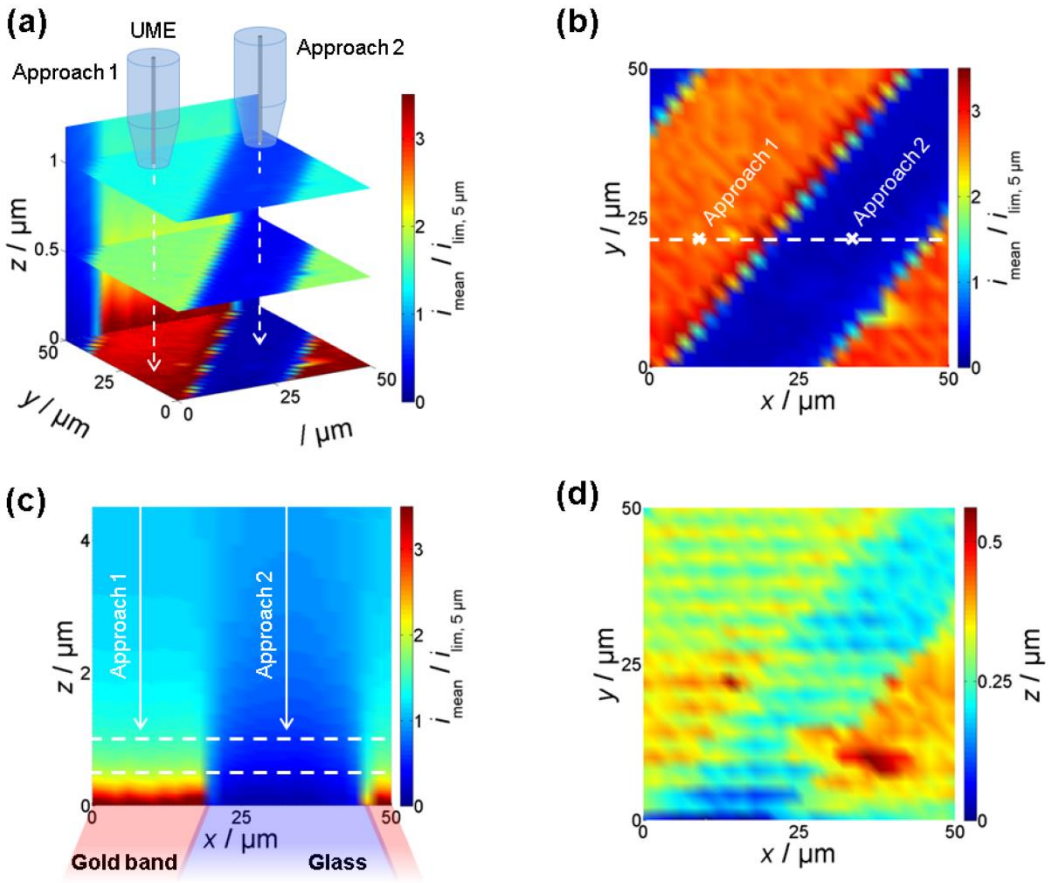

Figure 3-4. A HIC-SECM data set, acquired by imaging gold bands on glass in the feedback mode. The tip current measured was normalized by a value close to 'bulk' at 5 μm, at each *x*,*y* pixel, and is presented as: (a) an *x*-*y*-*z* 3D current image with data taken at 0.0 μm, 0.5 μm and 1.0 μm from the surface, *i.e.* at the final point of each approach and at the two dashed white lines in (c); (b) an *x*-*y* image at intermittent contact; and (c) an *x*-*z* current profile at y = 20.0 μm, shown by the dashed white line in (b). Plane-fitted surface topography (d), using the final *z*-position of each tip (HIC) approach. The imaging tip was a 2 μm diameter Pt-disk UME (*RG* =10), and imaging was performed in 1 mM $FcTMA^+$ (0.1 M KCl) aerated solution. Approach curves were performed every 2 μm in *x* and *y*, using a constant retract height of 5 μm (see Section 2.3.5)

Perhaps the most powerful demonstrations of HIC-SECM as a technique for flux and activity visualisation around a surface are the 2D vertical slice image in Figure 3-4(c) and the 3D image in Figure 3-4(a). The 2D vertical slice is one of 26 along the *y*-direction that can be obtained from this particular data set, while the three planes shown in the 3D image have been extracted from 100 recorded approach steps (and corresponding 2D images). This level of information is akin to 3D *z*-stacks obtained in confocal laser scanning microscopy, for example as applied to electrochemical systems,[51] but with better *z*-resolution. Redox activity can be mapped not only at the surface, but at very well defined distances (in 50 nm increments here) from the surface due to the principles of IC, with visualisation of the full current profile in 3D space around the substrate.

HIC-SECM also provides topographical information and the plane-fitted topography from the *z*-piezo position is shown in Figure 3-4(d). Although the 1 μm radius imaging probe had a glass sheath of radius 10 μm, the glass tip is still able to provide a reasonable level of topographical information on the sample.

When the tip is more than 4.5 μm from the surface, the positive or negative feedback effects of the surface are much reduced, and so a current measurement close to the bulk value can be made at the start of each approach, approximately 5 μm away from the surface. From theory, at 5.0 μm from the surface the normalized tip current would be well within 90 % - 110 % of the bulk value for the extremes of negative feedback and positive feedback.[16,52,53] As such, 5.0 μm was deemed to be a reasonable distance over which to perform hopping, being sufficiently close to the electrode to perform fast scans, whilst far enough away that the ‘bulk’ current measurement was reasonably unaffected by the surface. To enable quantitative analysis of individual approach curves Figure 3-5, the normalized current for

approach 1 (over gold) was multiplied by 1.089 (the normalized current at 5 μm for positive feedback)[52] and the normalized current for approach 2 (over glass) was multiplied by 0.940 (the normalized current at 5 μm for negative feedback),[53] so that it could be plotted with respect to theory. The validity of this analysis was verified by measuring the steady-state current at larger distances from the surface. This analysis was used here since the approach was only 5 μm, however a true bulk value would be identical regardless of the conductive nature of the underlying substrate. Note that such 'bulk' measurements could easily be incorporated into the scan, either at a few pixels or throughout the scan, for example by introducing non-linear data acquisition during an approach (fewer points further away).

As can be seen in Figure 3-5, each approach curve is in good agreement with theory. It is a key feature of HIC-SECM that one can readily pull out approach curves for any *x*-*y* pixel.

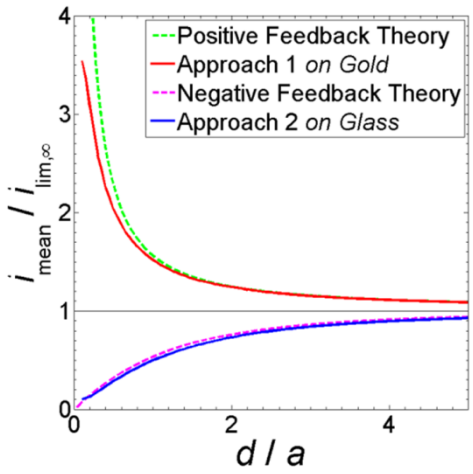

Figure 3-5. Approach curve data for approach 1 and approach 2, shown in Figure 3-4(b) and (c). Experimental approach curves over gold (approach curve 1, red) and over glass (approach curve 2, blue) are compared to theoretical approach curves for an electrode of *RG* value 10 for pure negative feedback (dashed magenta)[53] and positive feedback (dashed green).[52]

As is well known in SECM, and as discussed in earlier work on IC-SECM,[28] the UME face and substrate surface are never exactly parallel and the edge of the glass surround of the UME comes into contact at the point of IC.[27] The current at this position can be analysed to determine the distance between the active part of the tip (electrode) and substrate. To fit the data, a value of 200 nm was determined as the distance between the electrode and substrate at IC.

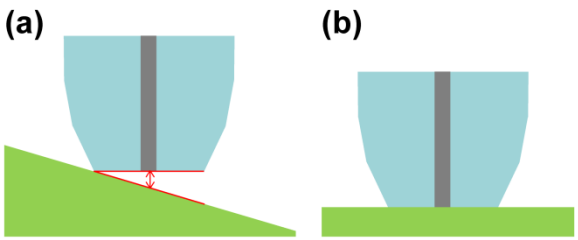

Figure 3-6. Schematic showing the distance of closest approach for a misaligned substrate (a) and a perfectly aligned tip and substrate (b).

3.4 Pt-disk electrode

An inverted Pt-disk UME was used as a second model substrate. The tip electrode used to image the substrate is shown in Figure 3-7(a(i)). Note the geometry of the electrode is oval, as is common for tip electrodes of this size. An optical image of the substrate electrode is shown in Figure 3-7(a(ii)). This substrate was imaged using HIC-SECM in both the feedback mode and in SG/TC mode. The tip-substrate setup is shown in Figure 3-7(b), while the feedback mode and SG/TC mode used for electrochemical imaging are described in Figure 3-7(c) and (d), respectively.

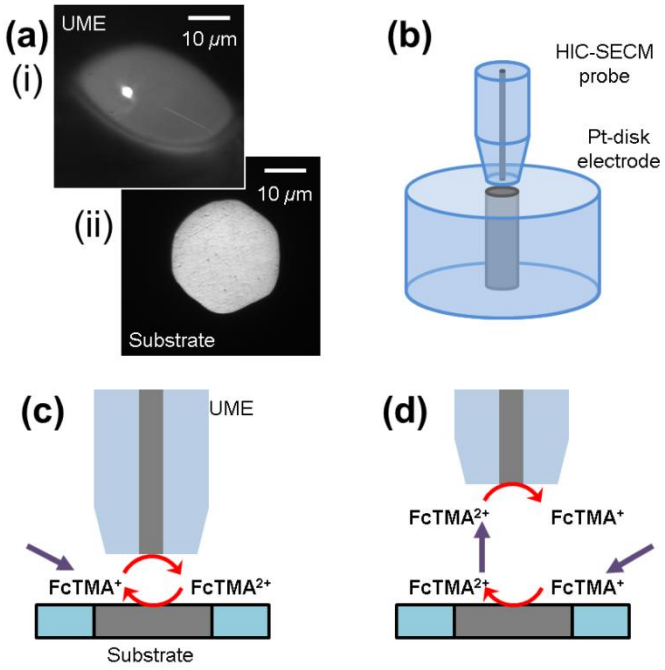

Figure 3-7. Optical microscope image of the 2 μm diameter Pt-disk UME tip used for imaging (a(i)), and the 25 μm diameter Pt-disk substrate UME (a(ii)). Experimental setup of 2 μm diameter probe UME over inverted 25 μm diameter substrate UME (b). Electrochemical reactions for measurements in the feedback mode (c) and SG/TC mode (d).

Firstly, feedback measurements are discussed. The tip current at the end of each approach curve (where HIC was detected) is shown in Figure 3-8(a), and an *x*-*z* profile extending 10 μm above the surface at the location of the dashed white line is shown in Figure 3-8(b). As for the imaging of the band electrodes, the mean tip current has been normalized by the value at the furthest distance in the hopping approach, in this case at 10.5 μm from the surface.

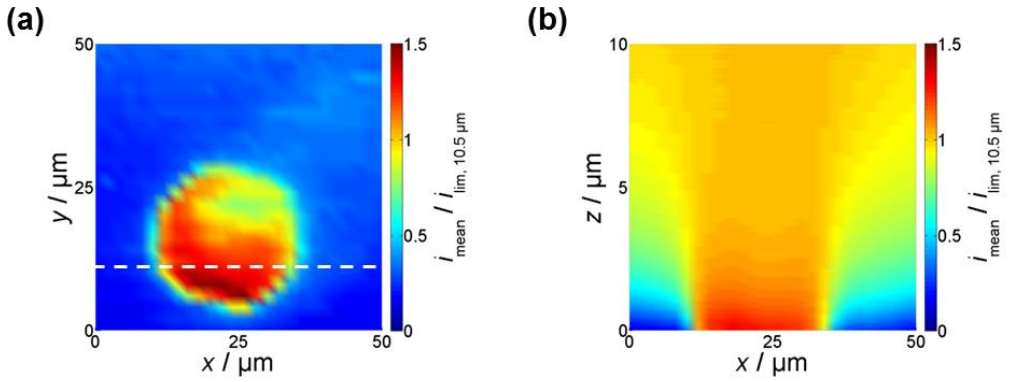

Figure 3-8. HIC-SECM images showing the tip current at the position of intermittent contact in the feedback mode (a) and an *x*-*z* profile of the tip current at *y* = 8 μm (b).

Although the increased current near the substrate electrode is as expected, due to positive feedback, there is some heterogeneity in the Pt surface activity (Figure 3-8(a)), which is magnified due to the close distance between the electrode and the substrate, estimated to be *ca.* 100 nm based on the current values attained (in negative feedback) over the regions of the glass substrate. The apparent heterogeneity is most likely due to surface contamination, since no special efforts were made to remove all of the material after the polishing procedure. The *x*-*z* profile (Figure 3-8(b)) shows strong positive feedback over the disk substrate (*ca.* $z = 0$ μm) which diminishes as the tip-substrate distance increases. Away from the disk ($x = 0$

μm or 50 μm), the behaviour is that for hindered diffusion (negative feedback). Between these two limits, there is an interesting section, notably in the region of the insulator close to the edge of the disc where the tip sees mainly negative feedback at moderate distances from the surface, but close to the surface is influenced by the electrode edge, leading to an enhancement in the current.

The inverted Pt-disk electrode was also imaged in SG/TC mode. The substrate was held at 0.45 V, to cause the oxidation of $FcTMA^+$ to $FcTMA^{2+}$ at a diffusion-limited rate, while the tip was held at 0 V for the reduction of $FcTMA^{2+}$ to $FcTMA^+$. Typical tip collection current maps are shown in Figure 3-9 in the form of an *x*-*y*-*z* plot (a), an *x*-*y* plot (b) and an *x*-*z* current map (c). The data, which highlight the detailed information available, are presented as absolute current values as the tip collected a reaction product that may not be present in bulk solution.

These data are valuable in revealing clear differences between the feedback and SG/TC *x*-*z* profiles for the Pt-disk, in Figure 3-8(b) and Figure 3-9(c), as a consequence of the different fundamental principles of operation. In the SG/TC mode, the tip acts as a reasonably passive probe of the concentration profile generated at the substrate, which extends over large distances (beyond that of the image) except when the tip and active part of the substrate are close, when the tip experiences positive redox feedback. In contrast, the tip needs to get much closer to the substrate to determine the redox activity in the feedback mode.

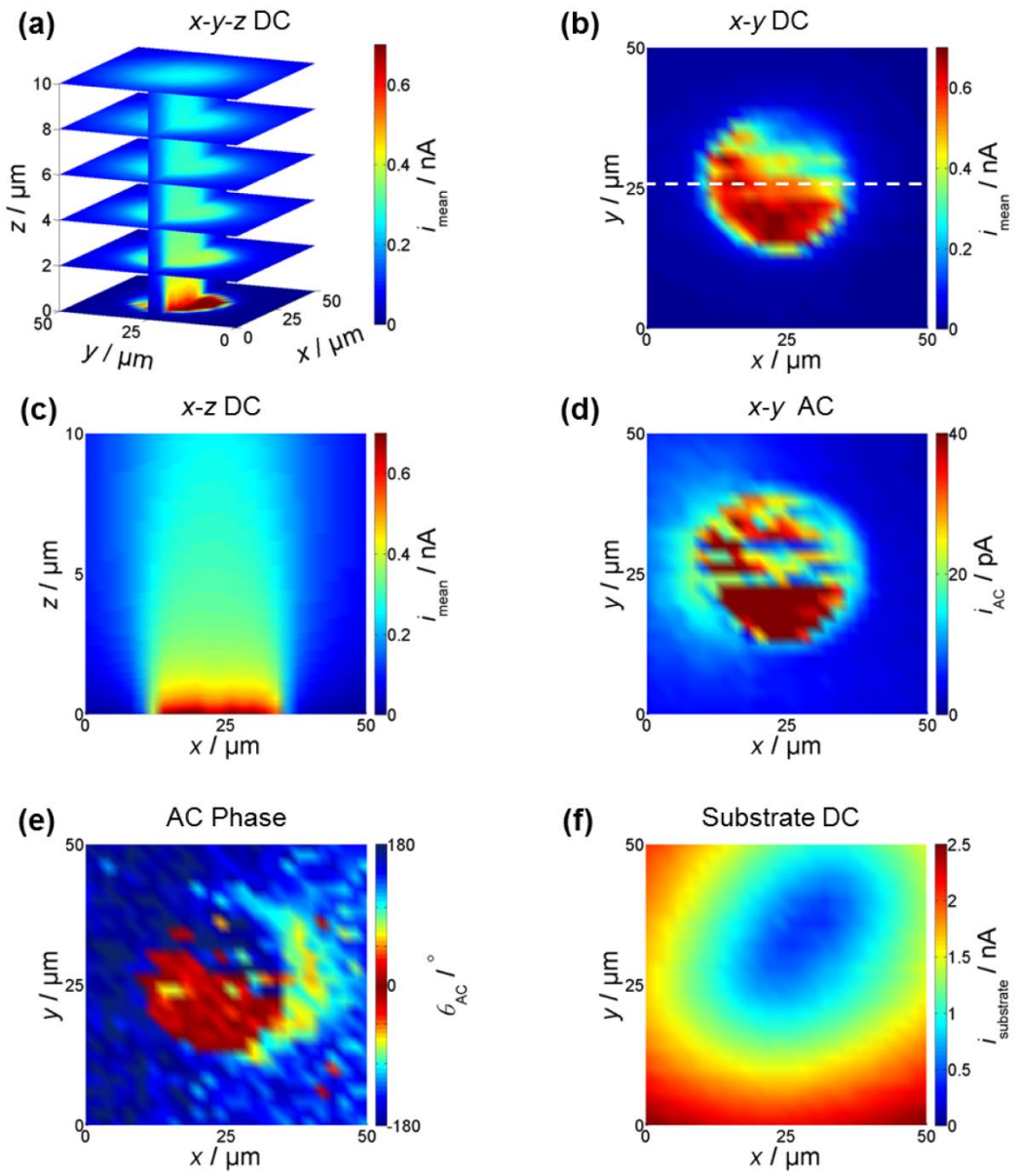

Figure 3-9. A HIC-SECM data set, acquired by imaging the surface of a 25 μm diameter Pt-disk UME in the SG/TC mode. The tip current is presented as: (a) an *x-y-z* 3D current image with x-y maps displayed at 0.0 μm, 2.0 μm, 4.0 μm, 6.0 μm, 8.0 μm and 10.0 μm from the surface, and an *x-z* map at y = 26.0 μm; (b) an *x-y* image at intermittent contact; and (c) an *x-z* current profile at y = 26.0 μm, shown by the dashed white line in (b). Simultaneously acquired data are presented at the surface (at intermittent contact) for the AC magnitude at the tip (d), the AC phase difference, θ_{AC}, at the tip (e) and the current at the substrate as a function of tip position (f).

A further advantage of the use of HIC-SECM, with an oscillated probe, is that additional data are available that are not attainable from alternative multidimensional electrochemical imaging techniques.[25] Figure 3-9(d) shows the AC magnitude at IC, for the plane analogous to Figure 3-9(b). As established in the previous work on IC-SECM,[28,29] and TPM,[31,32] the AC signal has a larger dynamic range and can reveal more detail than the DC image. The AC phase, θ_{AC}, presented in Figure 3-9(e), shows that the AC is out of phase with respect to the tip-substrate separation over the insulator and in phase with respect to the tip-substrate separation over the conductor, as expected based on TPM studies.[32] Again, this image highlights that one obtains additional contrast through the availability of the AC signal.

For these studies, the substrate current was also recorded during the entire HIC-SECM imaging process. The substrate current corresponding to the *x-y* maps in Figure 3-9(b) and Figure 3-9(d) is shown in Figure 3-9(f). Note that when the tip is exceptionally close to the substrate, its main impact is to block diffusion to the substrate, so that the substrate current is affected by the moving tip, mirroring the geometry of the oval glass surrounding shown in Figure 3-7(a(i)). Similar tip effects have been observed and fully explained in the context of AFM imaging of active UME substrates.[54]

It is informative to analyse the distance dependence of the AC magnitude, probe oscillation amplitude and AC phase difference as a function of tip-substrate separation. Typical data over the conducting and insulating part of the disk substrate are presented in Figure 3-10(a(i-iii)), respectively, for the feedback image in Figure 3-8 and in Figure 3-10(b(i-iii)), respectively, for the SG/TC image in Figure 3-9.

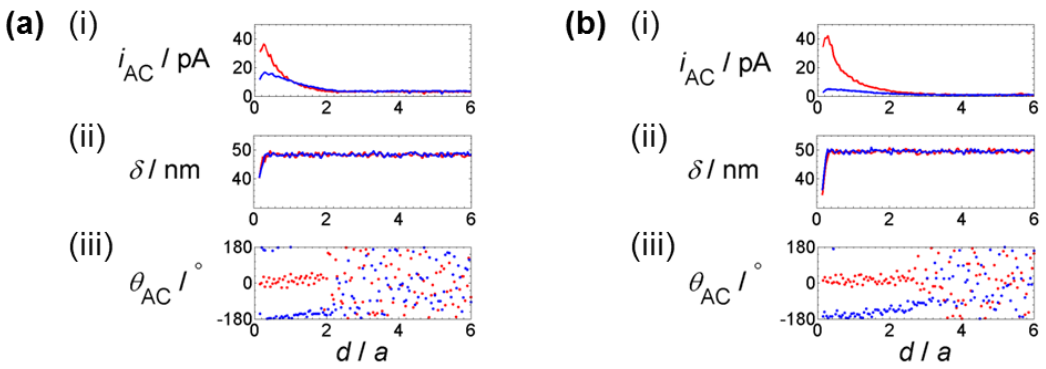

Figure 3-10. The AC component of the current (i), the tip oscillation amplitude, δ (ii) and the AC phase difference (iii) are shown for HIC approach curves over glass (blue) and Pt (red) in feedback mode (a) (data from Figure 3-8) and SG/TC mode (d) (data from Figure 3-9).

AC magnitude approach curves reveal a significant increase in current close the platinum substrate, shown in Figure 3-10(a(i)) and Figure 3-10(b(i)), consistent with expectations based on earlier TPM[31,32] or IC-SECM studies.[28,29] In brief, the AC approach to a conductive substrate is reasonably well-modelled as the derivative of the positive feedback approach curve.[31,32] The AC amplitude to an insulating surface similarly increases, although the increase is not as steep.[31] In the SG/TC mode, the concentration profile far from the surface is characterized by a shallow gradient (Figure 3-9(c) and consequentially the change in the AC current magnitude in the approach curve is weaker (Figure 3-10(b(i))).

The oscillation amplitude, δ, used to detect IC (Figure 3-10(a(ii)) and Figure 3-10(b(ii))) provides a clear signal by which to sense the surface. The IC signal, used for positional feedback, was found to be reliable and consistent over the whole scan area, as shown, for example in Figure 3-11, for the image of gold bands shown in Figure 3-4. This forms the basis for the quantitative analysis presented herein: IC

provides reliable tip-substrate distance control for HIC-SECM, allowing SECM images to be reconstructed at well-defined, user-selectable, heights from the surface.

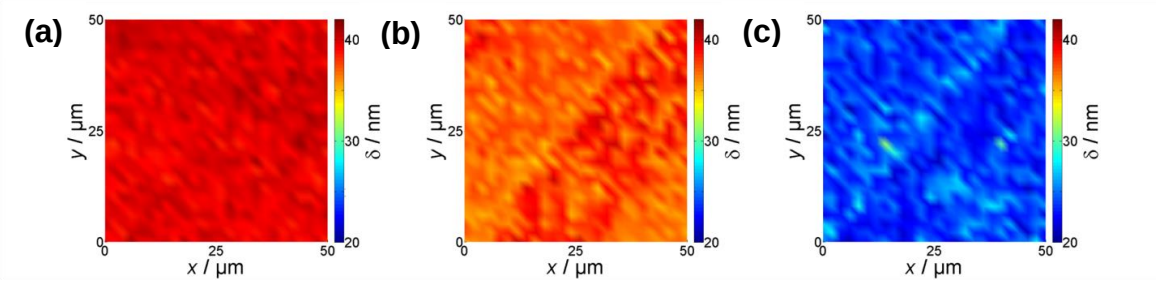

Figure 3-11. Measured oscillation amplitude, δ, as a function of x-y position, collected in the HIC-SECM scan of gold bands on glass, as presented in Figure 3-4. Maps are shown for the 'bulk' (1000 nm from the surface) (a), at the setpoint (10 % damping of bulk amplitude) for IC detection (b), and after three 50 nm steps (at the surface) (c).

The AC phase difference is also consistent with expectations based on earlier work.[31,32] Figure 3-10(a(iii)) and Figure 3-10(b(iii)) indicate that the AC signal is in phase with the tip-substrate separation over platinum, at the surface, in both feedback and SG/TC modes. The AC signal is out of phase over the inert surface, reflecting the different mode of mass transport (hindered diffusion).[31,32] Away from the surface, the phase difference oscillates randomly and is not diagnostic.

3.5 Conclusions

HIC-SECM has been demonstrated as a novel and effective imaging technique that enables multidimensional (3D spatial) mapping with various DC and AC signals acquired, coupled with an effective non-electrochemical method for distance control. HIC-SECM involves a series of hopping (*z*) approach curves at each point in an *x*-*y* map, using IC for positional feedback to sense the surface and halt the tip approach. Although HIC-SECM has been illustrated with respect to measurements at electrochemical interfaces, it is expected that the technique will be useful for visualising the chemical flux around many types of interface.[20,51]

Since a physical interaction between tip and substrate is used for tip position control, a particularly attractive aspect of HIC-SECM is that any type of probe should be able to be usable, including potentiometric probes, which have proved rather difficult to deploy in conventional SECM compared to amperometric tips. It is also important to point out that, as with IC-SECM and TPM, an AC signal is obtained as well as DC data which, in principle, provides a great depth of information about interfaces and interfacial processes, as highlighted herein.

Using HIC-SECM, as opposed to IC-SECM, means that the tip is only in contact with the surface for short periods, and so the tip and the sample are more protected. Furthermore, since a (close to) bulk measurement is made at each *x*-*y* position in a scan, correction can be made for changes in bulk solution concentration or changes in the electrode, for example, due to fouling. In this respect, HIC-SECM greatly expands the range and capability of 'self-referencing' probe electrode techniques.

3.6 References

(1) Amemiya, S.; Bard, A. J.; Fan, F.-R. F.; Mirkin, M. V.; Unwin, P. R. *Annu. Rev. Anal. Chem.* **2008**, *1*, 95.

(2) Sun, P.; Laforge, F. O.; Mirkin, M. V. *Phys. Chem. Chem. Phys.* **2007**, *9*, 802.

(3) Zhao, X.; Diakowski, P. M.; Ding, Z. *Anal. Chem.* **2010**, *82*, 8371.

(4) James, P. I.; Garfias-Mesias, L. F.; Moyer, P. J.; Smyrl, W. H. *J. Electrochem. Soc.* **1998**, *145*, L64.

(5) Horrocks, B. R.; Mirkin, M. V.; Pierce, D. T.; Bard, A. J.; Nagy, G.; Toth, K. *Anal. Chem.* **1993**, *65*, 1213.

(6) Wei, C.; Bard, A. J.; Nagy, G.; Toth, K. *Anal. Chem.* **1995**, *67*, 1346.

(7) Macpherson, J. V.; Unwin, P. R. *Anal. Chem.* **2000**, *72*, 276.

(8) Kranz, C.; Friedbacher, G.; Mizaikoff, B.; Lugstein, A.; Smoliner, J.; Bertagnolli, E. *Anal. Chem.* **2001**, *73*, 2491.

(9) Comstock, D. J.; Elam, J. W.; Pellin, M. J.; Hersam, M. C. *Anal. Chem.* **2010**, *82*, 1270.

(10) Takahashi, Y.; Shevchuk, A. I.; Novak, P.; Murakami, Y.; Shiku, H.; Korchev, Y. E.; Matsue, T. *J. Am. Chem. Soc.* **2010**, *132*, 10118.

(11) Ludwig, M.; Kranz, C.; Schuhmann, W.; Gaub, H. E. *Rev. Sci. Instrum.* **1995**, *66*, 2857.

(12) Ballesteros Katemann, B.; Schulte, A.; Schuhmann, W. *Chem. - Eur. J.* **2003**, *9*, 2025.

(13) Alpuche-Aviles, M. A.; Wipf, D. O. *Anal. Chem.* **2001**, *73*, 4873.

(14) Kurulugama, R. T.; Wipf, D. O.; Takacs, S. A.; Pongmayteegul, S.; Garris, P. A.; Baur, J. E. *Anal. Chem.* **2005**, *77*, 1111.

(15) Kim, J.; Shen, M.; Nioradze, N.; Amemiya, S. *Anal. Chem.* **2012**, *84*, 3489.

(16) Kwak, J.; Bard, A. J. *Anal. Chem.* **1989**, *61*, 1794.

(17) Novak, P.; Li, C.; Shevchuk, A. I.; Stepanyan, R.; Caldwell, M.; Hughes, S.; Smart, T. G.; Gorelik, J.; Ostanin, V. P.; Lab, M. J.; Moss, G. W. J.; Frolenkov, G. I.; Klenerman, D.; Korchev, Y. E. *Nat. Methods* **2009**, *6*, 279.

(18) Borgwarth, K.; Ebling, D. G.; Heinze, J. *Ber. Bunsen-Ges.* **1994**, *98*, 1317.

(19) Chen, C.-C.; Zhou, Y.; Baker, L. A. *Annu. Rev. Anal. Chem.* **2012**, *5*, 207.

(20) Takahashi, Y.; Shevchuk, A. I.; Novak, P.; Babakinejad, B.; Macpherson, J.; Unwin, P. R.; Shiku, H.; Gorelik, J.; Klenerman, D.; Korchev, Y. E.; Matsue, T. *Proc. Natl. Acad. Sci. U. S. A.* **2012**, *109*, 11540.

(21) Mann, S. A.; Hoffmann, G.; Hengstenberg, A.; Schuhmann, W.; Dietzel, I. D. *J. Neurosci. Methods* **2002**, *116*, 113.

(22) Happel, P.; Hoffmann, G.; Mann, S. A.; Dietzel, I. D. *J. Microsc.* **2003**, *212*, 144.

(23) Takahashi, Y.; Murakami, Y.; Nagamine, K.; Shiku, H.; Aoyagi, S.; Yasukawa, T.; Kanzaki, M.; Matsue, T. *Phys. Chem. Chem. Phys.* **2010**, *12*, 10012.

(24) Cornut, R.; Poirier, S.; Mauzeroll, J. *Anal. Chem.* **2012**, *84*, 3531.

(25) Nebel, M.; Eckhard, K.; Erichsen, T.; Schulte, A.; Schuhmann, W. *Anal. Chem.* **2010**, *82*, 7842.

(26) Yamada, H.; Fukumoto, H.; Yokoyama, T.; Koike, T. *Anal. Chem.* **2005**, *77*, 1785.

(27) Lee, Y.; Ding, Z.; Bard, A. J. *Anal. Chem.* **2002**, *74*, 3634.

(28) McKelvey, K.; Edwards, M. A.; Unwin, P. R. *Anal. Chem.* **2010**, *82*, 6334.

(29) McKelvey, K.; Snowden, M. E.; Peruffo, M.; Unwin, P. R. *Anal. Chem.* **2011**, *83*, 6447.

(30) McGeouch, C.-A.; Peruffo, M.; Edwards, M. A.; Bindley, L. A.; Lazenby, R. A.; Mbogoro, M. M.; McKelvey, K.; Unwin, P. R. *J. Phys. Chem. C* **2012**, *116*, 14892.

(31) Edwards, M. A.; Whitworth, A. L.; Unwin, P. R. *Anal. Chem.* **2011**, *83*, 1977.

(32) Wipf, D. O.; Bard, A. J. *Anal. Chem.* **1992**, *64*, 1362.

(33) Bard, A. J.; Fan, F. R. F.; Kwak, J.; Lev, O. *Anal. Chem.* **1989**, *61*, 132.

(34) Unwin, P. R.; Bard, A. J. *J. Phys. Chem.* **1991**, *95*, 7814.

(35) D. Martin, R.; R. Unwin, P. *J. Chem. Soc., Faraday Trans.* **1998**, *94*, 753.

(36) Dolgaleva, I.; Gorichev, I.; Izotov, A.; Stepanov, V. *Theor. Found. Chem. Eng.* **2005**, *39*, 614.

(37) Compton, R. G.; Unwin, P. R. *Phil. Trans. R. Soc. A* **1990**, *330*, 1.

(38) Berner, R. A.; Morse, J. W. *Am. J. Sci.* **1974**, *274*, 108.

(39) Sverdrup, H. *Chemica Scripta* **1983**, *22*, 12.

(40) Finneran, D. W.; Morse, J. W. *Chem. Geol.* **2009**, *268*, 137.

(41) Arvidson, R. S.; Ertan, I. E.; Amonette, J. E.; Luttge, A. *Geochim. Cosmochim. Acta* **2003**, *67*, 1623.

(42) Sjoberg, E. L.; Rickard, D. T. *Geochim. Cosmochim. Acta* **1984**, *48*, 485.

(43) Sjoberg, E. L.; Rickard, D. T. *Chem. Geol.* **1984**, *42*, 119.

(44) McGeouch, C.-A.; Edwards, M. A.; Mbogoro, M. M.; Parkinson, C.; Unwin, P. R. *Anal. Chem.* **2010**, *82*, 9322.

(45) Kwak, J.; Bard, A. J. *Anal. Chem.* **1989**, *61*, 1221.

(46) Rudd, N. C.; Cannan, S.; Bitziou, E.; Ciani, I.; Whitworth, A. L.; Unwin, P. R. *Anal. Chem.* **2005**, *77*, 6205.

(47) Barwise, A. J.; Compton, R. G.; Unwin, P. R. *J. Chem. Soc., Faraday Trans.* **1990**, *86*, 137.

(48) Compton, R. G.; Pritchard, K. L.; Unwin, P. R.; Grigg, G.; Silvester, P.; Lees, M.; House, W. A. *J. Chem. Soc., Faraday Trans. I* **1989**, *85*, 4335.

(49) Jones, C. E.; Unwin, P. R.; Macpherson, J. V. *ChemPhysChem* **2003**, *4*, 139.

(50) Amphlett, J. L.; Denuault, G. *J. Phys. Chem. B* **1998**, *102*, 9946.

(51) Rudd, N. C.; Cannan, S.; Bitziou, E.; Ciani, I.; Whitworth, A. L.; Unwin, P. R. *Anal. Chem.* **2005**, *77*, 6205.

(52) Lefrou, C. *J. Electroanal. Chem.* **2006**, *592*, 103.

(53) Cornut, R.; Lefrou, C. *J. Electroanal. Chem.* **2007**, *608*, 59.

(54) Burt, D. P.; Wilson, N. R.; Janus, U.; Macpherson, J. V.; Unwin, P. R. *Langmuir* **2008**, *24*, 12867.

4 Nanoscale Intermittent Contact-Scanning Electrochemical Microscopy

A major theme in scanning electrochemical microscopy (SECM) is methodology for nanoscale imaging with distance control and positional feedback of the tip. The expansion of intermittent contact (IC)-SECM to the nanoscale is reported, using disk-type Pt nanoelectrodes prepared using the laser-puller sealing method. The Pt was exposed using a focused ion beam milling procedure to cut the end of the electrode to a well-defined glass sheath radius, which could also be used to reshape the tips to reduce the size of the glass sheath. This produced nanoelectrodes that were slightly recessed, which was optimal for IC-SECM on the nanoscale, as it served to protect the active part of the tip. A combination of finite element method simulations, steady-state voltammetry and scanning electron microscopy, for the measurement of critical dimensions, was used to estimate Pt recession depth. With this knowledge, the tip-substrate alignment could be further estimated by tip approach curve measurements. IC-SECM has been implemented by using a piezo-bender actuator for the detection of damping of the oscillation amplitude of the tip, when IC occurs, which was used as a tip position feedback mechanism. The piezo-bender actuator improves significantly on the performance of our previous setup for IC-SECM, as the force acting on the sample due to the tip is greatly reduced, allowing studies with more delicate tips. The capability of IC-SECM is illustrated with studies of a model electrode (metal/glass) substrate.

4.1 Introduction

Since its inception, about two decades ago by Bard and co-workers,[1] imaging using scanning electrochemical microscopy (SECM) has mainly been limited to the use of ultramicroelectrode (UME) tips with characteristic dimensions on the 1-25 μm scale.[2,3] For nanoscale electrochemical imaging, *i.e.* the use of electrodes of several hundred nanometres active diameter or smaller, which operate at (similar or smaller) nanoscale distances from the substrate, a positional feedback mechanism is necessary, unless imaging is over small areas on a flat substrate and with stringent isothermal conditions.[4] SECM imaging without positional feedback, known as constant-height mode, leaves the tip susceptible to crashing into or drifting away from the surface, especially if the tip and substrate are not well aligned, or there is creep in the piezoelectric positioners.

Various attempts have been made to implement independent tip-substrate distance control and measurement for SECM at the nanoscale. Shearforce distance regulation has been used to provide positional feedback,[5,6] with constant-distance nanoscale imaging achieved.[7] The tip resonates laterally and the amplitude of this oscillation decreases when the tip is moved within a few hundred nanometres of the surface, due to the shear forces acting between tip and substrate.[8-10] Wipf and Bard introduced tip-position modulation (TPM) SECM,[11] in which the tip is oscillated with a small amplitude in the direction perpendicular to the substrate and the resulting AC and DC currents are measured. In principle, this can be used to determine both the activity and topography of a surface[12] and this approach can also be used for distance control.[13]

A constant-distance mode, in which the tip traces the contours of the surface based on the tip current, has been used,[14] but there is the issue of how to separate unambiguously the topography and activity of the sample; a problem which can be addressed by implementing a voltage switching mode.[15] Another approach has been to integrate an UME into a tip for atomic force microscopy (AFM), in combined SECM-AFM,[16-20] with high resolution tips having been made using nanowires grown on single-walled carbon nanotubes.[21] Nanoscale SECM is also possible by performing the scan in a thin liquid layer, which means the tip does not require insulation, in a technique comparable to scanning tunneling microscopy (STM).[22] An ion current between two ideally non-polarizable electrodes can also be used to provide pure distance control, as demonstrated by scanning ion conductance microscopy (SICM).[23] Tips having two electrodes have been successfully used for dual function imaging: a SICM component for topography, and a solid electrode for redox activity imaging.[24-26]

An issue of many combined techniques is that they often require the fabrication of specially-designed tips. However, positional feedback can also be achieved with conventional SECM probes. This has most recently been seen in intermittent contact (IC)-SECM,[27] where the tip is oscillated normal to the surface of interest (as in TPM) and upon physical contact between tip and substrate the oscillation is damped, which can be used as a setpoint for approach curve measurements and imaging. This technique has already been implemented for the visualisation of electrode activity,[28] for non-electrochemical tip-positioning[29] and for probing molecular transport across dentin.[30] However, in all of these applications, IC-SECM has so far been limited to micron-scale probes.

The preparation of Pt disk nanoelectrodes is now well known,[31-33] with electrode radii as low as 1 nm reported.[34] Nanoelectrodes have recently been reviewed,[35] and reports of such tips being used for nanoscale electrochemical imaging in SECM are now appearing.[36,37] Polished Pt-disk nanoelectrodes have been used for constant-height imaging, using an electrochemical response to determine topography,[36] and similar probes have also been used for electrochemical imaging of cells.[37] For pulled Pt tips, the Pt may be exposed using hydrofluoric acid to etch the glass to produce a finite cone-shaped electrode,[38] or by micropolishing the tip to produce a disk electrode.[32] Here, a robust and reliable method is used to focused ion beam (FIB) mill tips to ensure a flat electrode, with a recessed Pt disk, that is cut to a precise glass sheath thickness to give a probe with a typical *RG* value, defined as the ratio of the radius of the insulating glass sheath, r_{glass}, to the radius of the electrode, a. The FIB milling procedure has been used in the production of SECM-SICM tips.[24,26] Here it is used to shape electrodes to yield symmetrical probes with *RG* values close to 10. Although FIB milling was used for tip fabrication here, electrode micropolishing is a more readily available alternative, but control over tip geometry and size would be more challenging.

In order to implement nanoscale IC-SECM, improvements on the original instrument design are reported,[27] with the introduction of a piezo-bender actuator, which has a much smaller spring constant than the piezoelectric positioner used previously,[27] and provides greater sensitivity in the detection of tip oscillation amplitude damping. This is a key requirement for the implementation of IC-SECM with fragile nanoelectrodes.

4.2 Simulations

4.2.1 Recessed electrodes

Steady-state finite element method (FEM) simulations of mass transport to a recessed disk-shaped UME were carried out to quantify the effect of electrode recession on the diffusion-limited current in a 1 mM $FcTMA^+$ solution. A steady-state diffusion equation (Fick's second law), describes the mass transport of $FcTMA^+$ in this system,

$$D\nabla^2 c = 0 \qquad (4.1)$$

where D is the diffusion coefficient, which is set to 6.0×10^{-6} cm^2 s^{-1},[39] and c is the concentration of $FcTMA^+$. Rotational symmetry allowed a two-dimensional (2D) axisymmetric cylindrical geometry to be used, as shown in Figure 4-1. The electrode radius, a in Figure 4-1, was set to 70 nm and the amount of glass surround was set to 10a. These critical tip dimensions were based on SEM measurements of the electrode used, which was done for each electrode studied. The size of the simulation, b in Figure 4-1, was set to 50 μm, and the recession depth, r in Figure 4-1, varied. The concentration of $FcTMA^+$ at the electrode (boundary 2 in Figure 4-1) was set to zero (c = 0). The glass area of the electrode (boundaries 3, 4 and 5 in Figure 4-1) were set to no flux ($\nabla c \cdot \mathbf{n} = 0$), where **n** is the unit normal vector. The bulk solution (boundaries 6, 7 and 8 in Figure 4-1) was set to bulk concentration (c = 1 mM). Finally, the rotational symmetry axis (boundary 1 in Figure 4-1) was set as a symmetry boundary condition ($\nabla c \cdot \mathbf{n} = 0$). Simulations were run on a personal computer (WindowsXP Pro 64 bit) using COMSOL Multiphysics 4.2 (Comsol AB, Sweden).

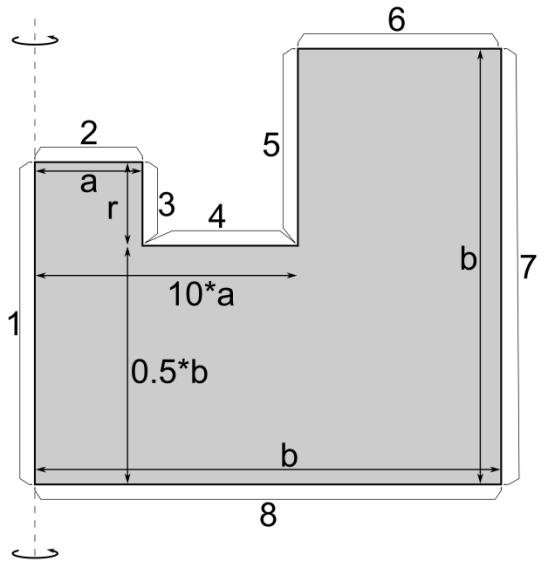

Figure 4-1. The simulation domain (including dimensions and boundary labels), as described in the supporting text, for a 2D FEM simulation of a recessed planar disk-shaped UME. Not to scale.

4.2.2 Approach curves

Steady-state FEM simulations of a recessed disk-shaped planar UME, at an angle with respect to an inert insulating substrate, and as a function of distance from the substrate, were carried out to quantify the effect of probe angle on the distance-dependent current (approach curve) response. As above, Equation (4.1) (Fick's second law), describes the mass transport of $FcTMA^+$ to the electrode, but the incorporation of the probe angle breaks the rotational symmetry and therefore a three-dimensional (3D) simulation, with one plane of mirror symmetry, was used. Figure 4-2 shows a 2D diagram of the geometry, with probe dimensions, as well as the 3D simulation domain (which, again, is not drawn to scale), with the boundaries marked.

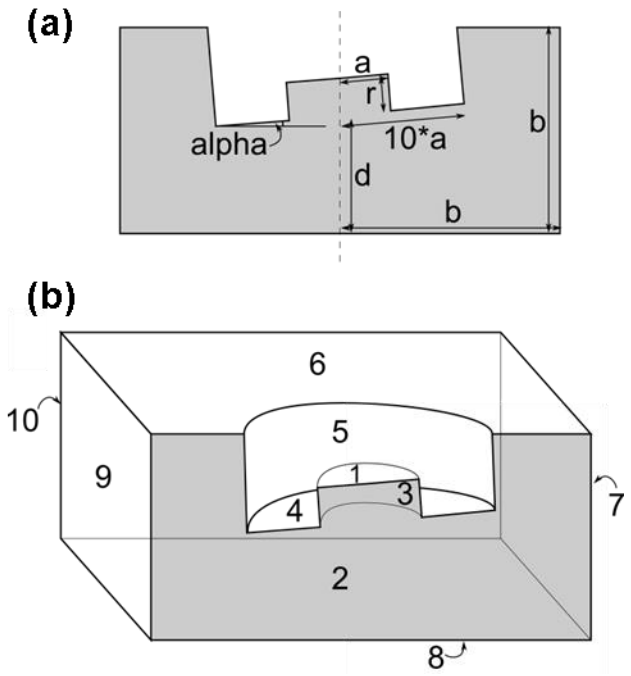

Figure 4-2. (a) 2D representation of the geometry, including dimensions, of the angled recessed UME above a surface. (b) The simulation domain (including boundary labels), as described in the main text, for 3D FEM simulations of a recessed planar disk-shaped UME above an insulating surface. Not to scale.

The simulation domain is defined by the probe dimensions, shown in Figure 4-2(a), and described above. In addition, the probe angle, *alpha* in Figure 4-2(a), and distance to the surface, *d* in Figure 4-2(a), are independent variables. The boundary conditions, shown in Figure 4-2(b), of the FEM simulation are as follows: 1 is the electrode surface and the concentration is set to zero (c = 0); 2 is the mirror symmetry plane and is set to have no normal flux ($\nabla c \cdot \mathbf{n} = 0$); 3, 4 and 5 are the glass surrounds of the probe and are set to have no normal flux ($\nabla c \cdot \mathbf{n} = 0$); 6, 7, 9 and 10 are the bulk solution and set to the bulk concentration (c = 1 mM); and 8 is the insulating surface and set to have no flux ($\nabla c \cdot \mathbf{n} = 0$).

4.3 Tip characterisation

Pt-disk nanoelectrodes were fabricated reproducibly and reliably with the active electrode radius typically in the range of 50 – 150 nm, exposed by FIB milling using the protocol shown schematically in Figure 2-2(a), in which a series of cuts are used to produce an electrode with a well-defined (and relatively small) *RG* value.

As formed, nanoelectrodes were typically asymmetric, with an *RG* value between 20 and 30, and this is likely due to the position of the Pt wire in the glass capillary during the sealing step. A typical nanoelectrode is shown end-on in the SEM micrograph in Figure 4-3(c) and (d). This asymmetry has recently been studied, and for *RG* values in this range does not have any significant effect on the approach curve with respect to the value expected based on the average *RG* value.[40]

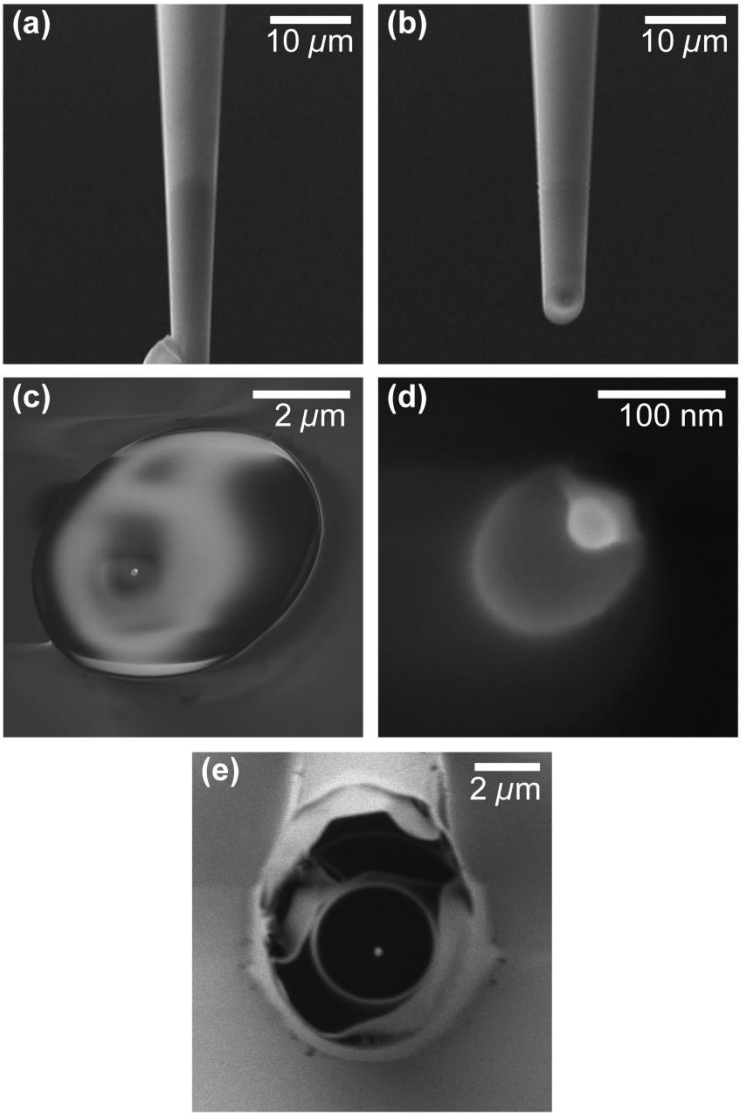

Figure 4-3. SEM micrographs of a nanoelectrode before (a) and after (b) FIB milling, viewed at 52 ° to the normal top down view. Top down view SEM micrographs of a Pt-disk nanoelectrode after FIB milling (c) and (d) of the cut surface after the procedure in (a) and (b) and (e) an electrode shaped by FIB milling.

4.3.1 FIB milling of carbon-filled electrode

Also, showing that the FIB-milling technique can be applied to other electrodes, a quartz capillary that contains a pyrolised carbon electrode is shown in Figure 4-4.

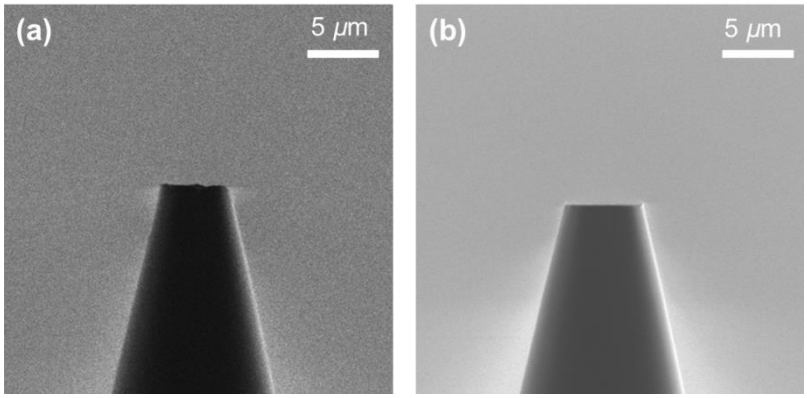

Figure 4-4. FIB-SEM micrographs of a milled quartz capillary, before (a) and after (b) the milling process.

The quartz capillaries were filled with carbon, in a procedure described elsewhere,[41,42] which produced the carbon electrodes with a rough surface. The FIB milling procedure was used to cut off the end of the probe, revealing a smoother and flatter surface, properties that would allow the probe to get closer to a substrate surface below. This is an example of another type of probe that could be improved for its application using the FIB milling procedure described here.

4.3.2 Pt nanoelectrode characterisation

The dimension of the exposed Pt surface can be characterized reasonably by measurement in the SEM. A typical SEM micrograph used to characterize tip dimensions has been included for a single electrode in Figure 4-3(c). The tip shown has a 70 ± 10 nm radius, determined by SEM. A cyclic voltammogram (CV) for the oxidation of 1 mM $FcTMA^+$ (0.1 M KCl) at a scan rate of 200 mV s^{-1} is shown in Figure 4-5(a), which shows a characteristic steady-state response. By holding the tip in bulk solution at the steady-state limiting potential, 0.45 V, a steady current of 2.51

pA was recorded. A non-recessed electrode would have given a steady-state limiting current of 16.2 pA for this electrochemical reaction. If one naively assumed a planar disk geometry, as has sometimes been done in the past, the tip radius would be calculated as 10 nm, using the steady-state limiting current, i_{ss}, equation for a disk electrode (for an infinite RG[43]), see Equation (1.14).

That nanoscale tips are often recessed is increasingly recognized and additional characterisation methods proposed to determine the geometry have been proposed.[44-46] As highlighted herein, a recessed electrode is actually beneficial for application in IC-SECM as it serves to protect the active part of the tip.

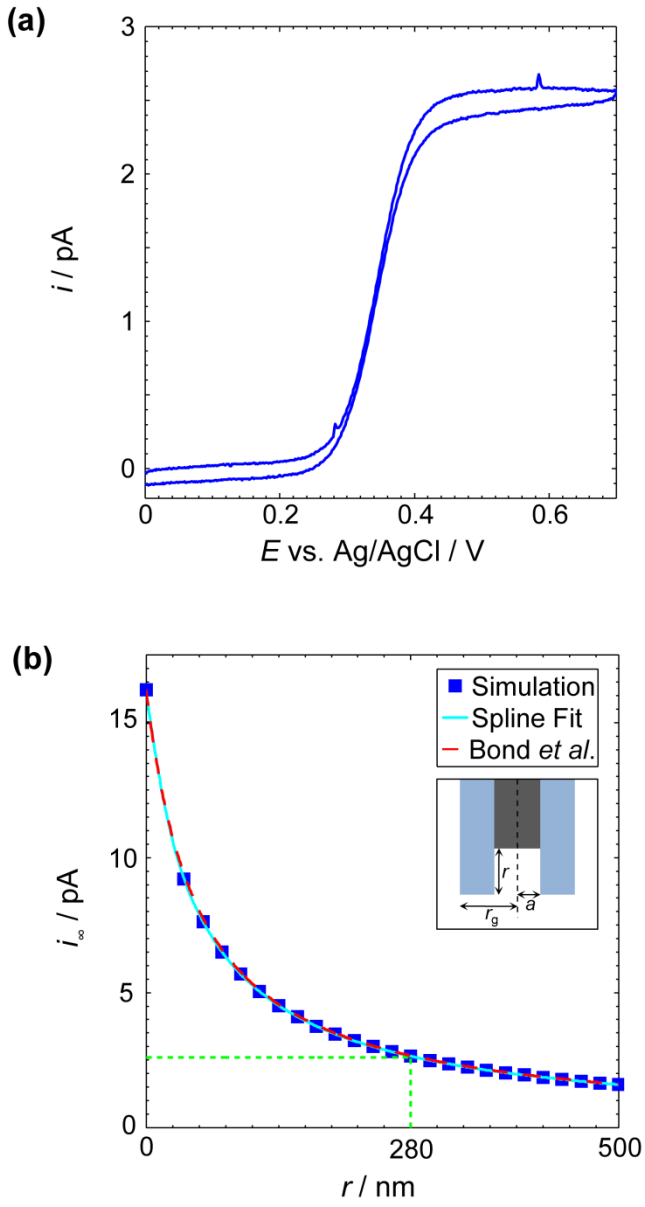

Figure 4-5. (a) CV recorded for a recessed 70 nm radius electrode (characterized by SEM) in 1 mM $FcTMA^+$ and 0.1 M KCl, at a scan rate of 200 mV s^{-1}. (b) Simulated steady-state diffusion-limited currents in bulk solution *vs.* Pt recession distance, *r*, in nm for a 70 nm radius planar disk electrode. Simulated results (blue) have been spline fitted (light blue) and theoretical results by Bond *et al.* are shown (red dashed).[47] The experimental diffusion-limited current, 2.51 pA, (green dotted) was used to determine *r*, for this electrode. Inset shows key tip dimensions: electrode radius, *a*, glass sheath radius, r_g, and Pt recession depth, *r*.

The steady-state limiting current for the electrodes were always less than predicted for a non-recessed disk electrode based on SEM measurements of the electrode radius, indicating that the tips were recessed to varying degrees.[46-48] In the case of the tip considered above, the Pt radius as measured in SEM was *ca*. 7 times greater than the radius calculated from the steady-state limiting current in the bulk. It should be considered that this discrepancy could partly be due to charging effects of the Pt sealed in the insulating glass making it appear larger in the SEM than it actually is. This aspect was considered recently by Tefashe and Wittstock, who studied micropolished Pt electrodes of sub-micron dimensions.[49] In their study, the nanoelectrode and glass sheath were coated in an ionic liquid to reduce such effects,[50] yet a similar disparity was observed to that herein (*e.g.* the radius measured in SEM was 348 nm, *c.f.* 53 nm calculated from i_{ss}). In our case, the electrodes were grounded to the tip holder in the SEM to reduce charging effects.

It is concluded that the main reason for the difference in electrode dimensions from SEM and voltammetry is that the electrode is recessed, probably for reasons recently identified by Amemiya and co-workers.[51] Although some blockage of the active electrode as well cannot be ruled out, additional information from approach curves indicates that recession is the main reason for the much diminished bulk current (*vide infra*). The extent of recession was estimated via FEM simulations, as described above, using the well characterized electrode dimensions from the SEM measurements. For the tip shown in Figure 2-2(b), the model predicted a series of diffusion-limited currents in bulk solution for a series of recession depths, *r*, as shown in Figure 4-5(b) (inset). The relationship of limiting current of the tip in the bulk against Pt recession depth shown in Figure 4-5(b) allowed an estimate of 280 nm for the recession depth.

The effect of recession depth on the steady-state limiting current has been studied by others; Bond's model works for deeply recessed electrodes,[47] whilst the model by Bartlett applies also to shallow recessed electrodes.[48] It can be seen that the FEM model herein matches reasonably closely to the result by Bond *et al.*, included in Figure 4-5.[47] AFM has also been used to visualise the surface of nanoelectrodes,[44] and white light vertical scanning interferometry can be used to measure the recession of an electrode, although this is limited to electrodes of several to several tens of microns dimension.[45] Our approach to measure the recession is fast and simple, based on the characterisation by SEM and the diffusion-limited steady-state current.

4.4 Approach curves

Importantly, by deploying IC-SECM with nanoelectrodes, it was found that the detection of oscillation amplitude damping is possible for small (nanoscale) tips. An amplitude setpoint of 95 % of that in the bulk was used for approach curves and imaging. A typical negative feedback approach curve to glass is shown in Figure 4-6(a), with the oscillation amplitude, δ, shown in green. In the approach, damping is first observed when the current has fallen by *ca.* 5 %, *i.e.* just beyond the noise level of *ca.* 2 % of the oscillation amplitude, although further extension of the tip into the surface leads to the oscillation amplitude and tip current decreasing further. These needle-type nanoelectrodes possessed a large degree of flexibility in the shaft of the tip, which was advantageous in allowing the tip to bend slightly, rather than snap, as it was pushed against the substrate. Since the alignment between the tip and substrate was unknown, d / a was arbitrarily set to zero at the point of IC detection.

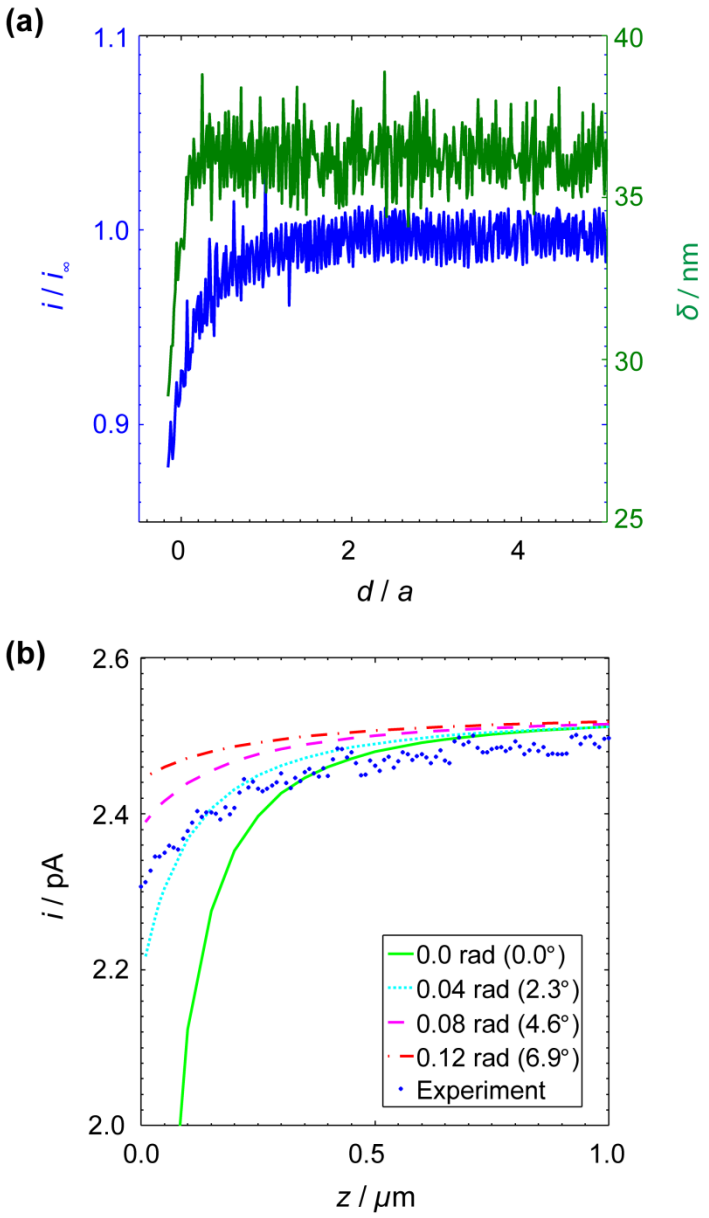

Figure 4-6. (a) Feedback approach curve to a glass (insulator) substrate with a 70 nm radius Pt nanoelectrode (characterized by SEM) oscillated at 70 Hz, δ = 36 nm in IC-SECM mode. The electrode potential was fixed at a value where 1 mM $FcTMA^+$ in bulk solution underwent diffusion-limited oxidation at the tip electrode. The normalized current at the tip (blue) and corresponding oscillation amplitude of the tip (green) are shown as a function of the tip-substrate separation where d / a = zero corresponds to IC detection. (b) Simulated approach curves for tip angles with respect to the surface of 0 (green), 0.04 (light blue dotted), 0.08 (pink dashed) and 0.12 radians (red dashed-dotted) against the experimental approach from part (a) (blue).

Using the known recession of the tip from the model shown in Figure 4-6, the same electrode was modelled approaching the surface at different angles in order to find the misalignment between tip and substrate. Here, $z = 0$ μm corresponds to IC detection (*i.e.* $d \neq 0$ when *alpha* > 0), and the model did not consider tip bending. The low damping setpoint ensures tip bending is minimised. Greater damping could lead to tip bending. IC-SECM detects IC, and there may be tip bending which would occur to a greater extent, the higher the oscillation amplitude damping. To minimise this, the smallest damping factor, that can clearly be discerned was chosen (*vide supra*). Since the tip current at the point at which IC was detected did not drop much beyond 90 % of the bulk current, Figure 4-6 shows that the tip was misaligned to the substrate somewhere between 0.04 and 0.08 radians, or about 3 ° or so, which appears reasonable and suggests that recession of the electrode is the main reason for the greatly reduced currents in bulk compared to expectations based on a coplanar electrode of dimensions identified in SEM.

A key component of the soft-tapping IC-SECM setup is the implementation of the piezo bender actuator, in which the tip exerts less force on the sample. Using the manufacturer's spring constants of 0.6 N μm^{-1} for the piezoelectric positioner used in our previous setup (PI Hera P-621.ZCD) and 0.02 N μm^{-1} for the bender actuator implemented in this new setup (PICMA P-871.112) the forces applied by the tip on the sample are estimated to be 3×10^{-3} N and 1×10^{-4} N respectively, based on a displacement of 5 nm from the damping of the oscillation of the tip. These values are upper limits with these nanoscale tips because tip bending may actually greatly reduce the force applied. Thus in this setup, the force of the tip on the sample, when the tip is mounted on the bender actuator is *ca*. 3 % of the force when the tip is mounted directly on to the piezoelectric positioner. The force exerted by the piezo

bender actuator is of the same order as found for soft linear array imaging devices.[52,53]

4.5 Imaging with nanoelectrodes

A gold band array on glass was used as a substrate for IC-SECM imaging in feedback mode. An optical image of the substrate is given in Figure 4-7(a). The 125 nm height of the gold band (Figure 4-7(c)) was not detectable in the topography for the area imaged by SECM, since the glass sheath surrounding the Pt nanoelectrode was *ca.* 3.6 μm. The AFM image shows that the edge of the gold band is not perfectly straight due the lift off process in the fabrication of the sample, therefore a rough edge was also expected in the electrochemical image. The radius of the Pt nanoelectrode used for IC-SECM imaging of the sample was 160 nm, as determined by SEM, and a view of the tip above the substrate taken *in situ* is shown in Figure 4-7(b).

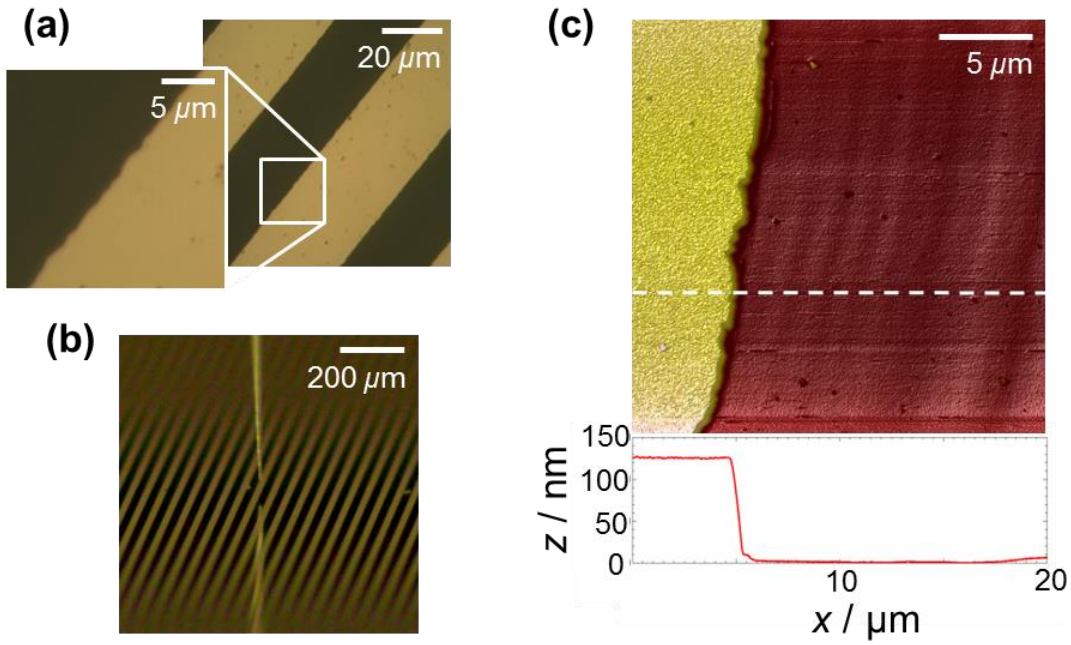

Figure 4-7. (a) Optical microscope image of the gold band sample, with a zoomed-in inset over the edge of a gold band. (b) View of the tip above the substrate prior to IC-SECM imaging. (c) AFM topography image of the substrate with inset of a line scan.

Figure 4-8(a) shows the feedback SECM image recorded with the tip in IC-mode, *i.e.* tracing the contours of the surface. When the tip is over the gold substrate, there is some positive feedback leading to current values with respect to bulk that are enhanced, *i.e.* $i / i_\infty > 1$. Over the glass part of the substrate surface, negative feedback occurs, with diffusion to the tip blocked leading to $i / i_\infty < 1$. For the reverse scan line, the tip was 300 nm away (in the *z*-direction) from the position of IC with the surface. This image shows both lower resolution and lower deviation of local currents from the bulk current value, since the probe is further away from – and thus less sensitive to the nature of – the surface.

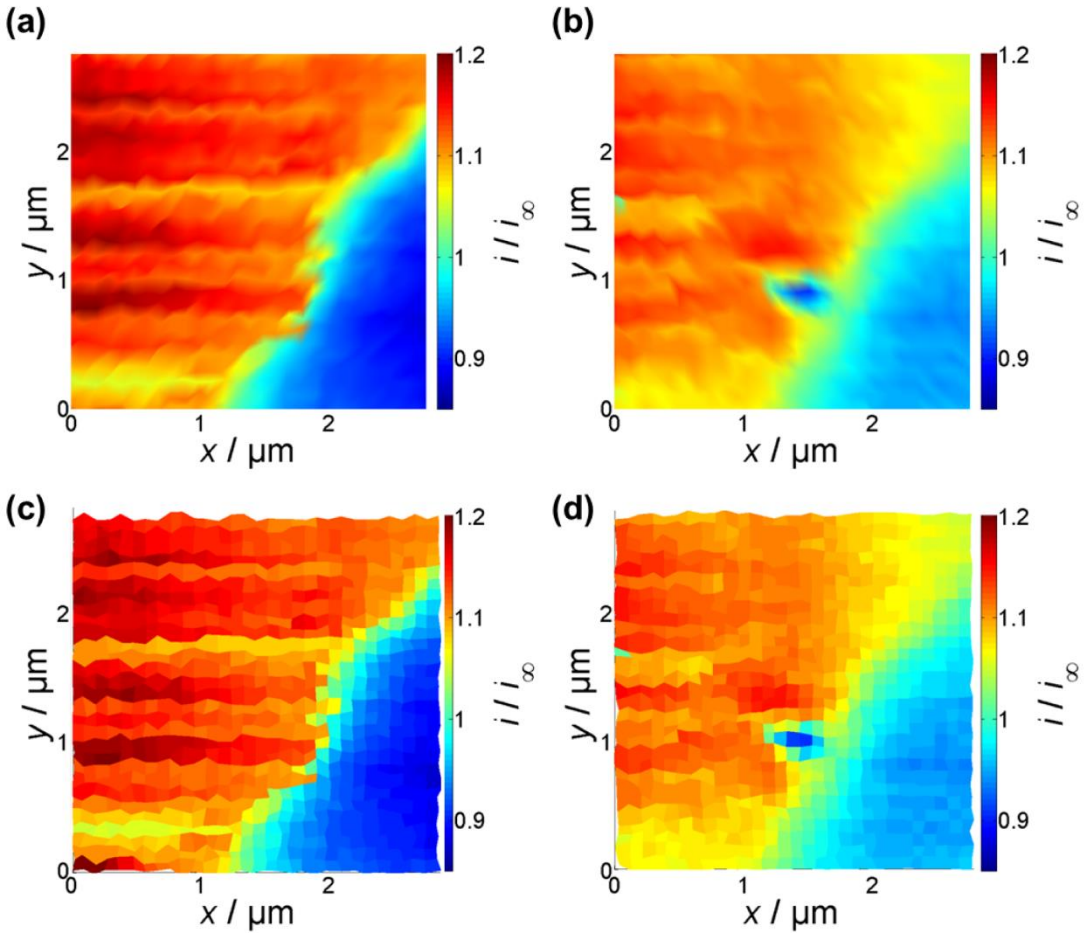

Figure 4-8. IC-SECM images of the edge of a gold band on glass, obtained using a 160 nm radius Pt disk electrode (80 Hz, δ = 39 nm, 1 mM $FcTMA^+$). Forward scan in IC of mean tip current/bulk current (a), and reverse scan of mean tip current/bulk current at constant separation of 300 nm (b). The IC-SECM maps before rendering are shown for the forward (c) and reverse (d) scans.

The feature exhibiting negative feedback in the reverse scan and positive feedback in the forward scan (at x = 1.5 μm, y = 1 μm) can be attributed to surface contamination during the forward scan of the gold substrate by the tip. This clearly only affects a few pixels around one point in the image, and with the development of hopping IC-SECM,[54,55] the amount of contact between the tip and the substrate is expected to reduce by > 99 %, which would overcome such problems in the future. Figure 4-8(c)

and (d) show the same data as those of (a) and (b), respectively, before image rendering, which shows that only a few pixels are affected by the surface contamination feature. The images are made of 30 × 30 pixels in *x* and *y*, and the plot showing one pixel per data point shows that the image rendering does not distort features in the original image. The *x* and *y* positions are given as recorded by the piezo, rather than the programmed positions set by the LabVIEW programme, so there is some variation between the desired location and the actual position, resulting in pixels that are not of equal size.

Notice that the tip current over the glass (insulator) in Figure 4-8(b) was *ca.* 90 % of that in the bulk, which – although for a different tip – is in line with the approach curve in Figure 4-6. The resolution of the tip is clearly much greater than for a typical micron sized UME, since a change from gold to glass occurs over a lateral distance of 200 nm at worst in Figure 4-8(a).

4.6 Conclusions

It has been shown that nanoscale imaging is possible with IC-SECM, using Pt-disk electrodes fabricated by laser pulling, and cut to a desired shape by FIB milling. The tips were found to be recessed, and the degree of recession was determined based on the disparity between the steady-state limiting current and the apparent size of the electrode based on SEM measurements. In addition, (mis)alignment between the electrode and the substrate surface was estimated based on the recession depth determined, through approach curve measurements. The recessed nature of these tip electrodes is particularly useful for IC-SECM in that it acts to protect the active electrode when it comes into contact with the surface. Although the results presented herein are for amperometric tips over a model substrate, potentiometric probes could be used with this technique.

The implementation of the piezo-bender actuator was important in the realization of IC-SECM for nanoelectrodes. It is anticipated that this technique could be applied to image samples with features of nanometre dimensions, such as individual carbon nanotubes, or low density single-walled carbon nanotube networks. The smaller force of the tip on the sample when using the piezo-bender actuator, as compared to the *z*-piezoelectric positioner used in our previously described setup, could allow for the imaging of softer samples, with greater topographical sensitivity. Future work could also consider the use of hopping scanning,[54,55] to eliminate lateral forces on the tip during the imaging, while allowing the tip to move closer to the sample by increasing the setpoint of the damping of the oscillation amplitude.

4.7 References

(1) Bard, A. J.; Fan, F. R. F.; Kwak, J.; Lev, O. *Anal. Chem.* **1989**, *61*, 132.

(2) Amemiya, S.; Bard, A. J.; Fan, F.-R. F.; Mirkin, M. V.; Unwin, P. R. *Annu. Rev. Anal. Chem.* **2008**, *1*, 95.

(3) Schulte, A.; Nebel, M.; Schuhmann, W. *Annu. Rev. Anal. Chem.* **2010**, *3*, 299.

(4) Kim, J.; Shen, M.; Nioradze, N.; Amemiya, S. *Anal. Chem.* **2012**, *84*, 3489.

(5) Ludwig, M.; Kranz, C.; Schuhmann, W.; Gaub, H. E. *Rev. Sci. Instrum.* **1995**, *66*, 2857.

(6) Cougnon, C.; Bauer-Espindola, K.; Fabre, D. S.; Mauzeroll, J. *Anal. Chem.* **2009**, *81*, 3654.

(7) Ballesteros Katemann, B.; Schulte, A.; Schuhmann, W. *Electroanalysis* **2004**, *16*, 60.

(8) Etienne, M.; Anderson, E. C.; Evans, S. R.; Schuhmann, W.; Fritsch, I. *Anal. Chem.* **2006**, *78*, 7317.

(9) Lee, Y.; Ding, Z.; Bard, A. J. *Anal. Chem.* **2002**, *74*, 3634.

(10) Buchler, M.; Kelley, S. C.; Smyrl, W. H. *Electrochem. Solid-State Lett.* **2000**, *3*, 35.

(11) Wipf, D. O.; Bard, A. J. *Anal. Chem.* **1992**, *64*, 1362.

(12) Edwards, M. A.; Whitworth, A. L.; Unwin, P. R. *Anal. Chem.* **2011**, *83*, 1977.

(13) Wipf, D. O.; Bard, A. J.; Tallman, D. E. *Anal. Chem.* **1993**, *65*, 1373.

(14) Kurulugama, R. T.; Wipf, D. O.; Takacs, S. A.; Pongmayteegul, S.; Garris, P. A.; Baur, J. E. *Anal. Chem.* **2005**, *77*, 1111.

(15) Takahashi, Y.; Shevchuk, A. I.; Novak, P.; Babakinejad, B.; Macpherson, J.; Unwin, P. R.; Shiku, H.; Gorelik, J.; Klenerman, D.; Korchev, Y. E.; Matsue, T. *Proc. Natl. Acad. Sci. U. S. A.* **2012**, *109*, 11540.

(16) Macpherson, J. V.; Unwin, P. R. *Anal. Chem.* **2000**, *72*, 276.

(17) Kranz, C.; Friedbacher, G.; Mizaikoff, B.; Lugstein, A.; Smoliner, J.; Bertagnolli, E. *Anal. Chem.* **2001**, *73*, 2491.

(18) Salomo, M.; Pust, S. E.; Wittstock, G.; Oesterschulze, E. *Microelectron. Eng.* **2010**, *87*, 1537.

(19) Kueng, A.; Kranz, C.; Mizaikoff, B.; Lugstein, A.; Bertagnolli, E. *Appl. Phys. Lett.* **2003**, *82*, 1592.

(20) Dobson, P. S.; Weaver, J. M. R.; Holder, M. N.; Unwin, P. R.; Macpherson, J. V. *Anal. Chem.* **2005**, *77*, 424.

(21) Burt, D. P.; Wilson, N. R.; Weaver, J. M. R.; Dobson, P. S.; Macpherson, J. V. *Nano Lett.* **2005**, *5*, 639.

(22) Fan, F.-R. F.; Bard, A. J. *Proc. Natl. Acad. Sci. U. S. A.* **1999**, *96*, 14222.

(23) Hansma, P. K.; Drake, B.; Marti, O.; Gould, S. A.; Prater, C. B. *Science* **1989**, *243*, 641.

(24) Takahashi, Y.; Shevchuk, A. I.; Novak, P.; Murakami, Y.; Shiku, H.; Korchev, Y. E.; Matsue, T. *J. Am. Chem. Soc.* **2010**, *132*, 10118.

(25) Takahashi, Y.; Shevchuk, A. I.; Novak, P.; Zhang, Y.; Ebejer, N.; Macpherson, J. V.; Unwin, P. R.; Pollard, A. J.; Roy, D.; Clifford, C. A.; Shiku, H.; Matsue, T.; Klenerman, D.; Korchev, Y. E. *Angew. Chem., Int. Ed.* **2011**, *50*, 9638.

(26) Comstock, D. J.; Elam, J. W.; Pellin, M. J.; Hersam, M. C. *Anal. Chem.* **2010**, *82*, 1270.

(27) McKelvey, K.; Edwards, M. A.; Unwin, P. R. *Anal. Chem.* **2010**, *82*, 6334.

(28) Patten, H. V.; Meadows, K. E.; Hutton, L. A.; Iacobini, J. G.; Battistel, D.; McKelvey, K.; Colburn, A. W.; Newton, M. E.; Macpherson, J. V.; Unwin, P. R. *Angew. Chem., Int. Ed.* **2012**, *51*, 7002.

(29) McGeouch, C.-A.; Peruffo, M.; Edwards, M. A.; Bindley, L. A.; Lazenby, R. A.; Mbogoro, M. M.; McKelvey, K.; Unwin, P. R. *J. Phys. Chem. C* **2012**, *116*, 14892.

(30) McKelvey, K.; Snowden, M. E.; Peruffo, M.; Unwin, P. R. *Anal. Chem.* **2011**, *83*, 6447.

(31) Mezour, M. A.; Morin, M.; Mauzeroll, J. *Anal. Chem.* **2011**, *83*, 2378.

(32) Ballesteros Katemann, B.; Schuhmann, W. *Electroanalysis* **2002**, *14*, 22.

(33) Zuliani, C.; Walsh, D. A.; Keyes, T. E.; Forster, R. J. *Anal. Chem.* **2010**, *82*, 7135.

(34) Li, Y.; Bergman, D.; Zhang, B. *Anal. Chem.* **2009**, *81*, 5496.

(35) Cox, J. T.; Zhang, B. *Annu. Rev. Anal. Chem.* **2012**, *5*, 253.

(36) Laforge, F. O.; Velmurugan, J.; Wang, Y.; Mirkin, M. V. *Anal. Chem.* **2009**, *81*, 3143.

(37) Sun, P.; Laforge, F. O.; Abeyweera, T. P.; Rotenberg, S. A.; Carpino, J.; Mirkin, M. V. *Proc. Natl. Acad. Sci. U. S. A.* **2008**, *105*, 443.

(38) Shao, Y.; Mirkin, M. V.; Fish, G.; Kokotov, S.; Palanker, D.; Lewis, A. *Anal. Chem.* **1997**, *69*, 1627.

(39) Bertoncello, P.; Ciani, I.; Li, F.; Unwin, P. R. *Langmuir* **2006**, *22*, 10380.

(40) Cornut, R.; Bhasin, A.; Lhenry, S.; Etienne, M.; Lefrou, C. *Anal. Chem.* **2011**, *83*, 9669.

(41) McKelvey, K.; Nadappuram, B. P.; Actis, P.; Takahashi, Y.; Korchev, Y. E.; Matsue, T.; Robinson, C.; Unwin, P. R. *Anal. Chem.* **2013**, *85*, 7519.

(42) Nadappuram, B. P.; McKelvey, K.; Al Botros, R.; Colburn, A. W.; Unwin, P. R. *Anal. Chem.* **2013**, *85*, 8070.

(43) Lefrou, C.; Cornut, R. *ChemPhysChem* **2010**, *11*, 547.

(44) Nogala, W.; Velmurugan, J.; Mirkin, M. V. *Anal. Chem.* **2012**, *84*, 5192.

(45) Chang, J.; Leonard, K. C.; Cho, S. K.; Bard, A. J. *Anal. Chem.* **2012**, *84*, 5159.

(46) Sun, P.; Mirkin, M. V. *Anal. Chem.* **2007**, *79*, 5809.

(47) Bond, A. M.; Luscombe, D.; Oldham, K. B.; Zoski, C. G. *J. Electroanal. Chem.* **1988**, *249*, 1.

(48) Bartlett, P. N.; Taylor, S. L. *J. Electroanal. Chem.* **1998**, *453*, 49.

(49) Tefashe, U. M.; Wittstock, G. *C. R. Chim.* **2013**, *16*, 7.

(50) Arimoto, S.; Kageyama, H.; Torimoto, T.; Kuwabata, S. *Electrochem. Commun.* **2008**, *10*, 1901.

(51) Nioradze, N.; Chen, R.; Kim, J.; Shen, M.; Santhosh, P.; Amemiya, S. *Anal. Chem.* **2013**.

(52) Cortés-Salazar, F.; Momotenko, D.; Lesch, A.; Wittstock, G.; Girault, H. H. *Anal. Chem.* **2010**, *82*, 10037.

(53) Lesch, A.; Momotenko, D.; Cortés-Salazar, F.; Wirth, I.; Tefashe, U. M.; Meiners, F.; Vaske, B.; Girault, H. H.; Wittstock, G. *J. Electroanal. Chem.* **2012**, *666*, 52.

(54) Novak, P.; Li, C.; Shevchuk, A. I.; Stepanyan, R.; Caldwell, M.; Hughes, S.; Smart, T. G.; Gorelik, J.; Ostanin, V. P.; Lab, M. J.; Moss, G. W. J.; Frolenkov, G. I.; Klenerman, D.; Korchev, Y. E. *Nat. Methods* **2009**, *6*, 279.

(55) Lazenby, R. A.; McKelvey, K.; Unwin, P. R. *Anal. Chem.* **2013**, *85*, 2937.

5 Nucleation, Aggregative Growth and Detachment of Metal Nanoparticles During Electrodeposition at Electrode Surfaces

The nucleation and growth of metal nanoparticles on surfaces is of considerable interest with regard to creating functional interfaces with myriad applications. Yet, key features of these processes remain elusive and are undergoing revision. Here, the mechanism of the electrodeposition of silver on basal plane highly oriented pyrolytic graphite (HOPG) is investigated on a wide range of length scales, spanning electrochemical measurements at the macroscale to the nanoscale using scanning electrochemical cell microscopy (SECCM), a scanning pipette-based approach. The macroscale measurements show that the nucleation process is neither truly instantaneous nor progressive, based on classical models, and that step edge sites of HOPG do not play a dominant role in nucleation events compared to the HOPG basal plane, as has been widely proposed. Moreover, nucleation numbers expected from electrochemical analysis do not match those studied by atomic force microscopy (AFM). The high time and spatial resolution of the nanoscale pipette setup reveals individual nucleation and growth events that are resolved and analysed in detail. Based on these results, corroborated with complementary microscopy measurements, a nucleation-growth-detachment mechanism is proposed as an important feature of the electrodeposition of silver NPs on HOPG. These findings have major implications for NP electrodeposition and for understanding electrochemical processes at graphitic materials generally.

5.1 Introduction

The properties of metal nanoparticles (NPs) can differ significantly from their bulk analogues, and are even tuneable through the size and shape of the particle. Examples of properties that depend on NP size and shape include interatomic bond distances,[1,2] melting point,[1,3] chemical reactivity[4-6] and optical and electronic properties.[1,7,8] This powerful control over the fundamental properties has given rise to a huge variety of applications of metal NPs, including in sensing,[9,10] spectroscopy,[10-12] catalysis,[5,13,14] as optical filters,[15] and in biomedical[16-18] and antimicrobial applications.[19,20] In many of these applications, NPs are often dispersed as arrays on a support material.

A wide variety of techniques can be used to prepare supported NPs.[21-30] For conducting supports, electrodeposition is particularly attractive as it allows the direct growth of NPs on a substrate, thereby ensuring electrical connection between the substrate and the NPs. Furthermore, it circumvents the need for NP stabilising surfactants, which may impact NP reactivity.[13] Electrodeposition can offer control over the size- and shape-distribution, as well as the spatial distribution of NPs, by tuning the deposition parameters and electrolyte composition.[29,31]

Analysis of the current-time-voltage characteristics during deposition can reveal insights into the electrodeposition mechanism.[30,32-34] However, such studies typically involve the deposition of large numbers of NPs, with the macroscopic current-time-voltage characteristics fitted with continuous mathematical models to extract nanoscale mechanistic information on the elementary processes involved in NP electronucleation. Interpretation of such data is further complicated by overlapping diffusion fields of neighbouring NPs,[35] surface-mediated Ostwald ripening,[36,37] and

heterogeneities in substrate properties (*e.g.* different types of nucleation sites).[28] Whilst there are some reports of the electrodeposition of one or a few NPs (< 10), [33,38-40] they have usually required the use of nanoscale electrodes to restrict the number of nucleation sites, but such electrodes are non-trivial to fabricate and fully characterize.[40,41] Additionally, the need to encapsulate electrodes in an insulating support severely restricts the range of electrode materials and surface preparations that can be used.

Here, the electrodeposition of silver (Ag) on (the basal surface of) highly oriented pyrolytic graphite (HOPG) is examined at both the macroscale and nanoscale, making use of scanning electrochemical cell microscopy (SECCM)[42,43] as a nanoscopic electrochemical cell. This system is particularly interesting for a number of reasons. First, Ag deposition on HOPG is often studied as a model system for metal deposition on carbon electrodes, displaying fast heterogeneous electron transfer kinetics.[44-48] However, previous studies indicate that this process cannot be modelled satisfactorily as either instantaneous or progressive nucleation and growth, instead seemingly showing intermediate behaviour.[45,49,50] Evidently, new insights would be hugely valuable for furthering understanding. Second, the active sites for metal electrodeposition on HOPG have been a topic of debate.[28,44,45,47,51] For example, the commonly accepted model is that electronucleation occurs solely on step edge and defect sites, with the basal plane being completely inert. However, in light of recent findings on HOPG basal plane reactivity for other electrochemical processes,[48,52-61] it is timely and important to readdress this model for metal electrodeposition. Specifically, the macroscale experiments described will be affected by *both basal and step edge sites*, which means samples of different step edge density (varied by more than two orders of magnitude herein) can be compared

to explore the contribution of step edges towards nucleation of nanoparticles. For the nanoscale experiments, given the spatial resolution of SECCM (a few hundred nm), this platform enables the study of the intrinsic activity of the *basal plane alone* towards NP deposition without any influence from step edges. Third, a further discrepancy can be found in the apparent density of nucleation sites, inferred by electrochemistry and those measured by microscopy. *Ex situ* characterisation typically shows a nucleation site density a few orders of magnitude higher than that obtained by modelling the current-time response.[44,62] Finally, the ability to cleave and characterize HOPG[54] offers a clean and reproducible surface characterized by low background currents, thus allowing dynamic measurements to be performed with good time resolution and an appreciable signal-to-noise ratio.

5.2 Silver electrodeposition on macroscopic HOPG surfaces

To investigate the role of step edge sites, the electrodeposition of Ag on two HOPG samples was studied: AM grade and SPI-3 grade. The key difference between the two samples is the mean step density, which differs, on average, by a factor of 400.[58] This is shown in Figure 5-1. Thus, these samples are ideally suited to investigate the role of step edges in the electrodeposition of Ag; any significant difference in reactivity between step edges sites and basal plane sites would be expected to result in an enormous difference in kinetics, as reflected in the currents for the electrodeposition process. Surprisingly, while the key (often exclusive) role of step edges in the electrodeposition at HOPG has been reported in many papers,[50,63-66] there appears to be no previous work that has investigated the effect of step edge density by examining different grades of HOPG.

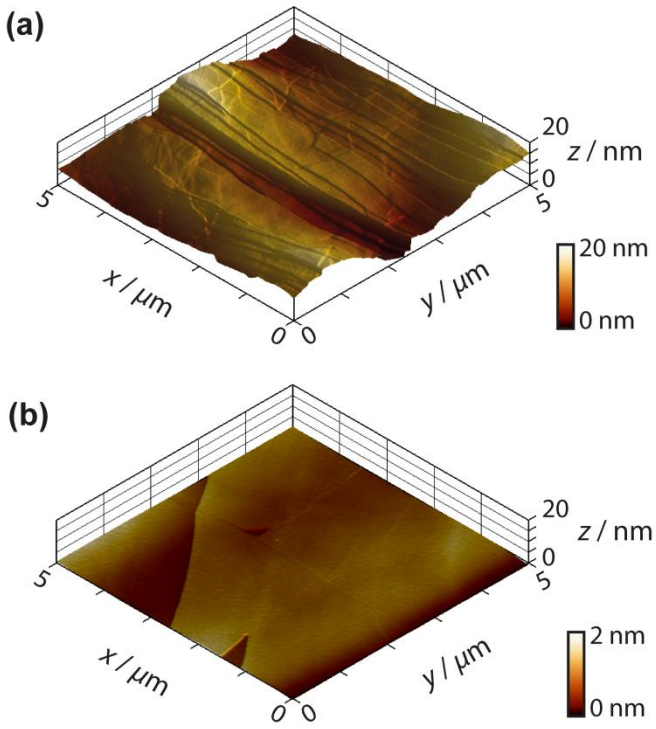

Figure 5-1. AFM images of SPI-3 HOPG (a) and AM grade HOPG (b) using images from Figure 2-6. Note that the colour scale for height is different, but the *z* scale is the same for each.

Cyclic voltammograms (CVs) were recorded on both grades of HOPG, at 100 mV s^{-1} and 1 V s^{-1}. The first voltammetric cycles for both surfaces are shown in Figure 5-2, and display the characteristic signatures of metal electrodeposition on carbon surfaces.[28,45] On the cathodic sweeps, a small nucleation overpotential (*ca.* 50 mV at 100 mV s^{-1}, *ca.* 100 mV at 1 V s^{-1}) is observed, leading to a characteristic peak that can be attributed to Ag electrodeposition. Reversal of the potential sweep direction gives rise to an anodic peak related to the Ag dissolution process. The total charge under the peaks is a measure of the amount of Ag deposited or dissolved (depending on the sweep direction), and was the same for both processes. It can be seen that the CVs look virtually identical (peak currents, onset potentials and total charges) for

both grades of HOPG, indicative of the same processes (thermodynamic and kinetic) occurring on both grades of HOPG at this timescale, even though the surface structure is hugely different.

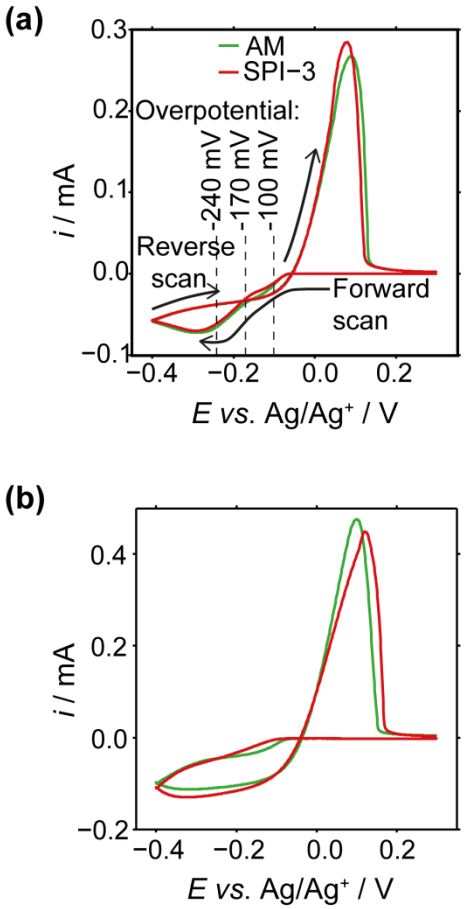

Figure 5-2. CVs of Ag electrodeposition and stripping (electrodissolution) on AM (green) and SPI-3 (red) HOPG, at 100 mV s^{-1} (a) and 1 V s^{-1} (b). The vertical lines signify several overpotentials at which current-time measurements were carried out.

Typical current-time transients for the electrodeposition of Ag at different overpotentials indicated in Figure 5-2(a) are shown in Figure 5-3. The general morphology of these traces is that the current initially increases with time, representing the nucleation and growth of NPs that are (largely) diffusionally

isolated, reaching a peak value followed by a decrease with time due to diffusional overlap (and, planar diffusion) of Ag^+ to the resulting NP array. The peak moves to shorter time with increasing driving force, (a) to (c), and the value is smaller (and slightly later) for AM grade HOPG. This tentatively suggests a smaller number of nucleating NPs on AM grade HOPG, although the behaviour of the two grades gets more similar with increasing driving force, (a) to (c). Moreover, comparing the current-time transients of the two grades of HOPG side by side, the difference between them is not as significant as might be expected, if step edges were the exclusive nucleation and growth sites, based on the huge difference in step density. These observations thus strongly suggest that electrodeposition can occur to a significant extent on basal plane sites.

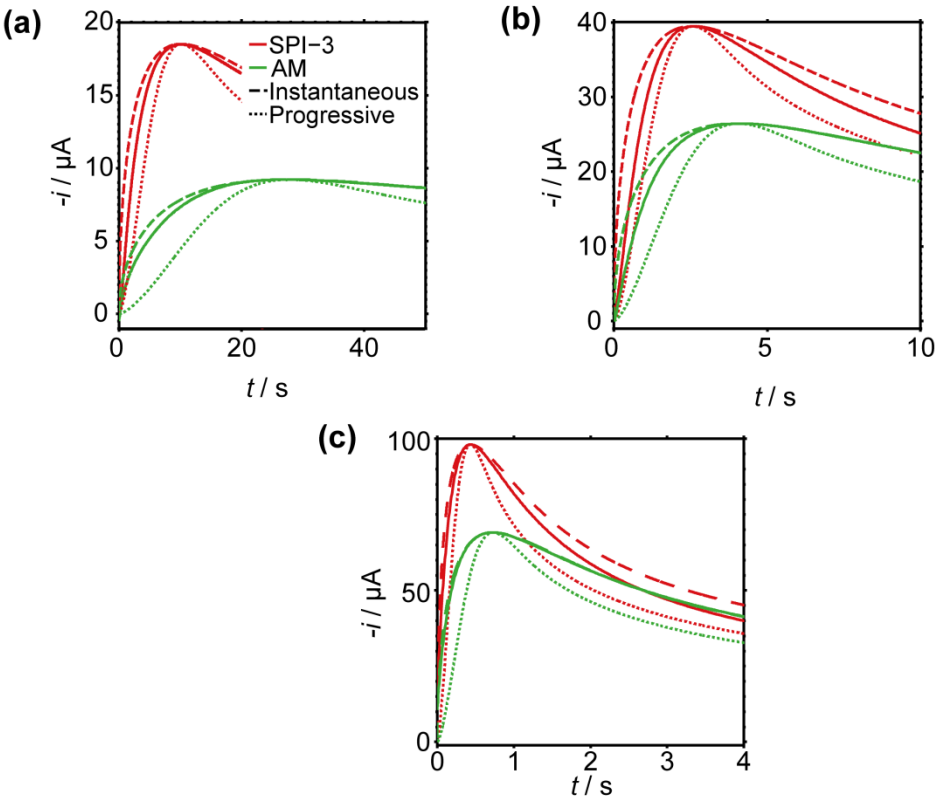

Figure 5-3. Current-time transients of Ag electrodeposition in a macroscopic droplet cell on AM (green lines) and SPI-3 (red lines) HOPG at (a) –100 mV, (b) –170 mV and (c) –240 mV. Theoretical fits to the Scharifker-Hills models for instantaneous (dashed) and progressive (dotted) nucleation are shown for each case.

Also shown in Figure 5-3 are the Scharifker-Hills fits for the current-time transients, both for instantaneous nucleation, using Equation (1.21), and progressive nucleation, using Equation (1.22).[30] Each transient has a value of I_m and t_m that have been used to show these two limiting cases. Models of this type are widely used to analyse chronoamperometric data for NP nucleation and growth,[67,68] but it can be seen that the rising part of the transients cannot be described adequately by either instantaneous nucleation or progressive nucleation, instead showing intermediate nucleation behaviour, consistent with previous studies as discussed in the Introduction.[30,32-34] Nonetheless, the number of apparent nucleation sites can be

extracted from the Scharifker-Hills model using either the peak current (I_m) or the time of the peak (t_m),[30] and are shown in Table 1. The concentration of Ag^+ is taken to be the bulk concentration, *i.e.* 1 mM.

Table 5-1. Apparent number of nucleation sites extracted from the current-time transients for Ag electrodeposition on HOPG based on the Scharifker-Hills model, using the maximum current density, I_m, and time at maximum current, t_m.

Potential / mV	**Estimated nucleation site density, N / ($\times 10^5$ cm^{-2})**		
	Method used	**AM**	**SPI-3**
–100	I_m	0.6	2.4
	t_m	0.6	1.6
–170	I_m	4.9	11
	t_m	4.1	6.4
–240	I_m	34	68
	t_m	23	38

It can be seen that the apparent number of nucleation sites on SPI-3 HOPG is roughly twice that on AM, even though the step edge density is two orders of magnitude higher. Regardless of the quality of the HOPG (highly stepped compared to few steps), the apparent numbers of nucleation sites are within the range of 10^5 – 10^6, again consistent with previous findings.[45,62] This semi-quantitative analysis points to a significant role of the basal surface in the NP nucleation and growth process.

To compare the apparent number of nucleation sites based on a Scharifker-Hills analysis with the number of deposited particles, HOPG substrates were characterised after deposition by FE-SEM and TM-AFM. It should be borne in mind that *ex situ* characterisation of metal NPs electrodeposited on HOPG can be complicated by the rather weak interaction between most metal NPs and the surface of sp^2 carbon materials, particularly the HOPG basal plane (*vide infra*).[62,69-72] Moreover, these measurements were made without KNO_3 supporting electrolyte, as noted earlier, although this did not have significant effect on the deposition transients. Thus, careful sample preparation and critical examination of the results from *ex situ* characterisation can provide powerful information on the electrodeposition process,[44,62,73] and at least allows an estimate of the minimum number of NPs electrodeposited. Representative images are shown in Figure 5-4.

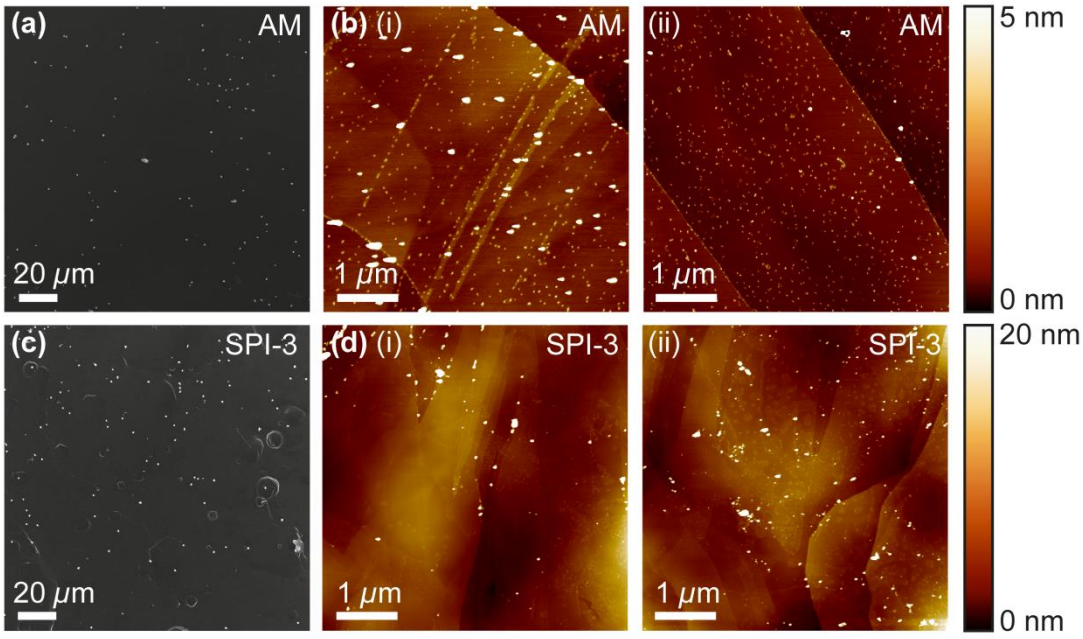

Figure 5-4. (a) FE-SEM image and (b-i and b-ii) AFM images (two different areas) of macroscale electrodeposition of Ag (from 1 mM $AgNO_3$) on AM grade HOPG. (c) FE-SEM image and (d-i and d-ii) AFM images (two different areas) of macroscale electrodeposition on SPI-3 HOPG. The electrodeposition potential was −100 mV, held for 1 s.

Analysis of images, such as those shown in Figure 5-4, is shown in Table 5-2. TM-AFM particles were analysed for multiple scan areas, whilst particles observed by SEM where counted over a 370 μm^2 area. A lower limit height threshold for particles observed by TM-AFM was set to 10 nm, which removed the effect of salt crystals, which can be seen in Figure 5-4(b) and (d). It was shown that when no deposition was carried out, salt crystals from the KNO_3 solution were present (see Figure 5-5).

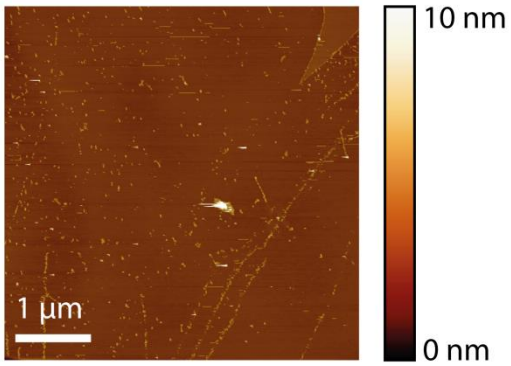

Figure 5-5. Tapping mode-atomic force microscopy (TM-AFM) image of AM grade HOPG, after exposure to a droplet of 50 mM KNO_3.

The macroscale deposition experiment was repeated using a "blank" solution (*i.e.* no $AgNO_3$ present, although supporting electrolyte was used) and without a potential applied. The droplet was removed, as described in the main text, and the surface was imaged by TM-AFM. Many features can be observed on the surface, below the 10 nm threshold, which can be attributed to salt residue, since no electrodeposition was carried out.

The particles observed by FE-SEM were much larger, given the lower resolving power of this microscope. Particles greater than 100 nm diameter (typically ~ 1 μm) where counted. These larger particles where not observed by TM-AFM, since the regions between them were studied exclusively; images shown were chosen to deliberately avoid these much larger particles.

Table 5-2. Number of deposited particles from TM-AFM and FE-SEM analysis of macroscale deposition at –100 mV *vs*. Ag/Ag^+.

TM-AFM Image Analysis	**AM**	**SPI-3**
Particles / ($\times 10^8$ cm^{-2})	1.8 ± 1.1	3.6 ± 2.8
Particle size (height) / nm	24 ± 10	19 ± 13
FE-SEM Image Analysis	**AM**	**SPI-3**
Particles / ($\times 10^7$ cm^{-2})	5.0 ± 0.3	3.6 ± 0.5

This *ex situ* analysis showed that the number of electrodeposited particles was in the range of 10^7 – 10^8 cm^{-2}, about two orders of magnitude higher than the number of apparent nucleation sites as obtained from analysis of the chronoamperometric transients (10^5 – 10^6 cm^{-2}, *vide supra*).

5.3 Nanoscale silver deposition on HOPG using SECCM

Evidently, there is a considerable disparity between electrochemical data analysed with the SH model and morphological analysis. Furthermore, a comparison of electrodeposition on AM and SPI-3 grade HOPG suggests a significant contribution of the basal surface to electrodeposition. Thus, to gain further insight into the process, Ag deposition on AM grade HOPG with SECCM was investigated to elucidate the role of the HOPG basal plane, in isolation from step edge sites. Pipettes

of *ca.* 400 nm diameter were employed, thus limiting the effective working electrode area to the same dimensions. As AM grade HOPG typically provides surfaces with extensive basal planes (>> 1 μm spacing between steps),[54] this means that the contact area will typically only be the basal plane, with no step edges.

Typical current-time responses for Ag electrodeposition at potentials of –50 mV, –100 mV and –200 mV are shown in Figure 5-6(a), where t = 0 corresponds to the initial contact between the electrolyte droplet and the substrate, which was then held in place for 1 s. Similar trends are observed at the different potentials: before t = 0 s and after t = 1 s, there is no appreciable current as the electrolyte droplet is not in contact with the substrate. Between t = 0 s and t = 1 s, when there is contact between the electrolyte and the substrate, a finite current due to Ag electrodeposition can be observed. Interestingly, the current is manifested as *ca.* 100 – 150 discrete events in the 1 s period, rather than in a continuous way. Closer inspection of these current events (Figure 5-6(b)) reveals them to show a marked time-dependence: starting from the baseline value, the current surges to reach a maximum within *ca.* 200 μs. The maximum is followed by a slower decay over 3 – 5 ms, after which the current rapidly drops back to the baseline level. After another few milliseconds, the current rises again for the next current event. Furthermore, by comparing the current-time transients at the different potentials, it can be seen that the duration of the individual currents are relatively constant. The initial part (peak) of the current events increases with more cathodic potentials (increasing overpotential). This potential-dependence is also evident in the distribution of the total charge associated with each current event (Figure 5-6(c)), increasing from 135 ± 35 fC at –50 mV to 204 ± 36 fC at –100 mV to 279 ± 29 fC at –200 mV.

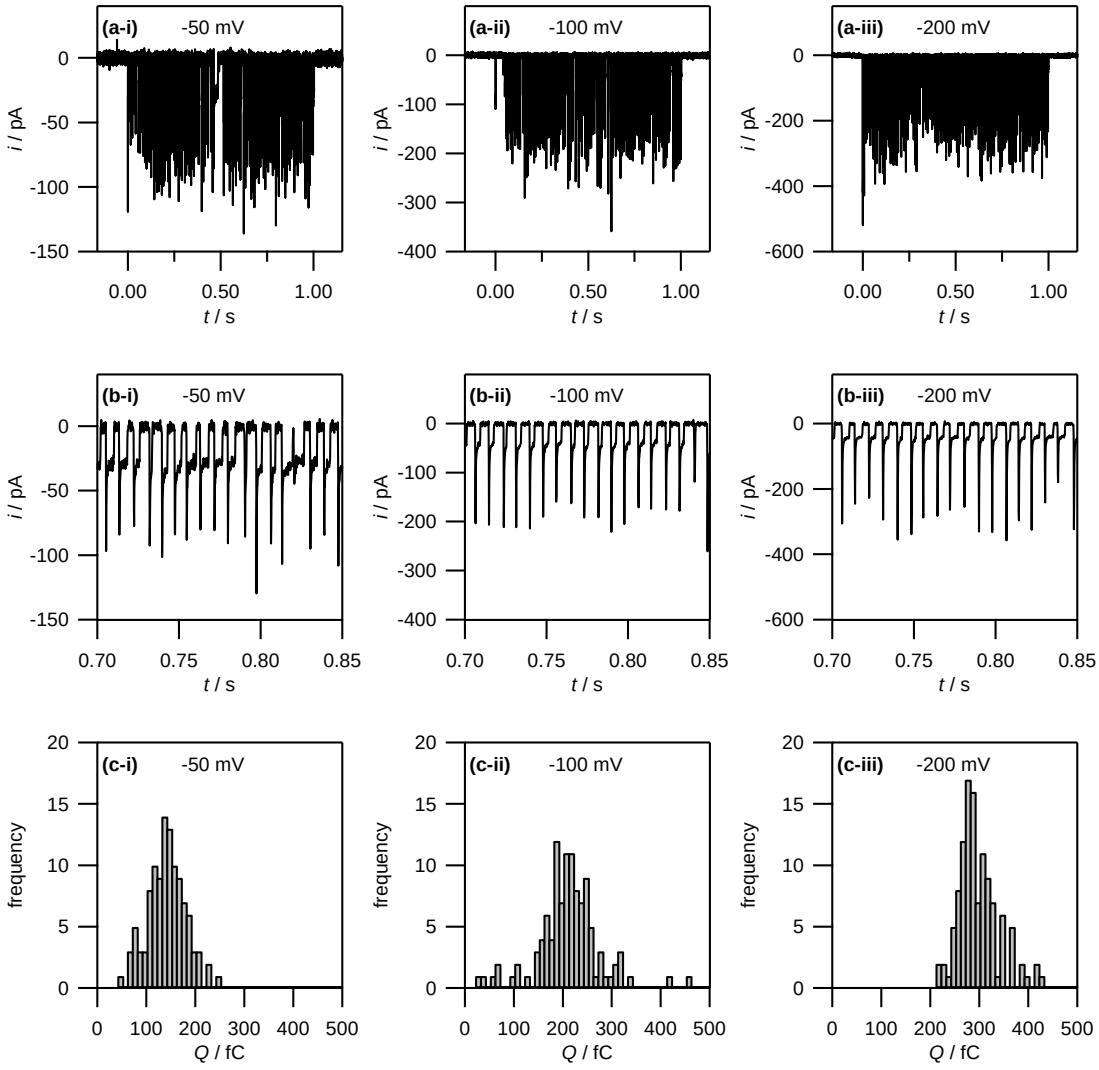

Figure 5-6. (a) Current-time traces for the electrodeposition of Ag (from 1 mM $AgNO_3$ in 50 mM KNO_3) on HOPG at –50 mV, –100 mV and –200 mV. Note that no electrodeposition takes place before t = 0 s and after t = 1 s as the electrolyte droplet is not in contact with the substrate. (b) Zoom-in on the current-time traces in (a) to show the discrete current events. (c) Histogram of the charges associated with the discrete current events.

Here, it is proposed that each current event is related to nucleation of Ag at multiple sites, aggregative growth and detachment of one or a few AgNPs. Figure 5-7 shows an example of a series of current events at each potential, with high temporal resolution.

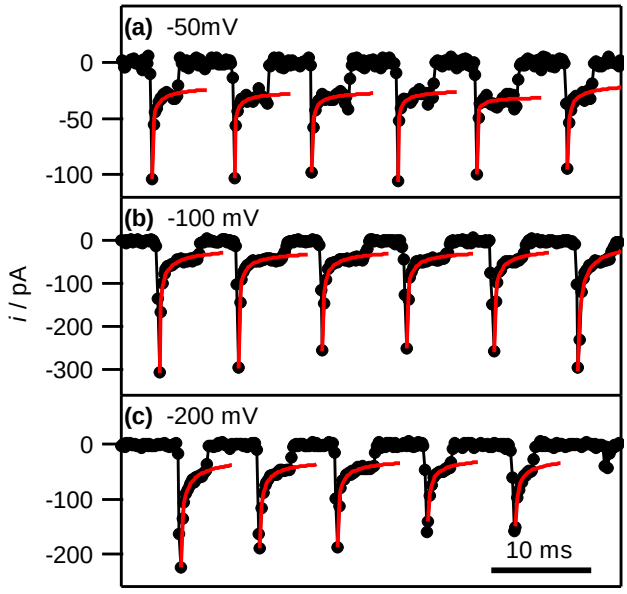

Figure 5-7. Experimental current-time traces (black connected circles) and fits of the individual current events to Equation (5.1) (red lines; see main text) at the indicated potentials. The full range of the horizontal axis corresponds to 50 ms.

While the initial rise in current for each event is too fast to consider in detail at the sampling rate employed, it provides important information on the quantity of nuclei that must be forming. The current for the electrodeposition of a single spherical particle is given by[74]

$$i(t) = \frac{2\pi nF(Dc^*)^{3/2} M^{1/2} t^{1/2}}{\rho^{1/2}} \qquad (5.1)$$

where n (=1) is the number of electrons in the redox process, F is the Faraday constant (F = 96,485 C mol^{-1}), D is the diffusion coefficient (D = 1.5 × 10^{-5} cm^2 s^{-1}),[75] c^* is the bulk concentration (c^* = 1.0 × 10^{-6} mol cm^{-3}), M is the molar mass of the deposited metal (107.87 g mol^{-1}), t is the time (in s), and ρ is the density (10.49 g cm^{-3}). This equation yields a current of 1.6 pA for t = 200 μs, which is clearly much smaller than the values obtained in Figure 5-7, and points to the electrodeposition of

around 50 to 200 particles in each event. NPs nucleate and rapidly achieve diffusional overlap, leading to an immediate diffusion controlled growth regime (*vide infra*), *i.e.* quasi-linear diffusion of Ag^+ ions down the barrels of the pipette, to the HOPG surface.

The current decay occurs over the course of several milliseconds, allowing further analysis. In particular, Figure 5-7 shows that the current decay for the individual current events at all potentials can be described by a modified Cottrell equation for a micro- or nanoelectrode:[76]

$$i(t) = nFAc^*(D/\pi t)^{1/2} + nFAc^*k_T \qquad (5.2)$$

where A is the effective surface area of the electrode (in cm^2), and k_T is the steady-state mass transport coefficient (in cm s^{-1}), which strongly depends on the geometry of the system. This equation assumes the reaction to be driven at the maximum rate, which is reasonable for applied overpotentials of –100 mV and –200 mV, but will work less well for –50 mV. Nonetheless it provides a reasonable approach for the semiquantitative interpretation of electrochemical data.

By fitting all current events to Equation (5.2), using the A and k_T as the two fitting parameters, values were obtained for $A = 3.2 \pm 1.3 \times 10^{-9}$ cm^2 (corresponding to a disk electrode with radius of *ca.* 300 nm) and $k_T = 0.05 \pm 0.02$ cm s^{-1} for electrodeposition at –50 mV. The fits of the current events at –100 mV and –200 mV reveal broadly similar values (see Table 5-3).

Table 5-3. Results of the modified Cottrell fits at different potentials.

	Potential			
	-50 mV	**-100 mV**	**-200 mV**	**Average over all potentials**
Area / (10^{-9} cm^2)	3.2 ± 1.3	6.9 ± 2.8	7.4 ± 3.3	5.6 ± 3.2
Corresponding radius (/nm)	319 ± 65	469 ± 95	485 ± 108	422 ± 121
k_T / (10^{-2} cm s^{-1})	4.8 ± 2.4	3.6 ± 2.7	3.7 ± 1.9	3.9 ± 2.6

The obtained values for *A* are in reasonable agreement with the pipette size, further supporting that the growth of the NPs after the initial current peak is governed by quasi-linear diffusion down the pipette towards the HOPG surface (*vide infra*). Similarly, the steady-state mass transfer coefficient is an order of magnitude lower than for an inlaid disk electrode of the same radius,[76]

$$k_{\mathrm{T,disk}} = 4D/\pi a \qquad (5.3)$$

where *a* is the disk radius, which has been found to be the typical magnitude for (sub-)micrometre sized pipettes with cone angles *ca.* 8 – 10 ° as used herein.[52,77]

Interestingly, after a few ms, the current ceases rather abruptly, which is assigned to the detachment of Ag from the surface. Afterwards, there is a small induction time before the next current event (*vide infra*).

To corroborate NP formation, the HOPG surface was examined after an electrochemical experiment performed at −50 mV with high resolution microscopy (Figure 5-8).

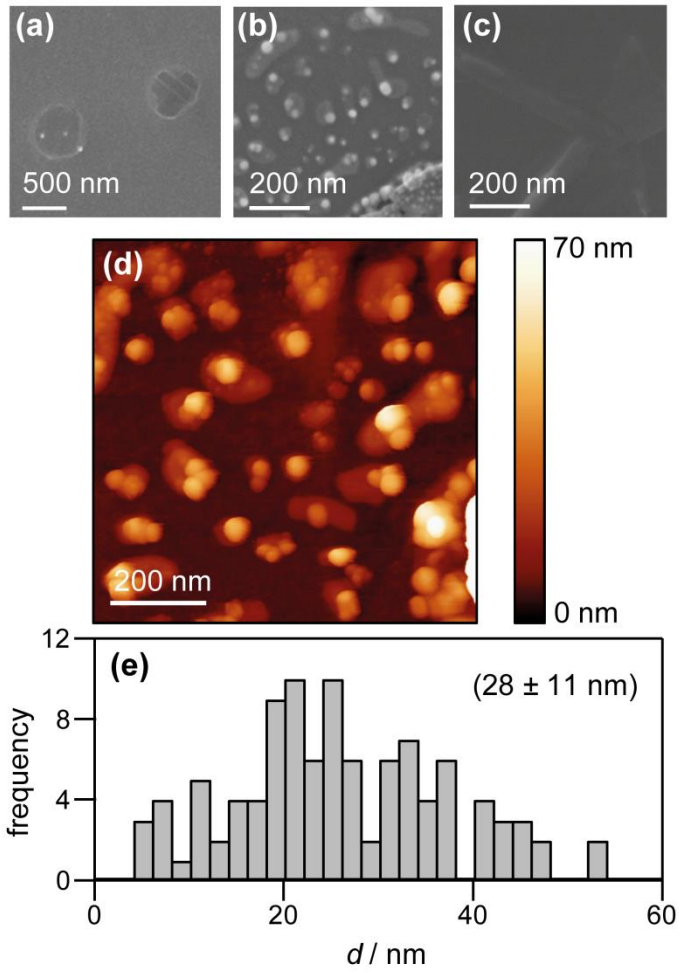

Figure 5-8. HOPG surface visualisation after electrodeposition. (a) FE-SEM image of two deposition spots. (b) FE-SEM image of a deposition spot after controlled breaking of the pipette. Some glass from the pipette is visible in the lower – right corner. (c) FE-SEM image of a controlled pipette breaking, without Ag deposition. (d) TM-AFM image of the same region as studied in (b). (e) Histogram of NP size obtained from the TM–AFM image in (d). The electrodeposition potential (for all data except (c)) was −50 mV.

Figure 5-8(a) shows an FE–SEM image of the HOPG substrate after electrodeposition experiments. Two spots are clearly visible where the electrolyte meniscus was brought into contact with the HOPG surface, and electrochemical measurements were made. These features further substantiate that the contact area is

comparable to the area of the pipette opening (*ca*. 400 nm diameter). Notably, even though the current-time traces associated with each of these spots showed the typical behaviour outlined above (*ca*. 100 – 150 discrete current events during the contact time of 1 s), only a few NPs can be observed. This is consistent with our proposed mechanism: NPs detach quickly after their formation and are transported into the bulk of the electrolyte solution in the pipette. By retracting the pipette after the deposition period, the electrolyte with the particles in solution is withdrawn from the surface, leaving a mostly clean surface.

To confirm NP formation, a small amount of electrolyte was forced from the pipette to the surface after an electrodeposition experiment by slightly lowering the pipette onto the HOPG surface, thereby leaving behind a minute drop of AgNP-containing electrolyte solution on the HOPG surface. Figure 5-8(b) shows a FE–SEM image of the NPs deposited this way, where part of a piece of glass from the pipette can be seen in the bottom-right corner. Comparing Figure 5-8(b) with Figure 5-8(a), it can clearly be seen that breaking the pipette leaves a large number of NPs of *ca*. 30 – 40 nm diameter on the surface. These findings clearly indicate a large number of NPs in the electrolyte solution in the pipette after an electrodeposition experiment. As these NPs are pristine (*i.e.* not capped by stabilising agents), and of controlled size, it is envisaged that this method could be exploited as an approach for NP synthesis. In addition, it may be possible to fine-tune the mean particle size by varying the Ag salt and the supporting electrolyte concentration, the substrate electrode, the temperature and the potential field across the electrolyte meniscus by applying a bias potential between the two QRCEs.

A pipette breaking control experiment was also performed, *i.e.* a pipette filled with just supporting electrolyte was forced onto the surface, to examine the tip contents

eliminating the effect of electrodeposition. The resulting surface is devoid of nanoparticles, although there are traces of salt. An enlarged view of the broken pipette on the surface is show is shown in Figure 5-9.

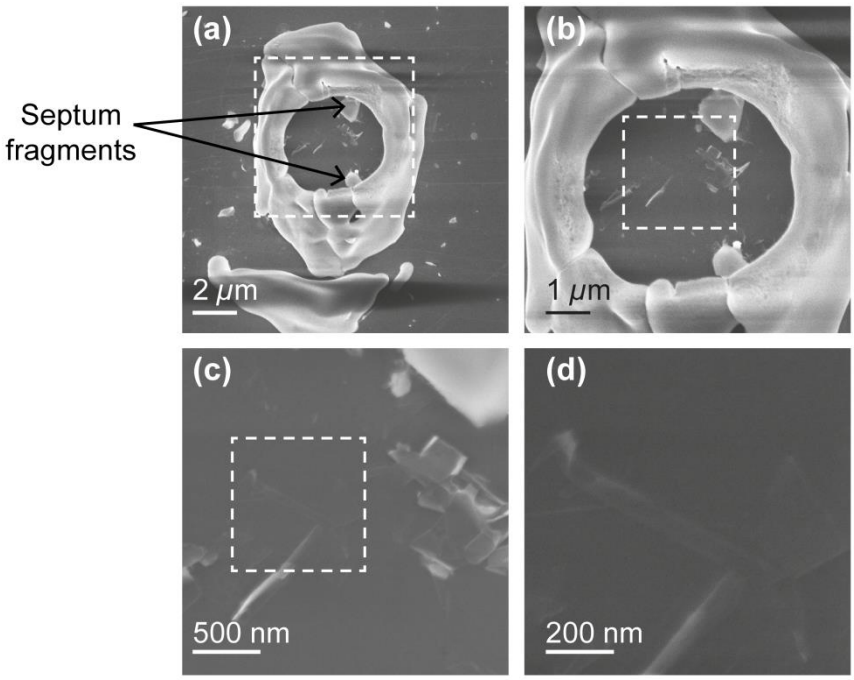

Figure 5-9. FE-SEM images of the site on HOPG of a controlled breaking of the pipette, which contained 50 mM KNO_3, at various magnifications. (a) The entire site of the broken pipette. (b) The central cavity of the tip. (c) The HOPG surface at the site of pipette breaking. (d) The surface, as depicted in Figure 5-8(c). Areas of successive magnification are highlighted in dotted lines. Note that there are some effects of insulating material (glass and salt) charging in (a) and (b). Also, fragments of the septum of the theta capillary are visible in (a) and (b).

The same area of the electrodeposition tip breaking was also investigated with TM-AFM with a Veeco Enviroscope AFM with Nanoscope IV controller. The resulting TM-AFM image is shown in Figure 5-8(d). While the background is somewhat noisy, possibly due to some salt residues from the electrolyte solution and carbon deposition from prior FE-SEM imaging, the NPs are clearly visible. In addition to

visualising the spatial distribution of NPs, TM-AFM also allowed for an analysis of the particle size distribution. A histogram of the NP heights is shown in Figure 5-8(e), which reveals a size distribution of 28 ± 11 nm, which appears consistent with the charge observed in Figure 5-6(c), for a few NPs.

It should however, be mentioned that this value is complicated by a number of issues. First, as discussed above, the background in the TM-AFM image is somewhat noisy, making it difficult to distinguish between smaller particles (< 10 nm) and background features. Consequently, the occurrence of NPs with a size below 10 nm is most likely overestimated, and the frequencies in the histogram for particles < 10 nm can be considered an upper limit. Furthermore, a closer inspection of Figure 5-8(b) and Figure 5-8(d) shows that the NPs are often agglomerated. This agglomeration is most likely induced by the drying of the electrolyte droplet. Naturally, agglomerates will have a larger apparent height, skewing the distribution towards larger NPs. Finally, some degree of Ostwald ripening can occur for the AgNPs in solution after they detach from the substrate,[37,78,79] facilitated by the presence of Ag ions in solution. This would further widen the size distribution. Although these factors complicate full quantitative comparison between the electrochemical results and the data from high-resolution microscopy, the important point is that the findings from electrochemical measurements and microscopy are wholly consistent with a nucleation-growth-detachment mechanism for multiple AgNPs on HOPG.

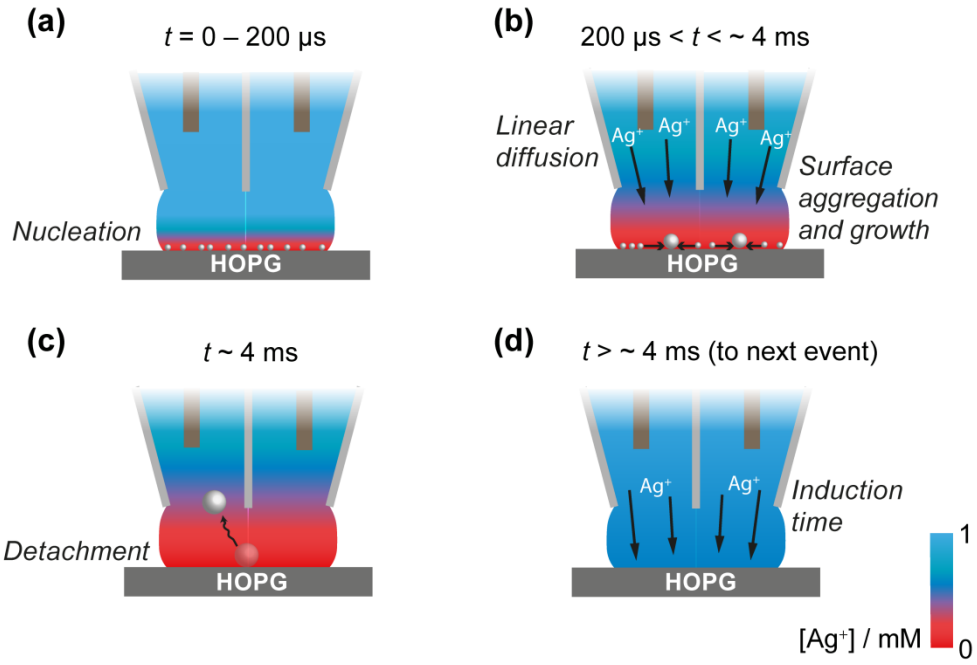

Figure 5-10. Schematic representation of the nucleation-growth-detachment mechanism, where *t* is the time. After the AgNPs nucleate (a), the growing NPs quickly consumes all of the Ag^+ in the electrolyte meniscus to reach a state where further growth of NPs is limited by diffusion of Ag^+ down the barrels of the pipette, during which time NPs can aggregate on the HOPG surface (b). This happens until the AgNPs reach a critical size/total charge and detach from the surface, shown here for a solitary particle at which time the surface concentration of Ag^+ is 0 mM (c). After detachment, the surface concentration of Ag^+ is replenished by diffusion down the barrels of the pipette (d), at which point the process can repeat with another nucleation event (a).

Based on these findings the time-dependency of the nucleation-growth-detachment mechanism for Ag electrodeposition on HOPG is summarized in Figure 5-10. Initially, many small critical nuclei are formed at the surface in a concatenated event (Figure 5-10(a)). As the nuclei form they rapidly (< 200 μs) achieve a diffusion controlled growth regime by consuming all of the Ag ions at the electrode surface (Figure 5-10(a)), and further growth of the NPs are limited by the quasi-linear

diffusion of Ag ions down barrels of the pipette into the electrolyte meniscus (Figure 5-10(b)), in agreement with the Cottrell analysis outlined above. At the surface, mobile Ag nuclei will aggregate into clusters in a process that lowers their surface tension (Figure 5-10(b)). This work supports the view that electrochemical deposition follows an aggregative growth, when considered on the nanoscale, as shown recently by Ustarroz *et al*.[80,81]

Finally, as the NPs reach a critical cluster size after 3 – 5 ms, and surface tension is sufficiently low, the particle(s) detach from the surface, where the surface concentration of Ag^+ ions is zero, and are transported into the electrolyte solution (Figure 5-10(c)).

Ag^+ ions need to diffuse back to the surface, where the surface concentration was previously zero, (Figure 5-10(d)) before the nucleation-growth-detachment cycle can restart (Figure 5-10(a)). This diffusion of Ag^+ ions results in the short induction time of *ca.* 4 ms (Figure 5-10(d)). Induction times for metal electrodeposition on (arrays of) nanoelectrodes are well known,[38,82] and may be related to the adsorption and lateral movement of a few individual Ag atoms on the surface to form a critical nucleus at each nucleation site for the next growth event.[47,83] The periodicity of the current-time features (Figure 5-6) strongly indicates that the induction time constant has a narrow distribution, and does not decrease markedly with increasing overpotential, in contrast to previous experimental and theoretical nucleation studies.[38,82] Histograms of induction times are shown in Figure 5-11.

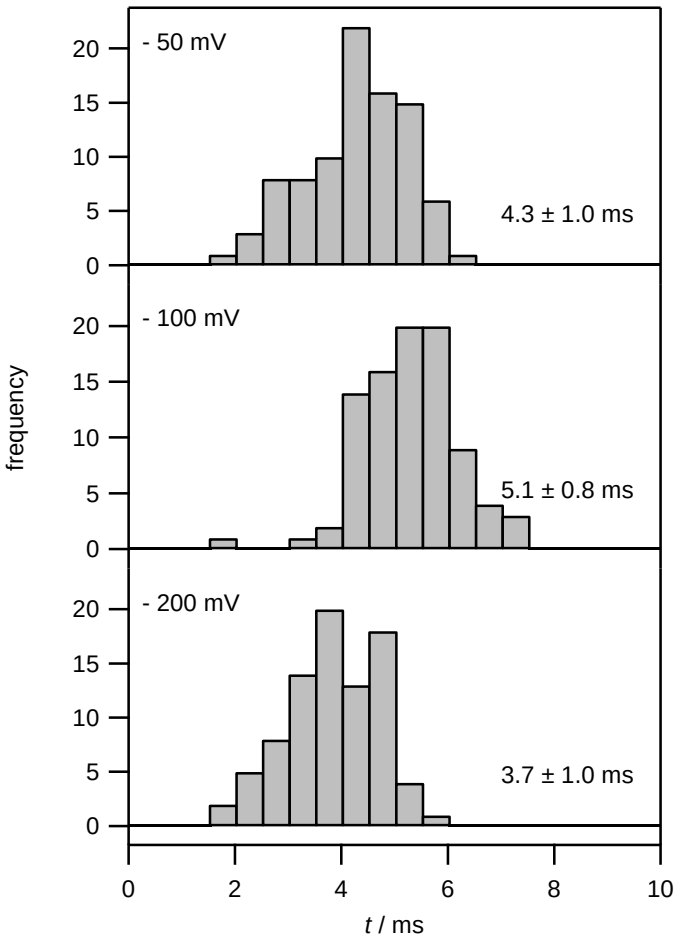

Figure 5-11. Histograms of induction times between distinct current events at the various electrodeposition potentials.

Two main contributing factors to the induction times need to be considered: first, there is the time associated with replenishing the electrolyte near the substrate with Ag^+. This time will depend on the degree of depletion of Ag^+, and thus the total charge, in the previous nucleation and growth event. For more negative (more driving) potentials, the total charge per event increases (see Figure 5-6), and consequently, the time required to replenish the electrolyte near the substrate is expected to increase. Second, there is a time constant associated with the adsorption of Ag^+ onto the substrate and for the formation of critical nuclei. More driving

potentials would be expected to favour this process. The weak potential-dependence of the total induction times is a consequence of these two opposing factors.

This can be explained by considering the time taken for Ag^+ ions to diffuse back to the surface from the pipette, a process that is independent of overpotential. The diffusional time, t_{diff}, follows the relationship

$$t_{diff} = \frac{(10a)^2}{D} \tag{5.4}$$

where 10*a* is an approximation of the diffusion layer thickness, *i.e.* 10 times the meniscus radius. The diffusional time, in this case the induction time, is 3 ms when *a* = 200 nm.

5.4 General discussion

The proposed nucleation-growth-detachment mechanism obviously merits some discussion, particularly in view of previous literature on metal (and, in particular, Ag) electrodeposition on HOPG (highlighted above and considered further herein). In most studies, it has often been suggested that the active sites for metal deposition are the step edges and that the atomically smooth basal plane needs to be activated (by some pre-treatment to introduce atomic scale defects)[29,47,84] for metal nucleation and deposition to occur. It should, however, be kept in mind that these findings are typically based on *ex situ* characterisation of the deposited particles, which can introduce additional artifacts due to sample preparation or characterisation techniques. For example, it has been shown that in scanning probe microscopy methods, such as AFM and scanning tunneling microscopy, NPs can be displaced or

dislodged by the probe.[44,85,86] Similarly, further sample preparation after electrodeposition experiments such as removing the electrolyte solution, rinsing the surface, and drying the surface can involve forces which are sufficient to overcome the weak metal – HOPG interaction and alter the NP size (due to agglomeration) and spatial distribution on the HOPG surface. As such, the finding that NPs are preferentially located at step edges from *ex situ* characterisation does not necessarily identify the active sites for metal nucleation and growth; instead, it indicates that step sites act as 'anchoring' sites for metal NPs, *i.e.* sites where the metal – substrate interaction is sufficiently strong for a NP to remain stuck, either due to geometric effects or local surface functionalities.

In this context, closer examination of some previous work reveals that significant electrodeposition of NPs can occur on the HOPG basal plane,[28,44,62,87-89] particularly where care was taken to minimise the lateral forces on the NPs during sample preparation and characterisation. Our findings that metal nucleation can occur readily on the HOPG basal plane, through both macroscale and microscale measurements, can be interpreted similarly. Here, each SECCM current event is associated with the formation and growth of a few AgNPs. Ag is known to be somewhat mobile on HOPG,[71,72] and as a result the growing NPs will move around on the HOPG surface until it hits an 'anchoring' site. The average density of metal nucleation sites on HOPG has been reported in the range of 10^6 – 10^{10} cm^{-2}, depending on the analysis performed.[29,44,45,62,73,87,88] As such, assuming the contact area is determined by the pipette diameter (*ca.* 400 nm), the number of point defects on the HOPG substrate would be very limited (and, interestingly, could be zero).[51,90-92] Given the size of the pipettes employed compared to the average step spacing of the HOPG substrate, the contacted region of the substrate would typically only

consist of the HOPG basal plane. Consequently, there is no 'anchoring' site for the AgNP, which keeps growing until the entropic gain of the NP being free in solution is greater than the interaction energy between the NP and the substrate, and the NP detaches from the surface and diffuses into the electrolyte solution. NP detachment due to an electric field between the pipette barrels can be ruled out, as no potential bias was applied between the QRCEs (Figure 2-8, as often used in SECCM,[77] and the supporting electrolyte concentration was high (50 mM). It is also interesting to note that the electrodeposition of metal nanoparticles,[93-96] and particularly Ag NPs,[74,97] occurs readily at liquid/liquid interfaces, often with little overpotential required. These are obviously defect free interfaces, and provide a precedent for aspects of the mechanism proposed herein.

The nucleation-growth-detachment mechanism also sheds light on the discrepancy between the observed behaviour of macroscopic Ag electrodeposition with the Scharifker-Hills model, which shows apparent intermediate behaviour between instantaneous and progressive nucleation and growth. Furthermore, at –100 mV applied potential, the number of nucleation sites predicted by the Scharifker-Hills model (10^5 – 10^6 cm^{-2}) is lower than the number of particles observed using SEM (10^7 cm^{-2}) and AFM (10^8 – 10^9 cm^{-2}). The SEM analysis counted particles over 100 nm, whilst the AFM images counted particles smaller than this, over around 3 nm. Both observations are consistent with and can be rationalized by the proposed nucleation-growth-detachment mechanism. As electrodeposition is initiated, nucleation and growth will occur at each nucleation site. The formed NPs are mobile due to the weak interaction between Ag and HOPG. As the nucleation sites are freed up due to the NPs mobility, further nucleation can occur, leading to a single nucleation site producing many NPs. The NP mobility encourages electrochemical

aggregative growth, as shown by Ustarroz *et al.*[80,81] This work on aggregative growth, together with our results on macroscopic nucleation, complements the nucleation-growth-detachment mechanism proposed for SECCM, considering that the Scharifker-Hills analysis is, in this case, too simplistic to take the detachment events into account. A significant point about the size and geometry of the SECCM meniscus setup is that the particles are encouraged to detach from the surface, since the contact area is so small that particles cannot grow too large and the barrels provide a route of exodus for mobile particles that break away from the weak surface interaction.

A further indication for the detachment of the NPs directly after growth (rather than, for example, when retracting the pipette) is the total number of current events. As shown in Figure 5-6, the number of current events, and thus the minimum number of NPs formed during 1 s is *ca.* 100 – 150. Experiments carried out over longer times showed that current events were maintained over the course of (at least) several minutes (see Figure 5-12). With an average NP diameter of 30 nm, there would simply not be enough space on the contacted area of the substrate (*ca*. 400 nm diameter) to accommodate all of the NPs formed if the NPs remained on the surface.

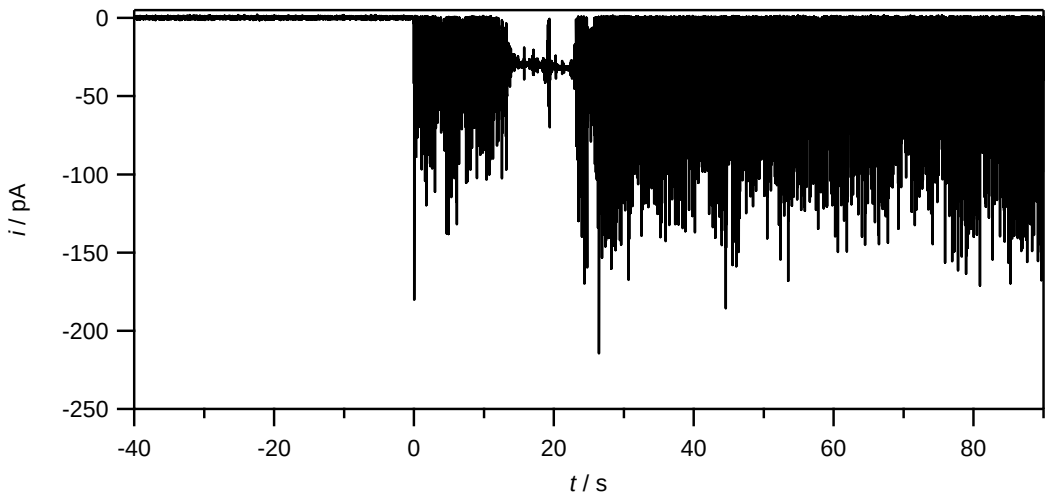

Figure 5-12. Extended current-time trace for the electrodeposition of Ag (from 1 mM $AgNO_3$ in 50 mM KNO_3) on HOPG at −200 mV.

No electrodeposition takes place before t = 0 s as the electrolyte droplet is not in contact with the substrate. Here, one data point was collected every 6.4 ms (average of 256 measurements every 25 μs) to limit the total amount of data collected over the longer time period. As a consequence, the time per data point here is comparable to the total length of one nucleation-growth-detachment cycle. Thus, the lack of observable individual events between 15 and 25 s is due to the convolution of individual events. Indeed, the response in this period can be compared to current-time traces which would be obtained in conventional electrodeposition studies employing extended electrode areas at moderate data collection rates, in which many individual events would show temporal overlap, and only an average continuous current can be observed.

5.5 Conclusions

In conclusion, it has been demonstrated with an SECCM-based approach that Ag electronucleation and growth on HOPG at the nanoscale is a stochastic process. In particular, owing to the timescale and length scale of SECCM, the HOPG basal plane has been probed in isolation of HOPG step edges with current-time measurements, allowing us to resolve the nucleation and growth of NPs on the HOPG basal plane. Interestingly, it was found that electrodeposition of Ag on HOPG follows a nucleation-growth-detachment mechanism. This finding is further supported by macroscale measurements, which show a disparity between the number of calculated nucleation sites (events) from chronoamperometry, and the observed number of particles, as well as transients which cannot be described satisfactorily with either instantaneous or progressive nucleation and growth models. The macroscale and nanoscale techniques probe different parts of the HOPG surface and it was shown that step edge sites did not contribute significantly to the number nucleation events and that the basal plane was the location for the majority of nucleation events.

Interestingly, under the experimental conditions employed, the AgNPs grow to *ca*. 30 nm before detaching from the surface and diffusing into the solution in the SECCM setup. The nucleation-growth-detachment model has been further corroborated by high resolution microscopy. In addition to opening up new prospects for the study of individual NP electrodeposition, the studies herein reveal key features and a model that sheds new light on the understanding of the metal electrodeposition process on carbon electrodes in general.

5.6 References

(1) Sun, C. Q.; Tay, B. K.; Zeng, X. T.; Li, S.; Chen, T. P.; Zhou, J.; Bai, H. L.; Jiang, E. Y. *J. Phys.: Condens. Matter* **2002**, *14*, 7781.

(2) Zanchet, D.; Tolentino, H.; Martins Alves, M. C.; Alves, O. L.; Ugarte, D. *Chem. Phys. Lett.* **2000**, *323*, 167.

(3) Li, H.; Han, P. D.; Zhang, X. B.; Li, M. *Mater. Chem. Phys.* **2013**, *137*, 1007.

(4) Haruta, M. *Chem. Rec.* **2003**, *3*, 75.

(5) Koper, M. T. M. *Nanoscale* **2011**, *3*, 2054.

(6) Li, Y.; Boone, E.; El-Sayed, M. A. *Langmuir* **2002**, *18*, 4921.

(7) Link, S.; El-Sayed, M. A. *J. Phys. Chem. B* **1999**, *103*, 4212.

(8) Fu, H. B.; Yao, J. N. *J. Am. Chem. Soc.* **2001**, *123*, 1434.

(9) Hernández-Santos, D.; González-García, M. B.; García, A. C. *Electroanalysis* **2002**, *14*, 1225.

(10) Anker, J. N.; Hall, W. P.; Lyandres, O.; Shah, N. C.; Zhao, J.; Van Duyne, R. P. *Nat. Mater.* **2008**, *7*, 442.

(11) Nie, S. M.; Emery, S. R. *Science* **1997**, *275*, 1102.

(12) Kneipp, K.; Kneipp, H.; Itzkan, I.; Dasari, R. R.; Feld, M. S. *Chem. Rev.* **1999**, *99*, 2957.

(13) Bard, A. J. *J. Am. Chem. Soc.* **2010**, *132*, 7559.

(14) Arvia, A. J.; Salvarezza, R. C.; Triaca, W. E. *J. New Mat. Electrochem. Syst.* **2004**, *7*, 133.

(15) Kitsomboonloha, R.; Ngambenjawong, C.; Mohammed, W. S.; Chaudhari, M. B.; Hornyak, G. L.; Dutta, J. *Micro Nano Lett.* **2011**, *6*, 342.

(16) Pankhurst, Q. A.; Connolly, J.; Jones, S. K.; Dobson, J. *J. Phys. D: Appl. Phys.* **2003**, *36*, R167.

(17) Moghimi, S. M.; Hunter, A. C.; Murray, J. C. *Pharmacol. Rev.* **2001**, *53*, 283.

(18) Chithrani, B. D.; Ghazani, A. A.; Chan, W. C. W. *Nano Lett.* **2006**, *6*, 662.

(19) Lokina, S.; Stephen, A.; Kaviyarasan, V.; Arulvasu, C.; Narayanan, V. *Eur. J. Med. Chem.* **2014**, *76*, 256.

(20) Prabhu, S.; Poulose, E. *Int Nano Lett* **2012**, *2*, 1.

(21) Masuda, H.; Yasui, K.; Nishio, K. *Adv. Mater.* **2000**, *12*, 1031.

(22) Howells, A. R.; Hung, L.; Chottiner, G. S.; Scherson, D. A. *Solid State Ionics* **2002**, *150*, 53.

(23) Yeung, K. L.; Wolf, E. E. *J. Vac. Sci. Technol. A-Vac. Surf. Films* **1992**, *10*, 651.

(24) Henry, C. R. *Surf. Sci. Rep.* **1998**, *31*, 235.

(25) Haynes, C. L.; Van Duyne, R. P. *J. Phys. Chem. B* **2001**, *105*, 5599.

(26) Turkevich, J.; Stevenson, P. C.; Hillier, J. *Discuss. Faraday Soc.* **1951**, *11*, 55.

(27) Brust, M.; Walker, M.; Bethell, D.; Schiffrin, D. J.; Whyman, R. *J. Chem. Soc., Chem. Commun.* **1994**, 801.

(28) Penner, R. M. *J. Phys. Chem. B* **2002**, *106*, 3339.

(29) Bayati, M.; Abad, J. M.; Nichols, R. J.; Schiffrin, D. J. *J. Phys. Chem. C* **2010**, *114*, 18439.

(30) Scharifker, B.; Hills, G. *Electrochim. Acta* **1983**, *28*, 879.

(31) Tian, N.; Zhou, Z.-Y.; Sun, S.-G.; Ding, Y.; Wang, Z. L. *Science* **2007**, *316*, 732.

(32) Gunawardena, G.; Hills, G.; Montenegro, I.; Scharifker, B. *J. Electroanal. Chem.* **1982**, *138*, 225.

(33) Hills, G.; Pour, A. K.; Scharifker, B. *Electrochim. Acta* **1983**, *28*, 891.

(34) Gunawardena, G.; Hills, G.; Montenegro, I.; Scharifker, B. *J. Electroanal. Chem.* **1982**, *138*, 255.

(35) Garcia-Pastoriza, E.; Mostany, J.; Scharifker, B. R. *J. Electroanal. Chem.* **1998**, *441*, 13.

(36) Dudin, P. V.; Unwin, P. R.; Macpherson, J. V. *J. Phys. Chem. C* **2010**, *114*, 13241.

(37) Redmond, P. L.; Hallock, A. J.; Brus, L. E. *Nano Lett.* **2004**, *5*, 131.

(38) Chen, S.; Kucernak, A. *J. Phys. Chem. B* **2003**, *107*, 8392.

(39) Tel-Vered, R.; Bard, A. J. *J. Phys. Chem. B* **2006**, *110*, 25279.

(40) Velmurugan, J.; Noël, J.-M.; Nogala, W.; Mirkin, M. V. *Chemical Science* **2012**, *3*, 3307.

(41) Cox, J. T.; Zhang, B. *Annu. Rev. Anal. Chem.* **2012**, *5*, 253.

(42) Ebejer, N.; Schnippering, M.; Colburn, A. W.; Edwards, M. A.; Unwin, P. R. *Anal. Chem.* **2010**, *82*, 9141.

(43) Ebejer, N.; Güell, A. G.; Lai, S. C. S.; McKelvey, K.; Snowden, M. E.; Unwin, P. R. *Annu. Rev. Anal. Chem.* **2013**, *6*, 329.

(44) Zoval, J. V.; Stiger, R. M.; Biernacki, P. R.; Penner, R. M. *J. Phys. Chem.* **1996**, *100*, 837.

(45) Miranda-Hernandez, M.; Gonzalez, I.; Batina, N. *J. Phys. Chem. B* **2001**, *105*, 4214.

(46) Porter, J. D.; Robinson, T. O. *J. Phys. Chem.* **1993**, *97*, 6696.

(47) Pötzschke, R. T.; Gervasi, C. A.; Vinzelberg, S.; Staikov, G.; Lorenz, W. J. *Electrochim. Acta* **1995**, *40*, 1469.

(48) McCreery, R. L.; McDermott, M. T. *Anal. Chem.* **2012**, *84*, 2602.

(49) Desai, D.; Turney, D. E.; Anantharaman, B.; Steingart, D. A.; Banerjee, S. *J. Phys. Chem. C* **2014**, *118*, 8656.

(50) Endres, F.; Freyland, W.; Gilbert, B. *Ber. Bunsen-Ges.* **1997**, *101*, 1075.

(51) Boxley, C. J.; White, H. S.; Lister, T. E.; Pinhero, P. J. *J. Phys. Chem. B* **2002**, *107*, 451.

(52) Williams, C. G.; Edwards, M. A.; Colley, A. L.; Macpherson, J. V.; Unwin, P. R. *Anal. Chem.* **2009**, *81*, 2486.

(53) Lai, S. C. S.; Patel, A. N.; McKelvey, K.; Unwin, P. R. *Angew. Chem., Int. Ed.* **2012**, *51*, 5405.

(54) Patel, A. N.; Collignon, M. G.; O'Connell, M. A.; Hung, W. O. Y.; McKelvey, K.; Macpherson, J. V.; Unwin, P. R. *J. Am. Chem. Soc.* **2012**, *134*, 20117.

(55) Anne, A.; Cambril, E.; Chovin, A.; Demaille, C.; Goyer, C. *ACS Nano* **2009**, *3*, 2927.

(56) Lhenry, S.; Leroux, Y. R.; Hapiot, P. *Anal. Chem.* **2012**, *84*, 7518.

(57) Kirkman, P. M.; Güell, A. G.; Cuharuc, A. S.; Unwin, P. R. *J. Am. Chem. Soc.* **2014**, *136*, 36.

(58) Patel, A. N.; Tan, S.-y.; Miller, T. S.; Macpherson, J. V.; Unwin, P. R. *Anal. Chem.* **2013**, *85*, 11755.

(59) Patel, A. N.; McKelvey, K.; Unwin, P. R. *J. Am. Chem. Soc.* **2012**, *134*, 20246.

(60) Edwards, M. A.; Bertoncello, P.; Unwin, P. R. *J. Phys. Chem. C* **2009**, *113*, 9218.

(61) Lee, C.-Y.; Guo, S.-X.; Bond, A. M.; Oldham, K. B. *J. Electroanal. Chem.* **2008**, *615*, 1.

(62) Gloaguen, F.; Leger, J. M.; Lamy, C.; Marmann, A.; Stimming, U.; Vogel, R. *Electrochim. Acta* **1999**, *44*, 1805.

(63) Walter, E. C.; Murray, B. J.; Favier, F.; Kaltenpoth, G.; Grunze, M.; Penner, R. M. *J. Phys. Chem. B* **2002**, *106*, 11407.

(64) Walter, E. C.; Zach, M. P.; Favier, F.; Murray, B. J.; Inazu, K.; Hemminger, J. C.; Penner, R. M. *ChemPhysChem* **2003**, *4*, 131.

(65) Favier, F.; Walter, E. C.; Zach, M. P.; Benter, T.; Penner, R. M. *Science* **2001**, *293*, 2227.

(66) Vazquez, L.; Hernandez Creus, A.; Carro, P.; Ocon, P.; Herrasti, P.; Palacio, C.; Vara, J. M.; Salvarezza, R. C.; Arvia, A. J. *J. Phys. Chem.* **1992**, *96*, 10454.

(67) Tsakova, V.; Milchev, A. *J. Electroanal. Chem.* **1987**, *235*, 237.

(68) Lu, G.; Zangari, G. *J. Phys. Chem. B* **2005**, *109*, 7998.

(69) Hula, R. C.; Edtmaier, C.; Holzweber, M.; Hutter, H.; Eisenmenger-Sittner, C. *Appl. Surf. Sci.* **2010**, *256*, 4697.

(70) He, Y.; Zhang, J. Y.; Wang, Y.; Yu, Z. P. *Appl. Phys. Lett.* **2010**, *96*, 063108.

(71) Goldby, I. M.; Kuipers, L.; von Issendorff, B.; Palmer, R. E. *Appl. Phys. Lett.* **1996**, *69*, 2819.

(72) Couillard, M.; Pratontep, S.; Palmer, R. E. *Appl. Phys. Lett.* **2003**, *82*, 2595.

(73) Liu, H.; Favier, F.; Ng, K.; Zach, M. P.; Penner, R. M. *Electrochim. Acta* **2001**, *47*, 671.

(74) Guo, J.; Tokimoto, T.; Othman, R.; Unwin, P. R. *Electrochem. Commun.* **2003**, *5*, 1005.

(75) Johnston, R. R. M.; Spiro, M. *J. Phys. Chem.* **1967**, *71*, 3784.

(76) Bard, A. J.; Faulkner, L. R. *Electrochemical Methods: Fundamentals and Applications, 2nd Edition* **2001**.

(77) Snowden, M. E.; Güell, A. G.; Lai, S. C. S.; McKelvey, K.; Ebejer, N.; O'Connell, M. A.; Colburn, A. W.; Unwin, P. R. *Anal. Chem.* **2012**, *84*, 2483.

(78) Silvert, P. Y.; HerreraUrbina, R.; Duvauchelle, N.; Vijayakrishnan, V.; Elhsissen, K. T. *J. Mater. Chem.* **1996**, *6*, 573.

(79) Bastus, N. G.; Comenge, J.; Puntes, V. *Langmuir* **2011**, *27*, 11098.

(80) Ustarroz, J.; Ke, X.; Hubin, A.; Bals, S.; Terryn, H. *J. Phys. Chem. C* **2011**, *116*, 2322.

(81) Ustarroz, J.; Hammons, J. A.; Altantzis, T.; Hubin, A.; Bals, S.; Terryn, H. *J. Am. Chem. Soc.* **2013**, *135*, 11550.

(82) Quinn, B. M.; Lemay, S. G. *Adv. Mater.* **2006**, *18*, 855.

(83) Ustarroz, J.; Gupta, U.; Hubin, A.; Bals, S.; Terryn, H. *Electrochem. Commun.* **2010**, *12*, 1706

(84) Hendricks, S. A.; Kim, Y. T.; Bard, A. J. *J. Electrochem. Soc.* **1992**, *139*, 2818.

(85) Schaefer, D. M.; Patil, A.; Andres, R. P.; Reifenberger, R. *Appl. Phys. Lett.* **1993**, *63*, 1492.

(86) Schaefer, D. M.; Ramachandra, A.; Andres, R. P.; Reifenberger, R. *Z Phys D - Atoms, Molecules and Clusters* **1993**, *26*, 249.

(87) Patten, H. V.; Ventosa, E.; Colina, A.; Ruiz, V.; López-Palacios, J.; Wain, A. J.; Lai, S. C. S.; Macpherson, J. V.; Unwin, P. R. *J. Solid State Electrochem.* **2011**, *15*, 2331.

(88) Gimeno, Y.; Creus, A. H.; Carro, P.; Gonzalez, S.; Salvarezza, R. C.; Arvia, A. J. *J. Phys. Chem. B* **2002**, *106*, 4232.

(89) Brülle, T.; Stimming, U. *J. Electroanal. Chem.* **2009**, *636*, 10.

(90) Obeng, Y. S.; Bard, A. J. *J. Am. Chem. Soc.* **1991**, *113*, 6279.

(91) Ma, H.; Lee, L.; Brooksby, P. A.; Brown, S. A.; Fraser, S. J.; Gordon, K. C.; Leroux, Y. R.; Hapiot, P.; Downard, A. J. *J. Phys. Chem. C* **2014**, *118*, 5820.

(92) Stevenson, K. J.; Veneman, P. A.; Gearba, R. I.; Mueller, K. M.; Holliday, B. J.; Ohta, T.; Chan, C. K. *Faraday Discuss.* **2014**.

(93) Izquierdo, D.; Martinez, A.; Heras, A.; Lopez-Palacios, J.; Ruiz, V.; Dryfe, R. A. W.; Colina, A. *Anal. Chem.* **2012**, *84*, 5723.

(94) Uehara, A.; Hashimoto, T.; Dryfe, R. A. W. *Electrochim. Acta* **2014**, *118*, 26.

(95) Johans, C.; Kontturi, K.; Schiffrin, D. J. *J. Electroanal. Chem.* **2002**, *526*, 29.

(96) Grunder, Y.; Ho, H. L. T.; Mosselmans, J. F. W.; Schroeder, S. L. M.; Dryfe, R. A. W. *Phys. Chem. Chem. Phys.* **2011**, *13*, 15681.

(97) Li, F.; Edwards, M.; Guo, J.; Unwin, P. R. *J. Phys. Chem. C* **2009**, *113*, 3553.

6 Impact of Surface Parasitic Processes on Quinone Electron Transfer Kinetics

The electrochemical reductions of quinone derivatives (*para*-benzoquinone (*p*-BQ), anthraquinone (AQ) and 2-(*p*-tolysulfinyl)cyclohexane-2,5-diene-1,4-dione) were studied using a gold and a carbon fibre ultramicroelectrode, to probe the electron transfer kinetics in acetonitrile. Such reactions are well studied, but it is shown herein that there are difficulties associated with obtaining reliable voltammetric measurements, since these electrodes undergo surface fouling processes for quinone species. This makes reliable determination of the standard rate constant quite challenging, and it is shown that subtle changes to experimental conditions such as analyte concentration and potential scan rate alter the amount of fouling, thus changing the apparent rate constant. Scanning the potential faster can reduce the extent of fouling, but this results in non-steady-state current measurements during cyclic voltammetry, so numerical modelling is required to extract meaningful kinetic data about the reaction. The difficulties of working with quinones in non-aqueous media are highlighted, with particular focus on methods to overcome the issue of electrode fouling. Our data are compared with other recent data in the literature regarding the adiabaticity of quinone reactions.

6.1 Introduction

The redox mechanisms of quinones have become the main focus of different research fields such as organic chemistry, electrochemistry and biochemistry. Special interest in aqueous electrochemistry of quinones arises from their role as a strong electron acceptor and a mediator of electron transfer (ET) in important biological processes such as respiration and photosynthesis.[1] As such, considerable attention has been directed to both aqueous[2,3] and non-aqueous[4,5] redox processes of quinones. Quinone moieties that undergo reversible redox reactions have been employed as anode active materials for rechargeable polymer-air batteries[6] and electrolyte active materials for supercapacitors.[7] Determination of heterogeneous ET rate constants for quinones plays a critical role in terms of device energy efficiency. Therefore, kinetic studies in aprotic media give valuable information about the stability and energetics of semiquinones, since these radicalic intermediates are formed and stabilised in non-aqueous media.

In aqueous media, quinones exhibit reversible two-electron two-proton transfer in the presence of a suitable proton donor-acceptor in which the reduction potential varies with pH, in a Nernstian manner.[8] On the other hand, in aprotic media, quinone derivatives usually undergo two one-electron reductions; first the formation of the radical anion and then the dianion at more negative potentials:[9,10]

$$Q + e^- \underset{k_b}{\overset{k_f}{\rightleftharpoons}} Q^{\bullet -} \qquad (6.1)$$

$$Q^{\bullet -} + e^- \underset{k_b}{\overset{k_f}{\rightleftharpoons}} Q^{2-} \qquad (6.2)$$

where Q and $Q^{\bullet -}$ represent the quinone and semiquinone (radical anion) species, respectively.

Reduction of quinone species is best described as a heterogeneous outer sphere ET mechanism[11] (see Section 1.1.3). For this type of process, the net rate of transformation depends on the potential-dependent rate constants of both the forward/reduction (k_f) and reverse/oxidation (k_b) processes. In this work, a comparative ET kinetic study for a series of quinones at a gold (Au) and carbon fibre (CF) ultramicroelectrodes (UME) is presented by measuring kinetic parameters of a quasi-reversible quinone to semiquinone transformation.

The experimental measurement of the standard rate constant (k^0) is challenging, with several different techniques used and many discrepancies in the reported literature values. Table 6-1 is a striking illustration of the range of reported experimentally measured k^0 values for quinones, even for the same compound on the same electrode material. Reported k^0 values are usually smaller than the true value due to a series of experimental factors, such as solution resistance, and these can lead to significant errors in reported values.[12] UMEs appear highly advantageous for eliminating such errors in voltammetry, and considerably higher rate constants are reported by employing UMEs[13] and nanoelectrodes.[14]

Table 6-1. Comparison of literature standard rate constants values for different quinones in aprotic electrolytes.

Ref.	Electrolyte	Electrode	k^0 / cm s^{-1}		
			***p*-BQ**	**AQ**	**NQ‡**
15	MeCN/TBAP§	Pt band 40.5 μm	0.13	0.097	0.1
16	[C_2mim][NTF_2] *	Au 10 μm microdisk	$\geq$ 0.03	-	-
17	MeCN/TBAP	Au 10 μm microdisk	0.051	0.19	-
17	MeCN/TBAP	CF 10 μm microdisk	0.067	0.45	-
18	MeCN/TEAB¶	Pt macro	0.63	0.92	0.83
18	MeCN/TEAB	Au macro	0.66	0.83	0.71
18	MeCN/TEAB	Graphite macro	0.45	0.56	0.51
19	DMF†/TBAP	Au macro	0.065	0.018	0.023
20	DMF/TEAB	Au macro	0.0053	-	-
21	DMF/TEAB	Au/Hg macro	0.18	0.23	0.35

* [C_2mim][NTF_2] = 1-ethyl-3-methyl-imidazolium bis(trifluoromethylsulfonyl)imide
† DMF = dimethylformamide
‡ NQ = naphthaquinone,
§ TBAP = tetrabutylammonium phosphate,
¶ TEAB = tetraethylammonium bromide

The heterogeneous ET rate constants for the reduction of quinones under steady-state conditions have been experimentally determined for microscale electrodes in Table 6-1.[15-17,19] Standard heterogeneous charge-transfer rate constants, for macroscale electrodes in Table 6-1,[18-21] were evaluated from the observed differences in current peak potentials,

$$\Delta E_{\mathrm{p}} = E_{\mathrm{cp}} - E_{\mathrm{ap}} \tag{6.3}$$

where E_{ap} and E_{cp} are the anodic and cathodic peak potentials, respectively. This value is used in the relationship given by Nicholson[22]

$$k^0 = \pi^{1/2} D^{1/2} \left(nF / RT\right)^{1/2} \gamma^{-\alpha} \nu^{1/2} \Psi\left(\Delta E\right) \quad (6.4)$$

where $n = 1$ for a single electron reduction of the quinone, and

$$\gamma = \frac{D_O}{D_R} \quad (6.5)$$

where D_O and D_R are diffusion coefficients for reactant (oxidised) and product (reduced) species, respectively, α is the transfer coefficient, v is the potential scan rate and $\Psi(\Delta E)$ is a parameter which is evaluated from a reference curve of $\Psi(\Delta E)$ *vs*. ΔE:

$$\Psi\left(E\right) = i / FAc^* D_O^{1/2} \left(nF / RT\right)^{1/2} \nu^{1/2} \quad (6.6)$$

where i is current, A is area and c^* is bulk concentration.

Au and CF are common electrode materials due to their unique properties. The former is an inert and very stable noble metal and the latter serves for a broad range of applications because of its wide potential window, low background currents, rich surface chemistry, chemical inertness and low cost.[23] The k^0 values of a small group of quinones will be measured at these electrodes.

SECM is a scanning probe technique which emerged as a useful tool for studying structures and processes on the micrometre and submicrometre scale. Since its inception, it has been widely used to probe a variety of electrochemical processes due to its high spatial resolution for both quantitative and qualitative investigations.[24] The electrochemical response provides information on local properties such as

topography or reactivity.[25] Here, SECM was used in the feedback mode, using positive feedback towards a biased (0.0 V) Au substrate to measure quinone kinetics. In this mode, depicted in Figure 6-1 for a reduction reaction at the ultramicroelectrode (UME), when the tip is placed close to the conductive substrate surface the reduced species (R) formed at the UME can diffuse to the substrate where it is oxidised, resulting in an additional flux of oxidised species (O) to the tip *i.e.* positive feedback.

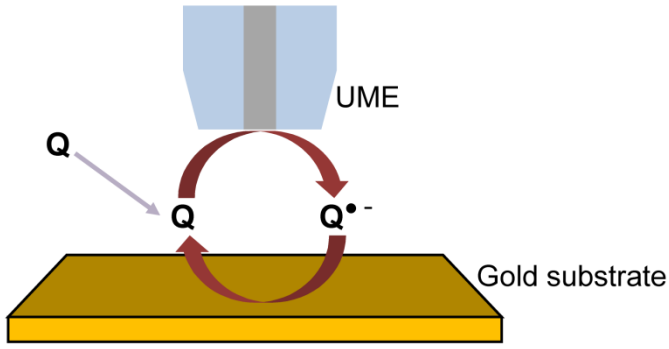

Figure 6-1. A schematic for SECM in feedback mode showing a quinone, Q, reduced at the tip to a semiquinone, $Q^{\bullet -}$.

An SECM approach curve is performed by translating the tip normal to the surface, whilst applying a potential to the tip that gives a steady-state limiting current. As the tip gets within a few electrode radii from the surface, feedback effects of the substrate are observed. If the electrode fouls during the approach, or the activity of the substrate is not known, there is not a reliable way to determine tip-substrate distance. Here, non-electrochemical tip-positioning method was used to place the electrode close to the surface. The tip was oscillated in the *z*-direction, and the amplitude of this oscillation is damped as the tip makes intermittent contact (IC) with the surface. Since this technique, IC-SECM (Chapters 3 and 4),[26] relies on

physical contact between the tip and substrate, the approach can be performed without applying a potential to the tip, thus preventing tip fouling whilst the tip is positioned at a well-defined distance to the substrate.[27]

SECM is a highly advantageous technique for studying fast heterogeneous ET kinetics since mass-transport of electroactive species significantly increases when the tip approaches close enough to the substrate surface. The use of SECM also eliminates some common experimental errors such as the solution ohmic drop.[28]

In this study, ET kinetics were probed for a family of quinone derivatives: *p*-benzoquinone (*p*-BQ); naphthaquinone (NQ); anthraquinone (AQ) and 2-(*p*-tolysulfinyl)cyclohexane-2,5-diene-1,4-dione in two different optical isomeric forms (enantiomer(-) (E-), enantiomer(+) (E+) and racemic(+/-) mixture (R)), and their molecular structures are displayed in Figure 2-10. As stated in Chapter 2, 2-(*p*-tolysulfinyl)cyclohexane-2,5-diene-1,4-dione) was synthesised in Departamento de Química Orgánica, Universidad Autónoma de Madrid, and sent for analysis courtesy of Dr. Raúl Díaz. This was done on CF and Au UMEs, by measuring CVs using SECM operated in the feedback mode and CV at an increased scan rate. Here, the surface blocking processes of quinone electrochemistry at different electrode materials and their influence on measured kinetics are explained. Our studies serve as the first on the electrode fouling processes during quinone reduction in aprotic media. The compounds were chosen on the basis of comparing kinetic parameters of well-studied quinones with previously reported literature values.

6.2 Results and discussion

6.2.1 Cyclic voltammetry of compounds

Diffusion coefficients were estimated by cyclic voltammetry performed at different scan rates with a glassy carbon (GC) (3 mm diameter) disk electrode as a working electrode, platinum wire as a counter electrode and silver wire as a reference electrode with 3 mM analyte concentration in acetonitrile/$TBAPF_6$ solution. As the response was close to reversible (*vide infra*), the Randles-Sevcik equation (Equation (1.13)) was employed in order to calculate the diffusion coefficients. The experimentally (macroscopic measurement on GC) determined diffusion coefficients in acetonitrile (0.1 M $TBAPF_6$) are presented in Table 6-2, along with the expected steady-state limiting currents at each electrode studied (measurement on Au and CF UMEs).

Table 6-2. Measured diffusion coefficients for each compound used, and the expected diffusion limited steady-state currents for the Au and CF electrodes used, in acetonitrile (0.1 M $TBAPF_6$).

	Macroscopic (on GC)	***Microscopic (on UMEs)***			
Compound	***D*** **/ cm^2 s^{-1}**	**i_{lim} / nA**			
		Au, *a* = 12.5 *μ*m		**CF, *a* = 3.5 *μ*m**	
		***c* = 0.2 mM**	***c* = 2 mM**	***c* = 0.2 mM**	***c* = 2 mM**
Ferrocene*	2.43×10^{-5}	2.34	23.4	0.66	6.56
***p*-BQ**	2.68×10^{-5}	2.58	25.8	0.72	7.23
AQ	2.15×10^{-5}	2.07	20.7	0.58	5.81
R / E^+ / E^-	1.42×10^{-5}	1.37	13.7	0.38	3.84

*Diffusion coefficient for ferrocene taken from literature Ref.[29]

The purity of compounds used was also verified using proton nuclear magnetic resonance (^{1}H NMR) spectroscopy in trideuteroacetonitrile (CD_3CN). In cases where the compound was not found to be pure, a recrystallisation was carried out.

6.2.2 Electrode surface blocking processes and effect of concentration

The kinetic properties of a quasi-reversible electrochemical reduction of semiquinone radical formation were studied. Our generic reaction describes the transformation of a quinone unit to a radicalic species in aprotic media. Although strong adsorption has been described, it is more likely in aqueous than aprotic media.[30] Strong electrode fouling was observed for almost all compounds in acetonitrile media. Different degrees of surface fouling were observed depending both on the electrode material and the compound studied.

Preliminary experiments on the Au electrode were performed in a 2 mM quinone concentration solution, at which electrode surface fouling was observed upon repetitive cycling, as shown in Figure 6-2(a) for *p*-BQ. Figure 6-2(b) demonstrates how significant surface blockage was eliminated for the Au electrode simply by decreasing the concentration of active species from 2 mM to 0.2 mM. The lower concentration means that the flux of quinone species to the electrode is lower, decreasing passivation of the surface during the course of the measurement.

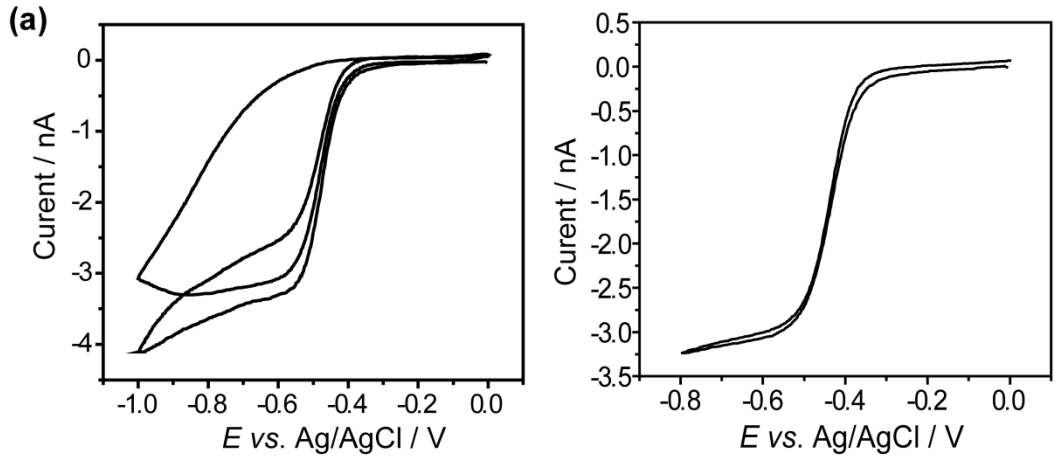

Figure 6-2. Two consecutive cyclic voltammograms of 2 mM (a) and 0.2 mM (b) of *p*-BQ solutions in acetonitrile (0.1 M $TBAPF_6$), on a 25 μm diameter Au UME at 25 mV s^{-1}.

In the case of the CF electrode, electrochemical analysis was found to be very challenging because of the strong adsorption of quinone molecules and/or intermediates to the electrode surface. Only the forward scans, and only the first scan, of voltammetric analyses (*i.e.* LSVs) were shown in reported measurements by Compton *et al*. at Au and CF UMEs, in which fouling cannot be observed effectively.[17]

A typical example of a voltammetric response is represented in Figure 6-2 for AQ at two different concentrations. Electrode fouling clearly appears during the first cycle and the electrode surface is partially recoverable upon resting the UME in electrolyte solution without applying a potential. However complete removal of surface fouling was not possible even after sweeping the potential through highly positive values.

Comparing the CVs for Au, Figure 6-2, and CF, Figure 6-3, it is noticeable that the surface fouling occurs more quickly on CF than on Au. On CF, a steady-state current

is not observed, rather the current magnitude decreases at the most negative potentials. This behaviour can be assigned to the intrinsic properties of carbon, for example it may arise from a carbon-quinone interaction. Quinone π-electrons in a cyclic arrangement most probably interact with the carbon sp^2 domain, giving rise to relatively strong π-π interactions. This type of interaction forms the basis of stable non-covalent functionalization of a carbon substrate with aromatic units such as pyrene.[31] As for the Au case, the degree of fouling on CF decreases by reducing the solution concentration from 2 mM to 0.2 mM, but it cannot be eliminated completely, even at the lowest solution concentration. After each consecutive cycle, fouling is noticeable and the apparent steady-state diffusion limited current decreases drastically.

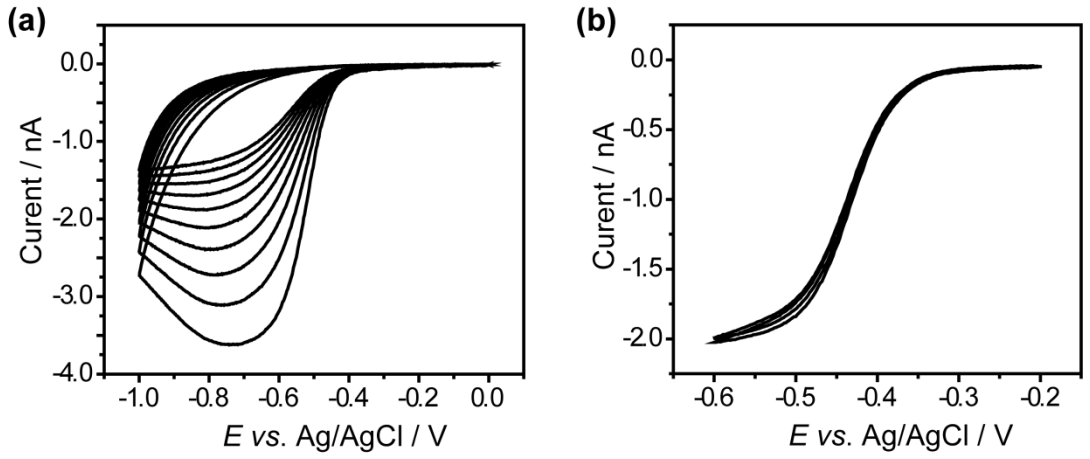

Figure 6-3. Cyclic voltammograms of 2 mM (10 cycles) (a) and 0.2 mM (2 cycles) (b) of AQ solutions in acetonitrile (0.1 M $TBAPF_6$), on a 7 μm diameter CF UME at 25 mV s^{-1}.

Another interesting aspect about electrode fouling is that fouling was not observed on a glassy carbon macro electrode (3 mm diameter, data not shown), under the same experimental conditions but in a three-electrode setup, although the mass transport

rates at macroelectrodes are much lower than for UMEs. Electrode fouling is likely to be favourable at UMEs, given the much greater fluxes of material to the electrode due to the enhanced mass transport at UMEs which exhibit hemi-spherical diffusion.

6.2.3 Steady-state voltammograms in bulk

The application of SECM for steady-state measurements of electrode kinetics is also described for both electrode materials. Table 6-3 is given to present the results of the kinetic parameters which were extracted from the CVs of five different compounds (0.2 mM) on a Au (25 μm) electrode in MeCN/TBAPF$_6$ medium at 25 mV s^{-1} scan rate. CVs are presented in Figure 6-4 performed in the bulk solution for voltammetric analysis. To determine the kinetic parameters at microdisk electrodes, the following potential differences were found

$$\Delta E = E_{3/4} - E_{1/4} \tag{6.7}$$

$$\Delta E_{1/4} = E_{1/4} - E_{1/2} \tag{6.8}$$

$$\Delta E_{3/4} = E_{1/2} - E_{3/4} \tag{6.9}$$

where $E_{1/2}$ is the half wave potential and $E_{1/4}$ and $E_{3/4}$ are voltammetric quartile potentials. Then, the values of kinetic parameters, *i.e.* the transfer coefficient (α) and formal potentials (ΔE^{0}') were calculated from Table II in ref.[32] at the intersection of $\Delta E_{3/4}$ and $\Delta E_{1/4}$ values. The errors have been estimated using the standard deviation of three consecutive CV measurements, in the same solution.

Table 6-3. Kinetic parameters extracted from steady-state voltammetric analysis of compounds studied at an Au microdisk electrode.

Compound	ΔE / mV	$\Delta E_{3/4}$ / mV	$\Delta E_{1/4}$ / mV	α	$\Delta E^{0'}$ / mV	k^0 / cm s^{-1}
***p*-BQ**	71.00	35.25	32.75	0.35 ± 0.8	9 ± 1	0.098 ± 0.017
AQ	68.35	34.00	31.75	0.36 ± 0.06	8 ± 2	0.106 ± 0.045
R	69.30	38.74	33.75	0.25 ± 0.02	8 ± 1	0.067 ± 0.001
E(+)	69.95	35.50	33.25	0.25 ± 0.05	8 ± 3	0.058 ± 0.001
E(-)	75.15	40.00	35.00	0.26 ± 0.06	12 ± 1	0.041 ± 0.003

In the case of micro-disk electrodes whose surface is not uniformly accessible, the theory describing quasi-reversible steady-state voltammograms on non-uniformly accessible electrodes was used, where k^0 is represented by Equation (6.10);[32]

$$\kappa'_{1/2} = \frac{\pi d k^0}{8 D_0} \exp[-\alpha n f \left(E_{1/2} - E^{0'}\right)] \qquad (6.10)$$

where κ' is a dimensionless rate constant that reflects electron transfer kinetics and the mass transport coefficient, and the subscript "1/2" corresponds to the half wave potential, $E_{1/2}$. Equation (6.10) assumes Butler-Volmer kinetics of the electrode reaction where

$$f = F / RT \qquad (6.11)$$

where F, R and T have their usual meaning.

6.2.4 Electrode kinetics with SECM

The application of SECM for steady-state measurements of fast heterogeneous reaction kinetics for quinones was demonstrated. For CV measurements, a Au UME, 25 μm diameter, acts as a working electrode. This tip was held in close proximity (distance, *d*) to a conductive gold substrate biased at 0.0 V, which served to regenerate the quinone from the semiquinone. This technique can be used to study very fast electrode reactions and permits calculation of more accurate rate constant values due to very high mass transport rates. This technique allows the elimination of some complications in the measurements associated with solution resistance and charging current.[33]

In aprotic solvents, the first reduction step of a quinone (Q) is known to generate the quinone radical anion ($Q^{\bullet -}$). Figure 6-4 depicts bulk and surface CVs of each compound performed at 0.2 mM concentration. Analysis was done above a 25 μm diameter gold disk electrode in acetonitrile (0.1 M $TBAPF_6$ as a supporting electrolyte), at a potential sweep rate of 25 mV s^{-1}.

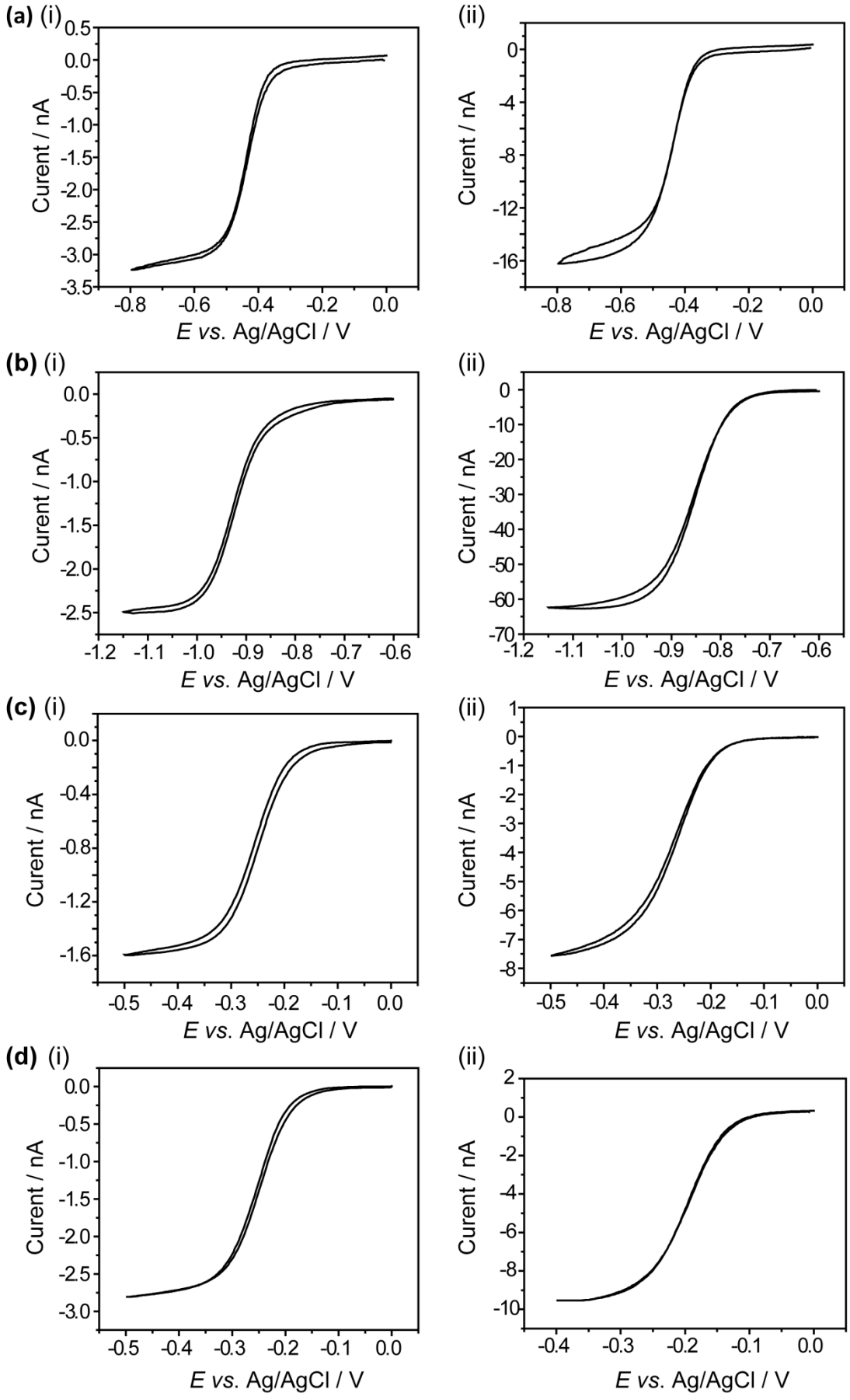
(a) (i)
Curent / nA
E vs. Ag/AgCl / V
(ii)
Curent / nA
E vs. Ag/AgCl / V
(b) (i)
Curent / nA
E vs. Ag/AgCl / V
(ii)
Curent / nA
E vs. Ag/AgCl / V
(c) (i)
Curent / nA
E vs. Ag/AgCl / V
(ii)
Curent / nA
E vs. Ag/AgCl / V
(d) (i)
Curent / nA
E vs. Ag/AgCl / V
(ii)
Curent / nA
E vs. Ag/AgCl / V

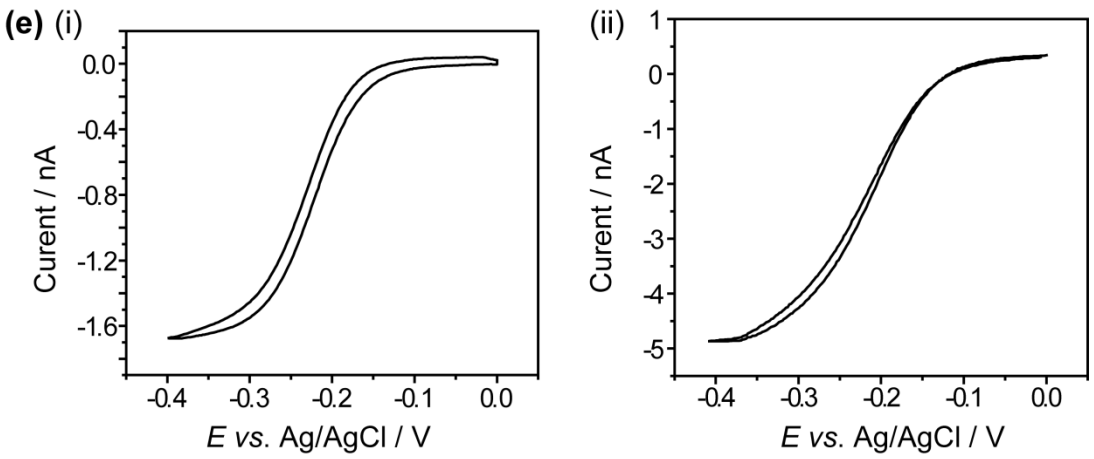

Figure 6-4. Cyclic voltammograms for the first reduction step of *p*-BQ (a), AQ (b), R (c), E+ (d) and E- (e) in bulk (i) and close to the substrate surface (ii), using 0.2 mM solutions in acetonitrile (0.1 M $TBAPF_6$), on a 25 μm diameter Au UME at a scan rate of 25 mV s^{-1}.

CVs performed on the surface of the flat Au substrate were analysed in order to calculate kinetic parameters (Figure 6-4 surface CV analysis). Substrate-tip distance was calculated from Equation (1.20). Analytical approximation for diffusion controlled steady-state current for conducting substrate can be obtained from Equation (1.20). The tip-substrate distances were calculated, and the numerical values obtained were 11.8, 0.7, 4.0, 3.4 and 3.9 μm for *p*-BQ, AQ, E(+), E(-) and R, respectively.

Kinetic parameters such as

$$\lambda = k^0 / m_O \tag{6.12}$$

α and ΔE^0 were determined from CVs at the surface, using three quartile potentials, $E_{1/2}$, $E_{1/4}$ and $E_{3/4}$. A single table containing the above parameters for all possible

pairs of $\Delta E_{1/4}$ and $\Delta E_{3/4}$ is available (see Table I in Ref.[32]) for all parameters. Each parameter was determined from this Table and represented in Table 6-4.

After determination of such parameters, the effective mass transfer coefficient for SECM (m_O) was calculated from following equation;[32,34]

$$m_O = 4D_O\left(\frac{0.68 + 0.78377/L + 0.3315\exp\left(-1.0672/L\right)}{\pi a}\right) = \frac{I_T(L)}{\pi a^2 nFC_O^*} \quad (6.13)$$

Consequently, the standard rate constant, k^0 was determined from Equation (6.12) (Table 6-4).[32]

Table 6-4. Kinetic parameters extracted from SECM steady-state voltammetric analysis of compounds studied at an Au microdisk electrode.

Compound	ΔE / mV	$\Delta E_{3/4}$ / mV	$\Delta E_{1/4}$ / mV	α	$\Delta E^{0'}$ / mV	k^0 / cm s^{-1}
***p*-BQ**	85.00	47.50	35.00	0.27 ± 0.03	20 ± 6	0.23 ± 0.02
AQ	76.10	39.50	33.00	0.41 ± 0.02	11 ± 5	1.26 ± 0.46
R	83.00	51.55	35.00	0.27 ± 0.06	11 ± 6	0.19 ± 0.05
E(+)	70.50	38.50	32.05	0.34 ± 0.05	8 ± 7	0.28 ± 0.06
E(-)	90.00	55.00	37.50	0.23 ± 0.06	17 ± 9	0.12 ± 0.06

The bulk UME measurements (Table 6-3) are close to reversible, where ΔE = 59 mV for a truly reversible case. The SECM feedback measurements (Table 6-4) have slightly larger ΔE, however even these might be reversible. As such, it should be stressed that the values for k^0 are, in effect, lower limits only.

Table 6-4 shows k^0 values obtained by the SECM technique were approximately 2-4 times higher than the values determined by CVs obtained in bulk solution, since the SECM technique enable much higher rates of mass transfer of active species, since the UME tip is held close to the substrate surface which is able to regenerate the quinone species. Despite careful IR compensations by using the UME, the values obtained in bulk solution cannot always guarantee the accuracy of the analysis especially when the ET kinetics are too fast. The value of the rate constant for AQ (k^0 = 1.26 ± 0.46 cm s^{-1}), as determined using the positive feedback method, is roughly 12 times higher than the value calculated using the bulk CV analysis (k^0 = 0.106 ± 0.045 cm s^{-1}). The high ET kinetics were determined due to the small distance between the tip and the substrate surface (0.7 μm). As discussed before, mass transport increases dramatically at very close substrate-tip separations. Therefore, the mass transfer coefficient (m_O) for AQ is much higher compared to the values obtained for the other compounds, which were within the range of 0.046 – 0.065. The main difficulty with obtaining a very small tip-substrate separation is most probably the surface blocking processes that prevents an effective approach of the UME tip to the substrate surface. This phenomenon was extensively explained at both Au and CF electrodes above.

6.2.5 Non-steady-state voltammetry

Electrode fouling turned out to be a substantial concern for our measurements performed at low scan rate bulk voltammetric analysis and also for the experiments performed with the SECM technique. This surface blocking issue was successfully eliminated for Au electrode by simple modifications in experimental conditions, *i.e.*

lower concentration. However it remained a significant drawback in measurements performed using the CF electrode. Therefore, the potential scan rate was increased to eliminate the error arising from carbon surface blocking processes impeding accurate evaluation of kinetic parameters.

Performing the CVs at higher scan rates, 1 V s^{-1} was chosen as the slowest scan rate that did not show effects of fouling. At 1 V s^{-1}, the CV current response will be formed under mixed planar and radial diffusion. The consequence is that analysing them with a linear diffusion model will produce inaccurate rate constants. It should be noted that the data are of high quality and are highly reproducible. Steady-state rate constants are more reliable, with the caveat that there may be subtle blocking effects. Typical CVs at 1 V s^{-1} on Au and CF are shown in Figure 6-5.

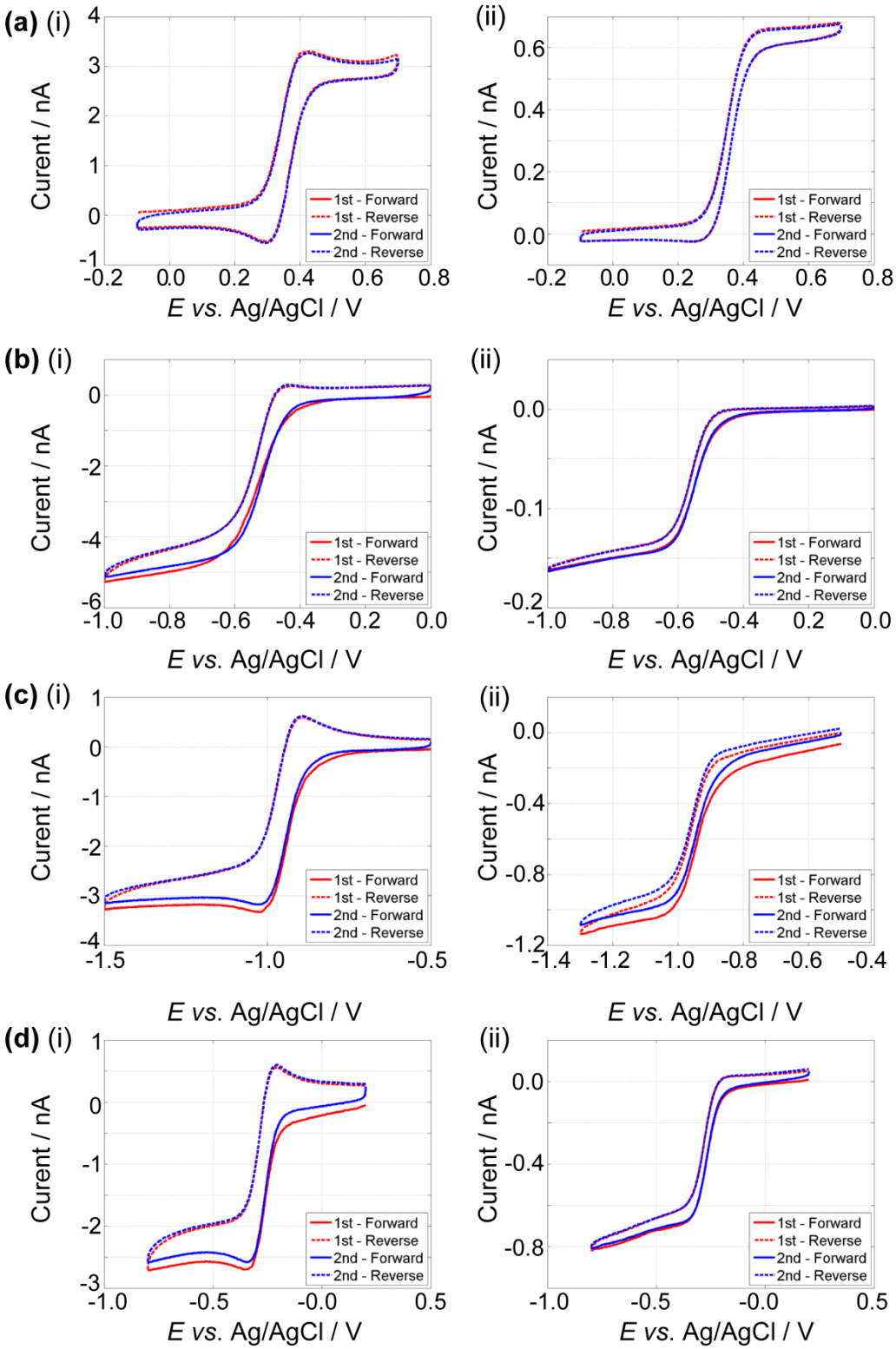

Figure 6-5. Cyclic voltammograms for the oxidation of ferrocene (a) and the first reduction steps of *p*-BQ (b), AQ (c) and R (d) on a 25 μm diameter Au UME (i) and a 7 μm diameter CF UME (ii) at a scan rate of 1 V s^{-1} and concentration of 0.2 mM in acetonitrile (0.1 M $TBAPF_6$).

Non-steady-state voltammetry was performed to increase the accuracy of kinetic parameters on the CF UME at relatively faster scan rates. As previously discussed, quinone adsorption is stronger on carbon-type electrodes, which blocks the surface of the electrode and prevents the accurate measurements of kinetics. Thus, increasing the scan rate above the values which were used for the measurements at the Au electrode is advantageous in preventing strong electrode fouling.

Standard rate constants of quinone compounds are not given for the CF electrode, due to the relatively strong adsorption behaviour on the CF electrode. Even though the degree of adsorption can be decreased by changing some experimental conditions, the surface blocking phenomenon could not be completely removed. It has been previously demonstrated that the use of the Nicholson method[22] to analyse CVs obtained at a microdisk electrode at intermediate scan rates without accounting for non-linear diffusion leads to an underestimation of k^0. A more sophisticated analysis is necessary to reduce this difference.[35] The analysis of these data requires customised simulations, which will be carried out in the future.

Adsorbed species can form a dense liquid layer (or an adsorbed layer) adjacent to the surface of the electrode. In considering that ET occurs from the electrode to the redox active species, or visa-versa, through electron tunneling, adsorbed layers are more likely to reduce the interaction (by increasing the tunnelling distance) between the electrode and redox active species and so, decrease the ET rate. The compounds studied have different molecular structures and substituents which may lead to a different degree of fouling due to the interaction of compounds with either the carbon skeleton, or different functionality on the surface of the CF electrode.

6.3 General discussion on adiabaticity of quinone reactions

Theories of ET kinetics based on macroscopic concepts simply involve parameters like α and k^0. On the other hand, such theories can no longer be effective once the structural modifications and environmental factors start to influence the rate of electrochemical processes. Therefore, Marcus-Hush theory[36] can be considered as an appropriate microscopic approach since it involves a reorganisation energy term which covers the influence of solvent dynamics and structural changes of both reactants and products on the electron transfer mechanism. Equation (6.14) is based on a transition-state formalism of heterogeneous electron-transfer kinetics that Marcus-Hush theory explains.

The heterogeneous ET rate constants can be calculated according to Marcus theory:

$$k^0 = K_p \nu_n \ \kappa \exp\left(-\Delta G^* / RT\right) \tag{6.14}$$

where, K_p is the equilibrium constant, ν_n is the nuclear barrier crossing frequency, κ is the electronic transmission coefficient, and ΔG^* is the Gibbs energy of activation for the electrode reaction, R is the universal gas constant and T is temperature.[11]

Marcus-Hush theory emerged as a significant contribution to the ET theory since it focuses on the effect of chemical properties of both reduced and oxidised species on ET kinetics. This approach has been widely applied to electrochemical reactions in order to predict the influence of structural effects on kinetic properties.[37]

In ET theory, adiabaticity generally refers to the extent of interaction or electronic coupling between a reactant and the electrode. If this interaction is strong, which occurs when a sufficiently close distance was achieved, κ approaches unity and the

process is called adiabatic. If this reaction is weak, the process is said to be non-adiabatic and κ becomes smaller than unity.

A recent study by Compton *et al*.[17] demonstrates a valuable discussion by comparing the reaction kinetics of a family of quinones on CF and Au UMEs. ET on carbon electrodes was considered as non-adiabatic and the rate of electron transfer was said to be associated with the variation in redox potential since the density of states (DOS) was expected to vary with potential. On the other hand, electrochemical reactions on Au were assumed to be adiabatic and the DOS for Au was considered as constant, which is indeed the case for adiabatic processes.

In non-adiabatic systems the rate depends strongly on the strength of the interaction. In Compton's work, coupling strength (V) was considered as constant, so the rate and the DOS of the electrode were said to be directly proportional. Table 6-1 includes a comparison of kinetic parameters extracted from their work. Based on the results presented, faster ET kinetics for quinones were confirmed for the CF substrate. Therefore, electronic coupling of quinone species to the electrode surface was reported to be greater for carbon than gold electrodes.[17]

Schmickler's short discussion[38] on adiabaticity of quinone ET on graphite electrodes is highly relevant to the study and important. Most of the outer sphere ET kinetics on metals are assumed to be adiabatic, yet there is a little doubt about the likelihood of an adiabatic process on semimetals like graphite. Therefore, their work mainly argues about whether quinone electroreduction on graphite is adiabatic by re-examining the experimental data presented by Compton *et al*.[17]

Their density functional theory (DFT) calculations reveal that non-adiabatic reactions should be slower on graphite since the DOS of graphite is smaller than

gold which is contrary to what Compton reported.[17] Their reasoning for the gold case, which is truly adiabatic, is enlightening as to why the overall rate constant is independent of electronic properties of the electrode material. In the adiabatic case, the energy of reorganisation is much greater than the interaction constant, therefore the overall rate depends solely on solvent dynamics. They reported all these reactions to be fast and adiabatic.

As detailed in an early study by Kojima and Bard,[39] electrochemical kinetics of most aromatic compounds were assumed to be adiabatic, in which variation of the rate constant was directly related to changes in the reorganisation energy. Once more, it has been confirmed that all reactions are fast and adiabatic on a Au electrode. In our particular case, reorganisation energy and so the rate constant is governed by solvent dynamics (outer component) since neither reactants nor products change their configuration during actual ET.

According to voltammetric analysis at the CF UME, relatively slower kinetics were observed for most of the compounds studied. However, it is relevant to point out that quinone electroreduction at carbon electrodes should be as fast as that at on Au electrodes. As previously discussed, these reactions are supposed to be adiabatic on semimetals, like graphite.[38] Thus, the question is: is the observed rate constant slower than the true values due to electrode fouling for carbon electrodes?

If quinone species undergo strong interactions with the carbon skeleton, solution species can form a dense liquid layer (or an adsorbed layer) adjacent to the surface of the electrode. In considering that ET occurs from the electrode to the redox active species, or visa-versa, through electron tunneling, adsorbed layers are more likely to reduce the interaction between the electrode and redox active species. The electronic

transmission coefficient (κ) which participates in the rate Equation (6.4) is directly related to this interaction and if this interaction weakens by an adsorption barrier, the rate constant rapidly falls off. As discussed before, if κ declines beyond unity, the reaction is no longer adiabatic.

On the basis of our findings, there seems to be no other logical reason to make quinone reactions slow down on carbon-based electrodes. Even if graphite electronic structure does have influence on rate constants, which is not the case here, quinone kinetics should be fast enough on this material since a recent study demonstrates absolute evidence that ET on the basal planes of graphite can be rather fast.[40]

6.4 Conclusions

Aprotic media permit the study of single-step electron transfer (ET) kinetics of quinones due to the stabilisation of the radicalic intermediates. As such, experiments were performed for a family of quinones at Au and CF UMEs, in acetonitrile. Electrode surface fouling was observed for almost all compounds. Different degrees of surface fouling were observed depending both on the electrode material, the compound studied and its concentration. The issue of fouling was minimised on Au by simple modification of reaction conditions, *i.e.* lowering quinone concentration and increasing the potential scan rate (under steady-state conditions). Surface blocking processes could not be eliminated for CF, however, due to the strong quinone-carbon interaction.

Voltammetric analysis for the reduction of the quinones to semiquinone was used for the Au electrode. Rate constants calculated via steady-state CVs correlate with some in the literature but are very close to the reversible limit. The observed standard rate constant for anthraquinone reduction was found higher than other type of quinones investigated, which is reasonable given the more delocalised charge on this conjugated system. SECM was further employed for the Au UME on flat gold substrate. Higher rate constants were reported by implementation of SECM technique comparing to steady-state analysis due to higher mass transport rates. Even in this configuration, with higher mass transport, the response is close to reversible.

Non-steady-state CV analysis was performed for kinetic studies of compounds at a CF UME. However, numerical evaluation of rate constant requires a dedicated model.

6.5 References

(1) Morton, R. A. *Biochemistry of Quinones*; 1st ed.; Academic Press: London, 1965.

(2) Hay, S.; Westerlund, K.; Tommos, C. *J. Phys. Chem. B* **2007**, *111*, 3488.

(3) Wei Yao, W.; Mei Peng, H.; Webster, R. D. *J. Phys. Chem. C* **2009**, *113*, 21805.

(4) Lehmann, M. W.; Evans, D. H. *J. Phys. Chem. B* **2001**, *105*, 8877.

(5) Namazian, M.; Coote, M. L. *J. Phys. Chem. A.* **2007**, *111*, 7227.

(6) Choi, W.; Harada, D.; Oyaizu, K.; Nishide, H. *J. Am. Chem. Soc.* **2011**, *133*, 19839.

(7) Roldán, S.; Blanco, C.; Granda, M.; Menéndez, R.; Santamaría, R. *Angew. Chem., Int. Ed.* **2011**, *50*, 1699.

(8) Sato, Y.; Fujita, M.; Mizutani, F.; Uosaki, K. *J. Electroanal. Chem.* **1996**, *409*, 145.

(9) Kim, Y.-O.; Jung, Y. M.; Kim, S. B.; Park, S.-M. *Anal. Chem.* **2004**, *76*, 5236.

(10) Guin, P. S.; Das, S.; Mandal, P. C. *Int. J. Electrochem.* **2011**, *2011*.

(11) Hubig, S. M.; Kochi, J. K. *J. Am. Chem. Soc.* **1999**, *121*, 1688.

(12) Simonov, A. N.; Morris, G. P.; Mashkina, E. A.; Bethwaite, B.; Gillow, K.; Baker, R. E.; Gavaghan, D. J.; Bond, A. M. *Anal. Chem.* **2014**, *86*, 8408.

(13) Evans, D. H. *Chem. Rev.* **2008**, *108*, 2113.

(14) Penner, R. M.; Heben, M. J.; Longin, T. L.; Lewis, N. S. *Science* **1990**, *250*, 1118.

(15) Rees, N. V.; Clegg, A. D.; Klymenko, O. V.; Coles, B. A.; Compton, R. G. *J. Phys. Chem. B* **2004**, *108*, 13047.

(16) Wang, Y.; Rogers, E. I.; Belding, S. R.; Compton, R. G. *J. Electroanal. Chem.* **2010**, *648*, 134.

(17) Nissim, R.; Batchelor-McAuley, C.; Henstridge, M. C.; Compton, R. G. *Chem. Commun.* **2012**, *48*, 3294.

(18) Samuelsson, R.; Sharp, M. *Electrochim. Acta* **1978**, *23*, 315.

(19) Rüssel, C.; Jaenicke, W. *J. Electroanal. Chem.* **1986**, *200*, 249.

(20) Capon, A.; Parsons, R. *J. Electroanal. Chem.* **1973**, *46*, 215.

(21) Rosanske, T. W.; Evans, D. H. *J. Electroanal. Chem.* **1976**, *72*, 277.

(22) Nicholson, R. S. *Anal. Chem.* **1965**, *37*, 1351.

(23) Uslu, B.; Ozkan, S. A. *Comb. Chem. High Throughput Screening* **2007**, *10*, 495.

(24) Bard, A. J.; Fan, F. R. F.; Kwak, J.; Lev, O. *Anal. Chem.* **1989**, *61*, 132.

(25) Lai, S. C. S.; Macpherson, J. V.; Unwin, P. R. *MRS Bulletin* **2012**, *37*, 668.

(26) McKelvey, K.; Edwards, M. A.; Unwin, P. R. *Anal. Chem.* **2010**, *82*, 6334.

(27) McGeouch, C.-A.; Peruffo, M.; Edwards, M. A.; Bindley, L. A.; Lazenby, R. A.; Mbogoro, M. M.; McKelvey, K.; Unwin, P. R. *J. Phys. Chem. C* **2012**, *116*, 14892.

(28) Mirkin, M. V.; Horrocks, B. R. *Anal. Chim. Acta* **2000**, *406*, 119.

(29) Wang, Y.; Rogers, E. I.; Compton, R. G. *J. Electroanal. Chem.* **2010**, *648*, 15.

(30) Batchelor-McAuley, C.; Goncalves, L. M.; Xiong, L.; Barros, A. A.; Compton, R. G. *Chem. Commun.* **2010**, *46*, 9037.

(31) Ehli, C.; Rahman, G. M. A.; Jux, N.; Balbinot, D.; Guldi, D. M.; Paolucci, F.; Marcaccio, M.; Paolucci, D.; Melle-Franco, M.; Zerbetto, F.; Campidelli, S.; Prato, M. *J. Am. Chem. Soc.* **2006**, *128*, 11222.

(32) Mirkin, M. V.; Bard, A. J. *Anal. Chem.* **1992**, *64*, 2293.

(33) Mirkin, M. V.; Richards, T. C.; Bard, A. J. *J. Phys. Chem.* **1993**, *97*, 7672.

(34) Mirkin, M. V.; Fan, F.-R. F.; Bard, A. J. *J. Electroanal. Chem.* **1992**, *328*, 47.

(35) Lavagnini, I.; Pastore, P.; Magno, F. *J. Electroanal. Chem.* **1992**, *333*, 1.

(36) Laborda, E.; Henstridge, M. C.; Batchelor-McAuley, C.; Compton, R. G. *Chem. Soc. Rev.* **2013**, *42*, 4894.

(37) Bard, A. J.; Faulkner, L. R. *Electrochemical Methods: Fundamentals and Applications*; 2nd ed.; John Wiley & Sons, Inc.: New York, 2001.

(38) Luque, N. B.; Schmickler, W. *Electrochim. Acta* **2013**, *88*, 892.

(39) Kojima, H.; Bard, A. J. *J. Am. Chem. Soc.* **1975**, *97*, 6317.

(40) Lai, S. C. S.; Patel, A. N.; McKelvey, K.; Unwin, P. R. *Angew. Chem., Int. Ed.* **2012**, *51*, 5405.

7 Conclusions

Although SECM is a well-established technique, the technique has largely (traditionally) been limited to studies using UMEs. There also remains scope for better tip-substrate distance determination methods, of key importance for electrochemical imaging using nanoelectrodes, and for alternative scanning modes.

HIC-SECM, as described in Chapter 3, advances SECM in both these respects. The nature of the 'hopping' mode also allows bulk measurements to be made at various points in the scan, in order to 'self-reference' measurements at the tip. This new technique will be powerful to visualise the chemical flux around many types of interface quantitatively, since the tip-substrate distance can be reliably determined and controlled.

Operating SECM with nanoelectrodes is particularly challenging, and whilst it is recognised that other attempts have been made, using nanoelectrodes with IC-SECM is a significant advancement to the field of SECM. By using a lower force configuration to that used previously for IC-SECM with UMEs, the results in Chapter 4 showed how IC-SECM could be implemented with nanoelectrode tips for electrochemical imaging over a model substrate.

The use of HIC-SECM over model substrates was demonstrated in Chapter 4, and useful information was carefully extracted from the data set obtained in the scan. For example, an extensive data set was simultaneously collected that included: tip current; substrate current; the AC component of these two direct currents, that was induced by the oscillating probe, and the phase difference of this AC signal; and the oscillation amplitude of the probe used to sense the surface.

These data were presented in a range of ways, including a full 3D tip current plot, which demonstrates the volume of data that is collected in a HIC-SECM scan. This 3D tip scanning mode allows 'slices' of data in a plane parallel to the surface, at various heights from the surface, or 'slices' perpendicular to the surface to be plotted. The latter is particularly powerful for visualising local concentration of species around a substrate, and can be used to determine flux of reactants to an electrode.

Whilst it is recognised that other similar hopping techniques, including 4D shearforce SECM, can provide similar information of concentrations of species around a substrate, HIC-SECM is a significant advancement to the field of SECM, since additional data are acquired during the scan, and there are fewer restrictions on the type of probe that may be used. Although the results presented in Chapters 3 and 4 are for amperometric tips over model substrates, in principle, any probe for SECM should be useable, including potentiostatic probes.

The work in Chapter 5 reveals considerable new insights on the formation of NPs on surfaces, and provides a novel method for the synthesis of NPs. Understanding the formation and interaction of NPs with supports is a key topic in chemical nanoscience, with applications spanning energy conversion systems (fuel cells and batteries) to sensors (electrochemical, electrical and optical). Yet, these processes have proved difficult to address with existing techniques. Using the high time and spatial resolution of the SECCM technique, and complementary microscopy, the formation of silver NPs on HOPG has been monitored, showing unequivocally that a nucleation-aggregative growth-detachment mechanism operates that has not been reported before. This mechanism is important not only for obtaining a better understanding of metal electrodeposition, but also for elucidating the active sites for

electron transfer on HOPG, a topic of recent debate. The microscopic observations are shown to scale up and rationalised to provide an holistic view.

While the results here are focused on silver deposition on HOPG, the methodology is general and could be applied to almost any metal electrodeposition. Furthermore, carbon-supported NPs are ubiquitous in a wide variety of fields such as (general) electrochemistry, (electro)catalysis, biosensing, surface science and material research.

The work in Chapter 6 highlights the difficulty in measuring fast heterogeneous electron transfer kinetics at UMEs. UMEs exhibit high rates of flux as compared to macroelectrodes, which can exacerbate electrode surface fouling processes. Simple measures can be taken to avoid this problem with quinone compounds in organic media, such as lowering the analyte concentration and increasing the potential scan rate. Increasing the potential scan rate results in non-steady-state CVs, for which a dedicated model is required for numerical evaluation of rate constants. Rate constants for a Au electrode were calculated (although lower limits), since fouling was not as problematic on Au as compared to CF electrodes. This was done using the IC-SECM technique in order to minimise possible blocking effects and achieve higher rates of mass transport as compared to performing measurements in bulk solution.